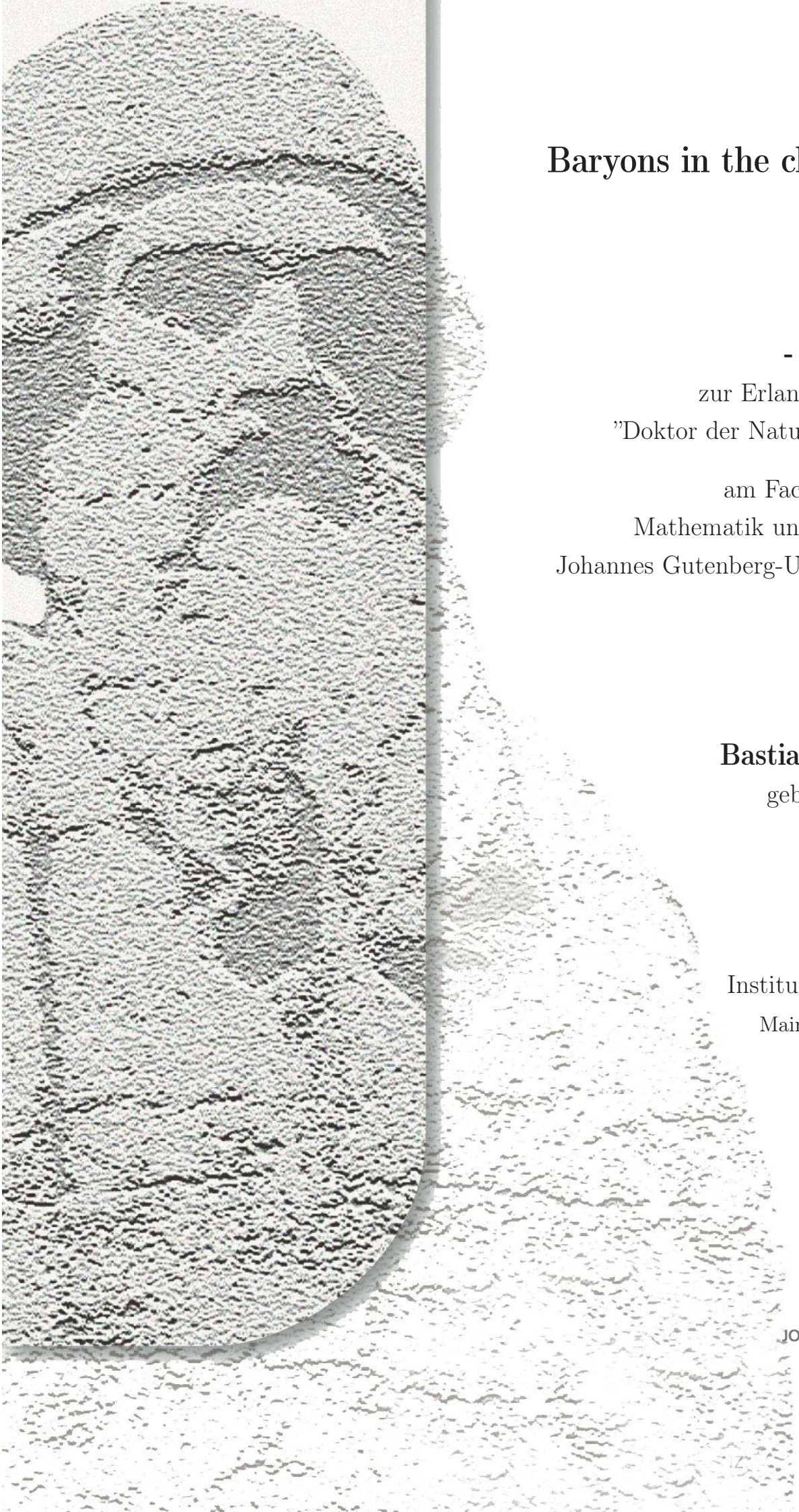

Baryons in the chiral regime

- Dissertation -

zur Erlangung des Grades
"Doktor der Naturwissenschaften"

am Fachbereich Physik,
Mathematik und Informatik der
Johannes Gutenberg-Universität Mainz

Bastian Knippschild
geboren in Korbach

Institut für Kernphysik

Mainz, 6. Oktober 2011

JOHANNES GUTENBERG UNIVERSITÄT MAINZ

Tag der Promotion: 28.02.2012

Contents

Zusammenfassung

Als Quantenchromodynamic (QCD) bezeichnet man die Theorie der starken Wechselwirkung, eine der vier fundamentalen Kräfte unseres Universums. Sie beschreibt die Wechselwirkung zwischen Quarks und Gluonen, welche die grundlegenden Bausteine der Hadronen wie Neutronen und Protonen sind. Fast die gesamte sichtbare Materie unseres Universums ist aus Protonen und Neutronen aufgebaut. Daher ist die Forschung sehr an ihren Eigenschaften (z.B. der Masse, der Ladungsverteilung und ihrer Form) interessiert.
Der einzige theoretische Zugang zu diesen Eigenschaften, der nicht-perturbativ und *ab initio* ist, ist die Gitter QCD. Allerdings erreichen heutige Gittersimulationen leider noch nicht die Genauigkeit von Experimenten, vor allem für baryonische Größen. Es ist sogar so, dass einige der Werte, die durch Gittersimulationen erzeugt werden, innerhalb ihrer Fehler nicht mit den experimentellen Werten übereinstimmen. Die Frage ist nun, ob diese Abweichungen durch systematische Effekte der Gitter QCD erklärt werden könnten.

Die vorliegende Arbeit beschäftigt sich daher mit der Berechnung von Formfaktoren des Nukleons und anderen hadronischen Größen in der Gitter QCD. Um diese zu berechnen, wurden sogenannte Wilson-Fermionen genutzt, wobei die entsprechenden u- und d-Quarks voll dynamisch behandelt wurden. Die Simulationen wurden auf verschiedenen Eichensembles mit Variationen von Pionmassen, Gitterabständen und Volumen durchgeführt.
Als erstes galt es, den Gitterabstand zu bestimmen, um einen Kontakt zwischen den Ergebnissen der Gitter QCD und den Experimenten herzustellen und einen Kontinuumslimes zu ermöglichen. Die leichte Quarkmasse wurde bei dem folgenden Wert bestimmt: $m_{ud}^{\overline{\text{MS}}}(2\text{ GeV}) = 3.03(17)(38)$ MeV.

Dieses Ergebnis zeigt eine gute Übereinstimmung mit den experimentellen Werten und anderen Gitter-Bestimmungen.
Als nächstes wurden die elektromagnetischen und axialen Formfaktoren des Nukleons berechnet, anschließend von diesen die Radien und Ladungen abgeleitet. Die verschiedenen Eichensembles ermöglichten nun, die Abhängigkeit dieser Größen bezüglich des Volumens, des Gitterabstands und der Pionmasse zu untersuchen. Am Ende wurde eine Kontinuums- und chirale Extrapolation zum physikalischen Punkt durchgeführt.
Zusätzlich wurden angeregte Zustände, die zu diesen Größen beitragen, untersucht. Wir nutzten hierzu die sogenannte Summationsmethode, welche die Beiträge von angeregten Zuständen stark reduziert, was eine deutlich bessere Übereinstimmung mit den experimentellen Werten liefert. Im Gegensatz dazu weichen die Werte für z.B. die axiale Ladung und den Dirac-Radius, die durch frühere Gittersimulationen bestimmt wurden, deutlich von den experimentellen Werten ab. Durch die sorgfältige Untersuchung der systematischen Effekte konnten folgende Werte erzielt werden $\langle r_1^2 \rangle_{u-d} = 0.627(54)$ fm^2 und $g_A = 1.218(92)$, welche eine gute Übereinstimmung innerhalb der Fehler mit den experimentellen Werten aufweisen.

Die ersten drei Kapitel der Dissertation führen in die theoretischen Grundlagen der Formfaktoren und der Gitter QCD ein. In Kapitel vier wird der Gitterabstand bestimmt, die Berechnung der Formfaktoren wird in Kapitel fünf erläutert, wobei die Auswirkungen von systematischen Effekten untersucht werden. In Kapitel sechs werden alle Ergebnisse präsentiert. Die Arbeit endet mit einer Zusammenfassung der Resultate und zeigt Möglichkeiten auf, um die hier vorgestellten Berechnungen zu ergänzen und weiterzuführen.

Abstract

Quantum Chromodynamics (QCD) is the theory of strong interactions, one of the four fundamental forces in our Universe. It describes the interaction of gluons and quarks which build up hadrons like protons and neutrons. Most of the visible matter in our universe is made of protons and neutrons. Hence, we are interested in their fundamental properties like their masses, their distribution of charge and their shape.
The only known theoretical, non-perturbative and *ab initio* method to investigate hadron properties at low energies is lattice Quantum Chromodynamics (lattice QCD). However, up-to-date simulations (especially for baryonic quantities) do not achieve the accuracy of experiments. In fact, current simulations do not even reproduce the experimental values for the form factors. The question arises wether these deviations can be explained by systematic effects in lattice QCD simulations.

This thesis is about the computation of nucleon form factors and other hadronic quantities from lattice QCD. So called Wilson fermions are used and the u- and d-quarks are treated fully dynamically. The simulations were performed using gauge ensembles with a range of lattice spacings, volumes and pion masses.
First of all, the lattice spacing was set to be able to make contact between the lattice results and their experimental complement and to be able to perform a continuum extrapolation. The light quark mass has been computed and found to be $m_{ud}^{\overline{\text{MS}}}(2\,\text{GeV}) = 3.03(17)(38)$ MeV. This value is in good agreement with values from experiments and other lattice determinations.
Electro-magnetic and axial form factors of the nucleon have been calculated. From these form factors the nucleon radii and the coupling constants were computed. The different ensembles enabled us to investigate systematically the dependence of these quantities on the volume, the lattice spacing and the pion mass.

Finally we perform a continuum extrapolation and chiral extrapolations to the physical point.
In addition, we investigated so called excited state contributions to these observables. A technique was used, the summation method, which reduces these effects significantly and a much better agreement with experimental data was achieved. On the lattice, the Dirac radius and the axial charge are usually found to be much smaller than the experimental values. However, due to the carefully investigation of all the afore-mentioned systematic effects we get $\langle r_1^2 \rangle_{u-d} = 0.627(54)$ fm^2 and $g_A = 1.218(92)$, which is in agreement with the experimental values within the errors.

The first three chapters introduce the theoretical background of form factors of the nucleon and lattice QCD in general. In chapter four the lattice spacing is determined. The computation of nucleon form factors is described in chapter five where systematic effects are investigated. All results are presented in chapter six. The thesis ends with a summary of the results and identifies options to complement and extend the calculations presented.

Chapter 1

Introduction

Quantum chromodynamics (QCD) is the theory of strong interactions, one of the four fundamental forces in our Universe. It describes the interaction of gluons and quarks which build up hadrons like protons and neutrons. Most of the visible matter in our universe is build of protons and neutrons. Hence, we are interested in their fundamental properties like their masses, their distribution of charge and their shape. Most of these quantities are directly related to form factors $F(q^2)$ of the hadrons which only depend on the squared momentum transfer q^2. Some of these quantities are the electric charge Q, the axial charge g_A, the anomalous magnetic moment μ and the mean squared radii. It should be possible to study these parameters with QCD.
Perturbation theory of QCD is only applicable at high energies because of its non-Abelian character [109] which is related to the $SU(3)$ color gauge group. At small energies quarks are confined and hence strongly bound but they become asymptotically free at high energies [88, 51, 50]. The aforementioned quantities like radii and charges are defined at zero momentum transfer where the quarks are not free. Hence, perturbation theory does not work and other methods have to be used. The only known non-perturbative way to describe the strong interactions from first principles is lattice QCD. The basic idea is to discretize the space-time on a four dimensional lattice. Observables like masses or matrix elements can be computed with simulations on high performance computing systems.
Masses of hadrons are one of the easiest quantities which can be computed in lattice QCD. In 2010 a remarkable study was published [38] where masses of several of light hadrons were computed within high precision. Three different lattice spacings and large volumes

have been used to minimize cut-off and volume effects. The smallest pion masses were around 190 MeV which is very close to the physical point. No deviations have been observed from lattice to experimental data.
Other quantities like the radii of the nucleon or the axial coupling constant are by far not in such a good agreement with experimental data. They can be computed in lattice QCD from matrix elements.
The matrix element of a nucleon with initial momentum p and spin s and final momentum p' and spin s' interacting with an electro-magnetic current $V_\mu = \overline{\Psi}(x)\gamma_\mu\Psi(x)$ can be expressed as [59]

$$\left\langle N(p',s')\left|V_\mu\right|N(p,s)\right\rangle = \bar{u}(p',s')\left\{\gamma_\mu F_1(Q^2) + i\frac{\sigma_{\mu\nu}q_\nu}{2m_N}F_2(Q^2)\right\}u(p,s). \tag{1.1}$$

The functions $F_1(Q^2)$ and $F_2(Q^2)$ are the Dirac- and Pauli form factors of the nucleon which only depend on the momentum transfer Q^2. On the right-hand side of eq. 1.1 $\bar{u}(p',s')$ and $u(p,s)$ are Dirac spinors, γ_μ is a Dirac matrix and $\sigma_{\mu\nu} = \frac{1}{2i}\{\gamma_\mu,\gamma_\nu\} = \frac{1}{2i}(\gamma_\mu\gamma_\nu - \gamma_\nu\gamma_\mu)$. The indices μ and ν always denotes the four Dirac components $\mu,\nu = 0,1,2,3$.
These form factors are usually measured in scattering experiments. Electrons or muons, which have no inner structure up to 10^{-18}m, are scattered on a nucleon. One of the most precise measurements of the proton form factor was done in Mainz at MAMI [14]. The differential cross section of an electron or muon with a nucleon is described by the Rosenbluth formula [91]

$$\left(\frac{\mathrm{d}\,\sigma}{\mathrm{d}\,\Omega}\right) \sim \left[\frac{G_E^2(Q^2) + \tau G_M^2(Q^2)}{1+\tau} + 2\tau G_M^2(Q^2)\tan^2\frac{\Theta}{2}\right], \text{ with } \tau = \frac{Q^2}{4m_N}. \tag{1.2}$$

This formula contains the two Sachs form factors $G_E(Q^2)$ and $G_M(Q^2)$. The angle Θ is the angle of deviation of the electron or muon from its original path and m_N is the nucleon mass. The connection of the Dirac and Pauli form factors to the Sachs form factors is given by

$$G_E(Q^2) = F_1(q^2) - \frac{Q^2}{4m_N}F_2(Q^2), \qquad G_M(Q^2) = F_1(Q^2) + F_2(Q^2). \tag{1.3}$$

The matrix element of a nucleon with the axial current $A_\mu = \overline{\Psi}(x)\gamma_\mu\gamma_5\Psi(x)$ is given by

$$\left\langle N(p',s') \left| A_\mu \right| N(p,s) \right\rangle = \bar{u}(p',s') \left\{ \gamma_\mu\gamma_5 G_A(Q^2) + \gamma_5 \frac{q_\mu}{2m_N} G_P(Q^2) \right\} u(p,s)$$

where $G_A(Q^2)$ is the axial form factor and $G_P(Q^2)$ the induced pseudo-scalar form factor. The axial form factors can be measured from different kinds of processes like charged pion electro-production off nucleons or Neutrino-nucleon scattering [11].
The form factors can be Taylor expanded in the momentum transfer as

$$G(Q^2) = g\left(1 + \frac{1}{6}\left\langle r^2 \right\rangle Q^2 + \mathcal{O}(Q^4)\right) \tag{1.4}$$

where $g = G(0)$ is the the form factor at zero momentum transfer and r is the corresponding radius. For the electro-magnetic and axial form factors it follows that:

$$G_E(0) = 1 \qquad \text{(electric charge)}, \tag{1.5}$$

$$G_M(0) = \mu \qquad \text{(magnetic moment)}, \tag{1.6}$$

$$G_A(0) = g_A \qquad \text{(axial charge)}. \tag{1.7}$$

The exception to this definition is the induced pseudo-scalar coupling constant g_P. It is defined as

$$g_P = \frac{m_\mu}{m_N} G_P(Q^2 = 0.88 m_\mu^2), \tag{1.8}$$

where m_μ is the muon mass. Most experimental measurements of the induced pseudo-scalar form factor suffer from muon capture. Thus it is defined at the four-momentum transfer for muon capture where the proton is at rest. This is at $Q^2 = 0.88 m_\mu^2$.
The radii can be computed via derivatives with respect to the momentum transfer at zero momentum transfer. This leads to

$$\left\langle r_X^2 \right\rangle = \frac{6}{G_X(0)} \left. \frac{\partial G_X(Q^2)}{\partial Q^2} \right|_{Q=0}, \qquad \text{where } X = E, M, A, P. \tag{1.9}$$

The explicit computation of nucleon matrix elements in lattice QCD is discussed in chapter 3 in detail.

In 2010, a publication appeared where the proton radius was measured in muonic hydrogen atoms with laser spectroscopy [87]. It turned out that their determination differs by five standard deviations from the experimental value quoted by CODATA (http://www.codata.org/) and from the values measured with electron scattering experiments at the Mainzer Microtron [14]. Lattice QCD cannot resolve this issue at the moment because the required statistical precision cannot be achieved with up-tp-date computer systems and algorithms. In addition, lattice QCD suffers from systematic effects which lead to discrepancies between lattice results and experimental values. However, if we want to be in the position to resolve the discrepancies in the experiments some day we have to understand all systematic errors in lattice QCD. The statistical precision may become better automatically in the next years with larger accessible computer power.

Constantia Alexandrou presented a summary of all lattice results of the electro-magnetic form factors and the axial charge at the lattice conference in 2010 [2]. Figure 1.1 shows the electric $G_E^p(Q^2) - G_E^n(Q^2)$ and magnetic $G_M^p(Q^2) - G_M^n(Q^2)$ iso-vector form factors of the nucleon from this summary. The green points indicate the experimental data. The lattice data are from various kinds of lattice formulations of QCD like twisted mass fermions (TMF), domain-wall fermions (DW), mixed action formulation (sea and valence quarks are treated differently) and clover Fermions. These simulations have been done at a pion mass of roughly 300MeV but with different numbers of dynamical flavors.

The lattice data for the electric form factor are in very good agreement with each other, although they cannot reproduce the experimental data. This is may be due to the fact that the pion mass is twice as high as the experimental value. The extrapolation to the physical point is usually done with a special form of Heavy Baryon Chiral Perturbation Theory (HBChPT) where degrees of freedom of the Δ-baryon are taken into account. This is the so called Small Scale Expansion (SSE). However, even with this kind of extrapolation the value from lattice QCD is significantly smaller than the experimental one.

The situation seems to be much better for the magnetic form factor which is shown in the right panel of fig. 1.1. It is hard to see, but the extraction of the radius and magnetic moment would lead to significantly smaller values than the experimental. However, a combined SSE fit to the magnetic moment and the radius for several pion masses compensates these deviations. An extrapolation to the physical point reproduces the experimental data within the statistical errors of the simulations [56].

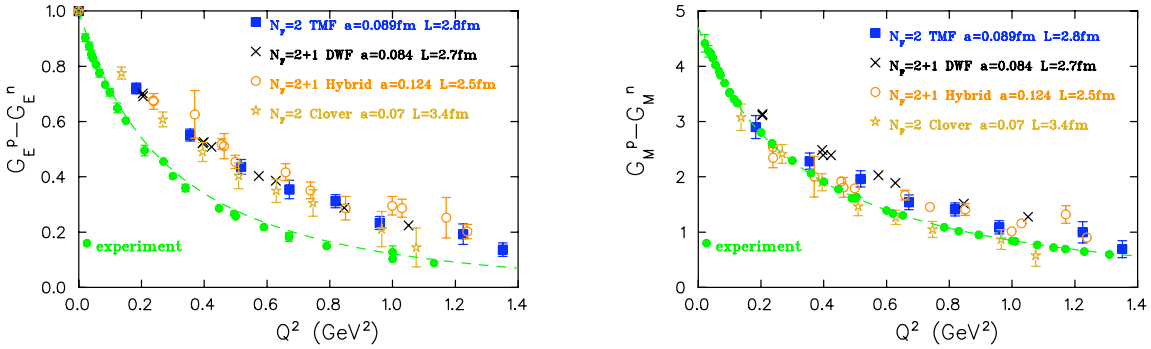

Figure 1.1: Comparison of the iso-vector electro-magnetic form factor of the nucleon from lattice QCD for various kinds of lattice formulations presented at the lattice conference in 2010 [2].

The axial charge g_A plays a central role in QCD at low energies, it can be easily computed with lattice QCD compared to other observables and it is experimentally very well know. Thus, g_A could be a new "benchmark observable" in up to date lattice simulations. Figure 1.2 shows the axial charge g_A as a function of the quark mass. The experimental value is represented by the black asterisk and lattice data by the colored points. All lattice data are systematically smaller than the experimental value and a chiral extrapolation would lead to significantly smaller values than the experimental one. So far, lattice QCD fails to reproduce the experimental value and the "benchmark" is not reached.

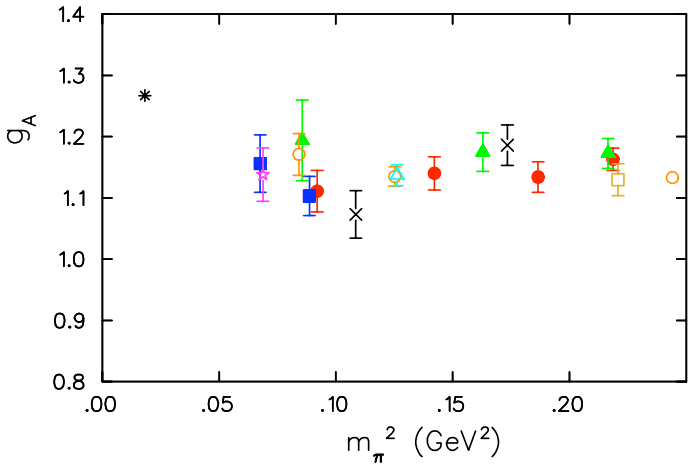

Figure 1.2: The axial charge of the nucleon from lattice QCD for various kinds of lattice formulations presented at the lattice conference in 2010 [2].

The perspective for form factor data computed in lattice QCD is by far worse than for hadron masses. The deviation from experiment cannot be explained from large pion masses only. Effects like cut-off or volume effects have been investigated already [5, 3], but it seems that they are not large enough to explain the discrepancies. If QCD is the correct theory of strong interactions, other systematic effects must influence the computation of nucleon form factors in lattice QCD. To clarify this issue is the goal of this thesis.

Chapter 2

Lattice QCD

Lattice QCD provides a frame work to calculate hadronic quantities non-perturbatively and from first principles. This chapter presents instructions to build up a theory on a lattice. The Φ^4-theory will be used as an easy example to show relevant techniques. It will be shown how to discretize gauge fields and the Dirac operator on the lattice with this knowledge. The chapter will end with a brief introduction into lattice simulation techniques and a discussion of systematic effects.

2.1 Euclidean lattice quantization of the Φ^4-Theory

A theory can be quantized on a lattice in principle in four steps.

1. The first step is the definition of the classical action in the continuum in Euclidean space time. For the Φ^4-theory this is

$$S_E[\Phi] = \int d^4x \left\{ \frac{1}{2}\partial_\mu \Phi(x)\partial_\mu \Phi(x) + \frac{1}{2}m^2\Phi(x)^2 + \frac{\lambda}{4!}\Phi(x)^4. \right\} \tag{2.1}$$

2. The second step is the discretization of the action. A hyper-cubic lattice

$$\Lambda_E = \left\{ x \in R^4 \,\middle|\, x^0/a = 1, ..., N_t; x^j/a = 1, ..., N_s, j = 1, 2, 3 \right\} \tag{2.2}$$

can be introduced as the set of discrete space-time points. The lattice spacing is given by *a*, the number of lattice sites by $N_t \times N_s^3$, and the physical space-time volume by $V = T \times L^3 = N_t \cdot a \times (N_s \cdot a)^3$.
Field-theoretical objects can be assigned to the lattice sites or the links between the sites. In the case of the Φ^4-theory the only free field is the Φ-field which lives on a lattice site x_n. It follows that the discretized action is given by

$$S_E[\Phi] = a^4 \sum_{x \in \Lambda_E} \left\{ \frac{1}{2} d_\mu \Phi(x) d_\mu \Phi(x) + \frac{1}{2} m^2 \Phi(x)^2 + \frac{\lambda}{4!} \Phi(x)^4 \right\}, \tag{2.3}$$

with the forward and backward derivatives:

$$d_\mu \Phi(x) = \frac{1}{a}(\Phi(x + a\hat{\mu}) - \Phi(x)), \tag{2.4}$$

$$d_\mu^* \Phi(x) = \frac{1}{a}(\Phi(x) - \Phi(x - a\hat{\mu})). \tag{2.5}$$

The vector $\hat{\mu}$ is the unit vector in μ-direction. A dual lattice Λ_E^* in momentum space can be introduced via the discrete Fourier transformation

$$\Lambda_E^* = \left\{ p \in R^4 \,\middle|\, p^0 = \frac{2\pi}{T} n^0, p^j = \frac{2\pi}{L} n^j, j = 1,2,3 \right\} \tag{2.6}$$

where $n_0 = -\frac{N_t}{2}, ..., (\frac{N_t}{2} - 1)$ and $n_j = -\frac{N_s}{2}, ..., (\frac{N_s}{2} - 1)$. The Fourier transformation of a field Φ is defined in one dimension as

$$\widetilde{\Phi}(p) = \sum_{n=1}^{L} e^{-ipna} \Phi(x_n), \tag{2.7}$$

which can be easily expanded to higher dimensions. In four dimensions it follows directly that the momenta p^0 and p^j are quantized in units of $2\pi/T$ and $2\pi/L$ respectively. A natural momentum cut-off $\Lambda = \pi/a$ is introduced. The momentum p_μ has to be in the first Brillouin zone

$$-\frac{\pi}{a} < p_\mu \leq \frac{\pi}{a}. \tag{2.8}$$

This means that the lattice itself acts as a regulator.
It can be seen that the discretization of the action is not unique. One could use different definitions for the derivative d_μ or the potential $V(\Phi)$ as long as they describe the same formal continuum limit $a \to 0$.

3. The third step is the quantization via the path integral formalism. The path integral is defined as

$$Z_E := \int \mathfrak{D}[\Phi]\, e^{-S_E[\Phi]}. \tag{2.9}$$

In this quantization the integration measure $\mathfrak{D}[\Phi]$ has the interpretation of an ordinary multiple-dimensional integration

$$\mathfrak{D}[\Phi] = \prod_{x \in \Lambda_E} \mathrm{d}\,\Phi(x). \tag{2.10}$$

Like in the continuum a generating functional and correlation functions can be defined. With the definition of a scalar product

$$(\Phi_1, \Phi_2) = a^4 \sum_{x \in \Lambda_E} \Phi_1(x)\Phi_2(x), \tag{2.11}$$

the free part of the action can be rewritten as

$$S_E[\Phi] = \frac{1}{2}(\Phi, K\Phi) \tag{2.12}$$

with the linear operator

$$K = -d^*_\mu d_\mu + m^2. \tag{2.13}$$

The n-point correlation function can then be defined as

$$\langle \Phi(x_1)...\Phi(x_n) \rangle = \frac{1}{Z_E} \int \prod_{x \in \Lambda_E} \mathrm{d}\,\Phi(x)\; \Phi(x_1)...\Phi(x_n) e^{-S_E[\Phi]}. \tag{2.14}$$

These correlation functions contain all informations of the theory in Euclidean space-time and they approach the Schwinger functions in the continuum limit. The Osterwalder and Schrader criteria assures that the information in Minkowski space-time can be reconstructed out of the Schwinger functions [85].
With the definition of an external field J(x), the generating functional W[J] is given by

$$e^{W[J]} := \left\langle e^{(J,\Phi)} \right\rangle = \frac{1}{Z_E} \int \prod_{x \in \Lambda_E} \mathrm{d}\,\Phi(x)\; e^{-S_E[\Phi]}\; e^{(J,\Phi)}. \tag{2.15}$$

The correlation function can be obtained by differentiating the generating functional with respect to the external field

$$\begin{aligned} \frac{\partial}{\partial J(x)} e^{W[J]} &= a^4 \left\langle \Phi(x) e^{(J,\Phi)} \right\rangle , \qquad (2.16) \\ \frac{\partial^2}{\partial J(x_1)\partial J(x_2)} e^{W[J]}|_{J=0} &= (a^4)^2 \left\langle \Phi(x_1)\Phi(x_2) \right\rangle , \qquad (2.17) \\ &\vdots \quad , \end{aligned}$$

where the relation between the generating functional W[J] and the operator K in the free case can be computed via

$$e^{W[J]} = \frac{1}{Z_E} \int \prod_{x \in \Lambda_E} \mathrm{d}\,\Phi(x)\; e^{-\frac{1}{2}(\Phi, K\Phi) + (J,\Phi)}. \qquad (2.18)$$

Rewriting the exponent

$$\begin{aligned} &-\frac{1}{2}(\Phi - K^{-1}J, K(\Phi - K^{-1}J)) + (J, K^{-1}J) = \\ &= -\frac{1}{2}\left\{(\Phi, K\Phi)) - (K^{-1}J, K\Phi) - (\Phi, J) + (K^{-1}J, J)\right\} + \frac{1}{2}(J, K^{-1}J), \end{aligned}$$

leads to

$$\begin{aligned} \Rightarrow\; e^{W[J]} &= e^{\frac{1}{2}(J,K^{-1}J)} \frac{1}{Z_E} \int \prod_{x \in \Lambda_E} \mathrm{d}\,\Phi(x) \exp\left\{ -\frac{1}{2} \underbrace{(\Phi - K^{-1}J)}_{\Phi`} \underbrace{K(\Phi - K^{-1}J)}_{\Phi`} \right\} = \\ &= e^{\frac{1}{2}(J,K^{-1}J)}. \qquad (2.19) \end{aligned}$$

The inverse operator K^{-1} has to be calculated. This can be done via a Fourier transformation which leads to a diagonal form of the operator K. The Fourier transformation of the external source is given by

$$J(x) = \frac{1}{L^3 \cdot T} \sum_{p \in \Lambda_E^*} e^{ipx} \tilde{J}(p) \quad , \quad \tilde{J}(p) = a^4 \sum_y e^{-ipy} J(y). \qquad (2.20)$$

With the definition of the discretized Laplacian operator

$$d_\mu^* d_\mu f(x) = \frac{1}{a^2}\{f(x + a\widehat{\mu}) + f(x - a\widehat{\mu}) - 2f(x)\} \qquad (2.21)$$

the Fourier transformation of the operator K which acts on the external field J(x) can be computed

$$KJ(x) = \frac{1}{L^3 \cdot T} \sum_{p \in \Lambda_E^*} (Ke^{ipx}) \tilde{J}(p). \tag{2.22}$$

The operator K acts on the exponential as follows:

$$\begin{aligned} Ke^{ipx} &= (-d_\mu^* d_\mu + m^2) e^{ipx} = \\ &= -\frac{1}{a^2}(e^{ip(x+a\widehat{\mu})} + e^{ip(x-a\widehat{\mu})} - 2e^{ipx}) + m^2 e^{ipx} = \\ &= \{-\frac{1}{a^2}(e^{ip_\mu a} + e^{-ip_\mu a} - 2) + m^2\} e^{ipx} = \\ &= \{-\frac{4}{a^2}\sin(\frac{p_\mu a}{2}) + m^2\} e^{ipx} \\ &= (\widehat{p}^2 + m^2) e^{ipx}, \end{aligned} \tag{2.23}$$

with $p \cdot \widehat{\mu} := p_\mu$ and $\widehat{p}_\mu := \frac{2}{a}\sin(\frac{p_\mu a}{2})$. This means that the operator K is just a multiplication with $(\widehat{p}^2 + m^2)$. The inversion of K is straight forward:

$$\begin{aligned} (K^{-1}J)(x) &= \frac{1}{L^3 \cdot T} \sum_{p \in \Lambda_E^*} (K^{-1} e^{ipx}) \tilde{J}(p) = \\ &= \frac{1}{L^3 \cdot T} \sum_{p \in \Lambda_E^*} (\widehat{p}^2 + m^2)^{-1} e^{ipx} \underbrace{\tilde{J}(p)}_{= a^4 \sum_y e^{-ipy} J(y)} = \\ &= a^4 \sum_y \frac{1}{L^3 \cdot T} \sum_{p \in \Lambda_E^*} \frac{e^{ip(x-y)}}{\widehat{p}^2 + m^2} \, J(y) = \\ &= a^4 \sum_y \mathrm{G}(x-y) \, J(y), \end{aligned} \tag{2.24}$$

where $\mathrm{G}(x-y)$ is the Green's function of K. The generating functional can be rewritten by inserting eq. 2.24 in eq. 2.19

$$e^{W[J]} = \exp\left\{ \frac{1}{2} a^4 \sum_{x,y} J(x) \; \mathrm{G}(x-y) \; J(y) \right\}, \tag{2.25}$$

where the propagator becomes

$$\langle \Phi(x)\Phi(y) \rangle = \frac{1}{(a^4)^2} \frac{\partial^2}{\partial J(x) \partial J(y)} e^{W[J]}|_{J=0} = \mathrm{G}(x-y). \tag{2.26}$$

The expansion of the lattice momentum $\widehat{p}_\mu$ in a leads to the Euclidean momentum

$$\widehat{p}_\mu = p_\mu + \mathcal{O}(a^2) \tag{2.27}$$

up to $\mathcal{O}(a^2)$ discretization effects.
In the continuum limit ($a \to 0$) the Green's function becomes the Feynman propagator in Euclidean space-time. Particle masses are defined through poles in this propagator. For the free part of the Φ^4-theory this is $(\widehat{p}_\mu^2 + m^2)^{-1}$, where $\widehat{p}_\mu = \frac{2}{a}\sin(\frac{p_\mu a}{2})$ is a periodic function with a period of $\frac{2\pi}{a}$. It follows that the poles and hence the particle masses are uniquely determined modulo $\frac{2\pi}{a}$. That means that the mass spectrum is unique in the first Brillouin zone.

4. The fourth step is the determination of the possible particle spectrum. This can be computed via the relation between the correlation function and the eigenvalues E_α of the Hamiltonian H of the system. A complete basis $|\alpha\rangle$ of the Hilbert space $\mathcal{H}$ of the Hamiltonian is needed. On this Hilbert space an operator $\mathbb{T}$ exists which acts on the state $|\alpha\rangle$ like

$$\mathbb{T}|\alpha\rangle = \lambda_\alpha|\alpha\rangle \quad \lambda_\alpha\text{: eigenvalues,} \tag{2.28}$$

and has the explicit form

$$\text{where } \mathbb{T} = e^{-aH} \quad , \quad \lambda_\alpha = e^{-aE_\alpha}. \tag{2.29}$$

$\mathbb{T}$ is the transfer matrix and describes the propagation of a particle by one lattice point in Euclidean time. The functional integral and the fields can be rewritten in terms of $\mathbb{T}$ like

$$\begin{aligned} Z_E &= \int \mathfrak{D}[\Phi]\, e^{-S_E[\Phi]} = \mathrm{Tr}\ \mathbb{T}^{\frac{T}{a}} \\ &= \sum_\alpha \lambda_\alpha^{\frac{T}{a}} = \sum_\alpha e^{-TE_\alpha}, \end{aligned} \tag{2.30}$$

$$\Phi(\vec{x}, T) = \mathbb{T}^{\frac{T}{a}}\, \Phi(\vec{x}, 0) = e^{-TH}\, \Phi(\vec{x}, 0). \tag{2.31}$$

With the completeness relation of the Hilbert space and the above equations the two-point correlation function for large time intervals $T \to \infty$ can be computed:

$$\begin{aligned}\langle\Phi(x)\Phi(y)\rangle &= \frac{1}{Z_E}\int \mathfrak{D}[\Phi]\ \Phi(x)\Phi(y)\ e^{-S_E[\Phi]} \\ &= \frac{1}{\mathrm{Tr}\,\mathbb{T}^N}\,\mathrm{Tr}\{\mathbb{T}^{N_0}\ \Phi(\vec{x},0)\ \mathbb{T}^{N_1}\ \Phi(\vec{y},0)\ \mathbb{T}^{N_2}\},\end{aligned}$$

where the shorthand notations $N = \frac{T}{a}$, $N_0 = -\frac{x_0}{a}$, $N_1 = \frac{x_0 - y_0}{a}$ and $N_1 = \frac{T+y_0}{a}$ were used. Inserting the completeness relation leads to

$$\begin{aligned}&= \frac{1}{\mathrm{Tr}\,\mathbb{T}^N}\,\mathrm{Tr}\{\mathbb{T}^{N_0+N_2}\ \underbrace{1}_{\sum_\alpha |\alpha\rangle\langle\alpha|}\ \Phi(\vec{x},0)\ \mathbb{T}^{N_1}\ \underbrace{1}_{\sum_\beta |\beta\rangle\langle\beta|}\ \Phi(\vec{y},0)\} \\ &= \frac{1}{\sum_\alpha e^{-TE_\alpha}}\sum_{\alpha,\beta}\{\langle\beta|\Phi(\vec{y},0)e^{-H(T-(x_0-y_0))}|\alpha\rangle\langle\alpha|\Phi(\vec{x},0)e^{-H(x_0-y_0)}|\beta\rangle\} \\ &= \frac{1}{\sum_\alpha e^{-TE_\alpha}}\sum_{\alpha,\beta} e^{-E_\alpha(T-t)}\{\langle\beta|\Phi(\vec{y},0)|\alpha\rangle e^{-E_\beta t}\langle\alpha|\Phi(\vec{x},0)|\beta\rangle\}, \quad t = |x_0 - y_0|.\end{aligned} \tag{2.32}$$

It is assumed that only the ground state contributes for large Euclidean times ($T \to \infty; t \ll T$):

$$\sum_\alpha e^{-TE_\alpha} = e^{-TE_0}(1 + O(e^{-TE_1})), \tag{2.33}$$

where $E_1 > E_0$. This leads to the final expression

$$\langle\Phi(x)\Phi(y)\rangle = \sum_\beta \langle\beta|\Phi(0,\vec{y})|0\rangle\, e^{-(E_\beta - E_0)t}\, \langle 0|\Phi(0,\vec{x})|\beta\rangle\,. \tag{2.34}$$

The energy of the vacuum is given by E_0 and the mass of the particle by $E_\beta - E_0$. The mass spectrum is determined by the exponential fall-off of the two-point function, and the matrix element $\langle 0|\Phi(0,\vec{x})|\beta\rangle$ contains informations about the overlap between the state β and the vacuum. Other observables like matrix elements can be computed from n-point functions in a similar way. This is the basis for numerical simulations and will be worked out in detail for mesons and baryons in lattice QCD in chapter 3.

2.2 Lattice gauge fields

The quantization of QCD gauge fields on the lattice works in the same way as it was shown for the Φ^4-theory. The classical Euclidean Yang-Mills action in the continuum is given by

$$S_E[A] = -\frac{1}{2g_0^2}\int \mathrm{d}^4\, x\, \mathrm{Tr}(F_{\mu\nu}(x)F_{\mu\nu}(x)). \tag{2.35}$$

$F_{\mu\nu}$ is the well known field strength tensor

$$F_{\mu\nu} = \partial_\mu A_\nu - \partial_\nu A_\mu + [A_\mu, A_\nu], \tag{2.36}$$

where A_μ is an element of the Lie algebra su(N). A_μ can be written as

$$A_\mu = A_\mu^c T^c, \tag{2.37}$$

where A_μ^c is a real vector field and T^c a generator of the gauge group. The index *c* runs from 1 to N^2-1 where N is the number of colors which is three for QCD. The non-Abelian continuum gauge transformation of the fields is given by

$$A_\mu(x) \longrightarrow g(x)A_\mu(x)g^{-1}(x) + g(x)\partial_\mu g^{-1}(x), \tag{2.38}$$

$$F_{\mu\nu}(x) \longrightarrow g(x)F_{\mu\nu}g^{-1}(x). \tag{2.39}$$

The discretization of gauge fields is more involved than for the fields in the Φ^4-theory. The naive ansatz $A_\mu(x),\ x \in \Lambda_E$ fails because eq. 2.38 does not longer hold when the continuum derivative ∂_μ is replaced by its discretized counterpart. A new method for the discretization of the gauge fields is needed. The idea is to use a parallel transporter on the lattice which is represented graphically in fig. 2.1.

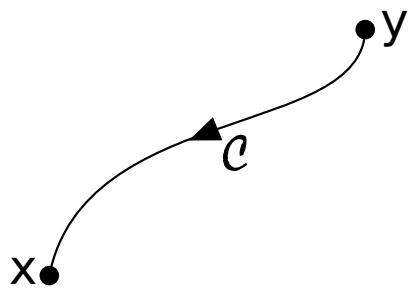

Fig. 2.1: Parallel transporter in the continuum

The curve $\mathcal{C}$ is parametrized by $z(t)$ where $0 \leq t \leq 1$ and $z(0) = y, z(1) = x$. The differential equation for the parallel transporter is given by

$$\left\{ \frac{\mathrm{d}}{\mathrm{dt}} + \dot{z}^{\mu} A_{\mu}(z) \right\} v(t) = 0, \tag{2.40}$$

which can be solved by

$$v(t) = \text{P.O. exp} \left\{ - \int_{y}^{x} \mathrm{d}\, z^{\mu} A_{\mu}(z) \right\} v(0). \tag{2.41}$$

P.O. means path ordered which means that the direction of the path is important. The parallel transporter from y to x along $\mathcal{C}$ is given by

$$U(\mathcal{C}(x,y)) = \text{P.O. exp} \left\{ - \int_{y}^{x} \mathrm{d}\, z^{\mu} A_{\mu}(z) \right\} \tag{2.42}$$

which is an element of he group SU(N). The lattice version of the parallel transporter is called link variable $U_{\mu}(x,y)$ and it connects two neighboring lattice sites x and y in μ-direction. Two link variables are shown in fig. 2.2 and 2.3.

Figure 2.2: $U(x, x + a\widehat{\mu}) \equiv U_{\mu}(x)$

Figure 2.3: $U(x + a\widehat{\mu}, x) = U(x, x + a\widehat{\mu})^{-1} = U_{\mu}(x)^{-1} = U_{\mu}(x)^{\dagger}$

As mentioned before, the gauge field A_{μ} is an element of the Lie algebra su(N) but the link variable $U_{\mu}(x)$ is an element of the group SU(N). It stands to reason to define

$$U_{\mu}(x) = e^{-aA_{\mu}(x)}. \tag{2.43}$$

This definition is not unique but one can always find a link variable to a given field $A^c_\mu(x)$ which approximates the field for small *a*

$$U_\mu(x) := e^{aA^c_\mu(x)} = 1 + aA^c_\mu(x) + O(a^2). \tag{2.44}$$

It follows

$$A^c_\mu(x) = \lim_{a\to 0} \frac{1}{a}\,(U_\mu(x) - 1). \tag{2.45}$$

The gauge transformation of the link variable on the lattice follows from eq. 2.38

$$U_\mu(x) \longrightarrow g(x)U_\mu(x)g^{-1}(x + a\widehat{\mu}), \qquad g(x), g(x + a\widehat{\mu}) \in \text{SU(N)}. \tag{2.46}$$

This means that a closed loop C on the lattice is always gauge invariant. These closed loops are called Wilson loops W(C)

$$W(C) = \mathrm{Tr}\{U^C(x, x)\}. \tag{2.47}$$

A possible way to discretize the gauge action is the Wilson plaquette action [103]. A so called plaquette has to be build which is shown in fig. 2.4.

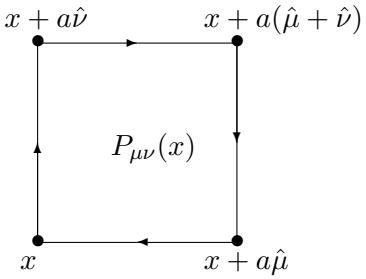

Figure 2.4: A plaquette $P_{\mu\nu}(x)$ is defined through a multiplication of four link variables.

The plaquette itself is a product of four link variables starting at a point x and going in the $\mu - \nu$-direction. Its continuum limit is:

$$\begin{aligned} &\mathrm{Tr}\left\{\, U_\nu(x)\, U_\mu(x + a\widehat{\nu})\, U^{-1}_\nu(x + a\widehat{\mu}) U^{-1}_\mu(x)\right\} = \mathrm{Tr}\{P_{\mu\nu}(x)\} \\ &\xrightarrow[a\to 0]{} N + \frac{a^4}{2}\,\mathrm{Tr}\{F^c_{\mu\nu}F^c_{\mu\nu}\} + O(a^5). \end{aligned} \tag{2.48}$$

The Wilson plaquette action can be build of these plaquettes:

$$S_E[U] = \beta \sum_{x \in \Lambda_E} \frac{1}{2} \sum_{\mu,\nu} \left(1 - \frac{1}{N} \operatorname{Tr} P_{\mu\nu})(x) \right). \tag{2.49}$$

In the continuum limit this becomes

$$\begin{aligned} S_E[U] &= \frac{\beta}{2} \sum_{x \in \Lambda_E} \sum_{\mu,\nu} \{1 - 1 - \frac{a^4}{2N} \operatorname{Tr} \left(F^c_{\mu\nu}(x) F^c_{\mu\nu}(x) \right) \} + O(a^5) \\ &= -\frac{\beta}{4N} \underbrace{a^4 \sum_{x \in \Lambda_E}}_{\to \int \mathrm{d}^4 x} \sum_{\mu,\nu} \operatorname{Tr} \left(F^c_{\mu\nu}(x) F^c_{\mu\nu}(x) \right) + O(a^5) \\ &\xrightarrow[a \to 0]{} -\frac{1}{2g_0^2} \int \mathrm{d}^4 x \operatorname{Tr} \left(F^c_{\mu\nu}(x) F^c_{\mu\nu}(x) \right), \end{aligned}$$

which is the continuum gauge action of eq. 2.35 where the parameter β is directly related to the bare gauge coupling via

$$\beta = \frac{2N}{g_0^2}. \tag{2.50}$$

In pure lattice gauge theory this would be the only free parameter which would automatically set the lattice spacing a. The determination of the lattice spacing with two flavors of dynamical quarks will be presented in chapter 4.
The gauge action can be quantized via its generating functional

$$Z_E = \int \mathfrak{D}[U] \, e^{-S_E[U]} = \int \prod_{x \in \Lambda_E} \prod_{\mu=0}^{3} \mathrm{d}\, U_\mu(x) \, e^{-S_E[U]}, \tag{2.51}$$

where $\mathrm{d}\, U_\mu(x)$ is the invariant group measure for compact Lie groups. This measure can be normalized

$$\int_{SU(N)} \mathrm{d}\, U = 1. \tag{2.52}$$

and is called Haar measure [45].
It should be mentioned here that the definition of the gauge action is not unique. Other closed loops could be used to reduce discretization effects but these definitions need usually more multiplications of links variables and are hence more expensive in terms of computer time.

2.3 Dirac operators

The fermionic part of QCD is defined in the continuum as

$$S_F[\Psi,\overline{\Psi},A]=\sum_{f=1}^{N_f}\int \mathrm{d}^4\mathrm{x}\,\overline{\Psi}^{(f)}_{\alpha,a}(x)\left\{(\gamma_\mu)_{\alpha\beta}\left(\delta_{ab}\partial_\mu+iA^{ab}_\mu(x)\right)+m^{(f)}\delta_{ab}\delta_{\alpha\beta}\right\}\Psi^{(f)}_{\beta,b}(x) \tag{2.53}$$

where $\Psi^{(f)}_{\alpha,a}(x)$ is a quark spinor which carries Dirac and color indices. Dirac indices are always represented by greek letters and color indices by latin ones. Exception are the greek letters μ and ν which are always used for the four space-time components.
The sum in eq. 2.53 runs over all flavors N_f. All quarks couple in the same way to the gauge fields and differ only by their electric charge and mass $m^{(f)}$. An explicit representation of the Dirac matrices γ_μ can be found in appendix B.
The naive way of discretization of the fermion action follows exactly the same steps discussed for the Φ^4-theory. The only difference is the definition of the covariant derivative

$$D_\mu(x)=\partial_\mu+A_\mu(x). \tag{2.54}$$

The link variables defined in the previous section have to be build into the discretized forward and backward derivatives of eq. 2.4 and 2.5 to make them covariant. A combination of both derivatives assures that the Dirac operator is hermitian. This leads to the discretized covariant derivative

$$D^{\text{lat}}_\mu\psi(x)=\left(d_\mu+d^*_\mu\right)^{\text{cov.}}\psi(x)=\frac{1}{2a}\left(U_\mu(x)\psi(x+\hat{\mu})-U_\mu(x-\hat{\mu})^\dagger\psi(x-\hat{\mu})\right) \tag{2.55}$$

This derivative can be graphically represented as:

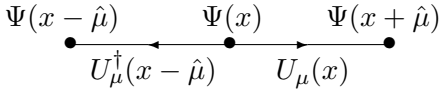

Figure 2.5: The covariant derivative discretized on a lattice.

With this definition the fermion action becomes on the lattice

$$\begin{aligned} S_F[\Psi,\overline{\Psi},U] &= a^4 \sum_{x\in\Lambda} \overline{\Psi}(x) \left\{ \frac{1}{2a}\gamma_\mu \left(U_\mu(x)\Psi(x+\hat{\mu}) - U_\mu(x-\hat{\mu})^\dagger \Psi(x-\hat{\mu}) \right) + m\Psi(x) \right\} \\ &\equiv a^4 \sum_{x,y\in\Lambda} \overline{\Psi}(x) M^N_{xy}[U] \Psi(y). \end{aligned} \tag{2.56}$$

The gauge invariance of the gauge action can be shown with the definition of the gauge transformation in eq. 2.46 and the transformation of the quark fields

$$\Psi(x) \to g(x)\Psi(x), \qquad \overline{\Psi}(x) \to \overline{\Psi}(x) g(x)^{-1}. \tag{2.57}$$

Taking the continuum limit by a Taylor expansion of $\Psi(x+\hat{\mu})$ and $U_\mu(x)$ lead directly to the continuum version of the fermion action with discretization effects of $\mathcal{O}(a^2)$.
The explicit form of the interactions matrix $M^N_{xy}[U]$ is given by

$$M^N_{xy}[U] = m\delta_{xy} + \frac{1}{2a}\gamma_\mu \left(U_\mu(x)\delta_{x,y+\hat{\mu}} - U_\mu(x-\hat{\mu})^\dagger \delta_{x,y-\hat{\mu}} \right). \tag{2.58}$$

Following the discretization steps of the Φ^4-theory and assuming no gauge interaction ($U_\mu(x) = 1$) leads to the inverse quark propagator of the naive fermion matrix:

$$S^{-1}(p) = m + \frac{i}{a}\gamma_\mu \sin(ap_\mu). \tag{2.59}$$

At zero spatial momentum $\vec{q} = 0$ and after a Wick rotation to Minkowski space: $p_0 \to iE$ and $\sin(ap_0) \to i\sinh(aE)$, the pole mass of the forward propagator is given by

$$am = \sinh(aE). \tag{2.60}$$

This shows that the continuum relation $E(\vec{p}=0) = m$ is violated by $\mathcal{O}(a^2)$-corrections even in the free field case .
Another interesting phenomenon can be derived from the propagator defined in eq. 2.59. The momentum has a hard cut-off within the first Brioullin zone. In the massless case a 16-fold degeneracy of the spectrum follows. This is due to the fact, that the *sine* becomes zero not only for $p_\mu = 0$ but also for $p_\mu = \pi$. The particle masses for $p_\mu = \pi$ are called doublers. These doublers are of course an unwanted feature because of the incorrect spectrum.

Wilson formulated a modified version of this action which should remove the doublers [104]. His solution was to add a dimension five operator $ar\overline{\Psi}\Box\Psi$ which gives the doublers a mass proportional to r/a. This fermion action is called Wilson action and has the form

$$\begin{aligned} S^W &= a^4 \sum_x \overline{\Psi}(x) \left\{ \frac{am+4r}{a}\Psi(x) + \right. \\ &\quad \left. + \frac{1}{2a}\left[(\gamma_\mu - r)U_\mu(x)\Psi(x+\hat{\mu}) - (\gamma_\mu + r)U_\mu(x-\hat{\mu})^\dagger \Psi(x-\hat{\mu})\right]\right\} \\ &\equiv a^4 \sum_{x,y\in\Lambda} \overline{\Psi}^r(x) M^W_{xy}[U] \Psi^r(y) \end{aligned} \tag{2.61}$$

where $M^W_{xy}[U]$ is the Wilson Dirac operator

$$M^W_{xy}[U] = \delta_{xy} - \kappa\left\{(r-\gamma_\mu)U_\mu(x)\delta_{x,y+\hat{\mu}} + (r+\gamma_\mu)U_\mu(x-\hat{\mu})^\dagger \delta_{x,y-\hat{\mu}}\right\}. \tag{2.62}$$

The quark fields $\Psi(x)$ have been rescaled with the hopping parameter

$$\kappa = \frac{1}{2am+8r} \tag{2.63}$$

and become

$$\Psi^r = \sqrt{am+4r}\Psi = \frac{1}{\sqrt{2\kappa}}\Psi. \tag{2.64}$$

The parameter κ is directly related to the quark mass via

$$am = \frac{1}{2\kappa} - 4r = \frac{1}{2\kappa} - \frac{1}{2\kappa_c}, \tag{2.65}$$

where κ_c is the critical value where the quark masses vanish. This definition will be used in chapter 6 to extract the quark mass.
It can be easily shown that for $r = 1$ the doublers are removed. The free Wilson quark propagator in momentum space is given by

$$S^W(p) = M_W^{-1}(p) = \frac{a}{1 - 2\kappa\sum_\mu (r\cos ap_\mu - i\gamma_\mu \sin ap_\mu)} \quad . \tag{2.66}$$

One can see in the massless case that for each value of p_μ where the *sine* becomes zero the *cosine* is non zero. The doublers get a mass proportional to r/a and only one pole is left at $p_\mu = 0$ and hence the correct spectrum is reproduced.

The removing of doublers does not come for free. An analysis of the pole mass of the Wilson action (like for the naive action) gives

$$am = r(\cosh aE - 1) + \sinh aE, \tag{2.67}$$

where it can directly be seen that the discretization effects are of $\mathcal{O}(a)$ which is worse compared to the naive action. However, the leading order discretization effects of Wilson's formulation can be shifted to $\mathcal{O}(a^2)$ with the so called Symanzik improvement program. It will be introduced in the section about systematic effects.
Another problem is that Wilson's formulation of the fermion action is not invariant under chiral symmetry in the massless case. Indeed it exists a no-go theorem by Nielsen and Ninomiya [82] which connects several properties of the fermion action. It says that it is not possible to construct a discretized massless fermion action which preserves the continuum formulation of chiral symmetry, has no doublers, is local and has the correct continuum limit. But there exists one way out. The chiral symmetry of the Dirac operator is given in the continuum by

$$\gamma_5 M + M\gamma_5 = 0. \tag{2.68}$$

This relation can be modified on the lattice like

$$\gamma_5 M + M\gamma_5 = aM\gamma_5 M, \tag{2.69}$$

where the relation of eq. 2.68 is restored in the continuum limit. This relation is called the Ginsparg-Wilson-relation [46]. It is possible to construct Dirac operators, so called Overlap operators, which respect this relation. Two different actions with these operators are known, the domain wall fermion action [63] and the Neuberger action [81]. For form factor calculations domain wall fermions are usually used rather than Neuberger fermions, so they will be discussed here in some detail.
To construct the domain wall fermion action, the four-dimensional lattice is expanded in a fifth dimension. Up to this fact the action is very similar to the Wilson action. It follows directly that the increase in computing time for overlap fermions compared to Wilson fermions is proportional to the number of lattice points in the fifth dimension N_5.
The four-dimensional physical quark fields live on the four-dimensional boundaries of the five-dimensional lattice and the color and Dirac structure are unchanged compared to Wilson fermions. All in all the domain wall action is build of the four-dimensional

Wilson-Dirac operator and a five-dimensional part, which is given by

$$\begin{aligned} M_5^{dw}(x,y) &= \delta_{x,y} - (1-\delta_{x,N_5-1})P_-\delta_{x+1,y} - (1-\delta_{x,0})P_+\delta_{x-1,y} \\ &+ \kappa(P_-\delta_{x,N_5-1}\delta_{0,y} + P_+\delta_{x,0}\delta_{N_5-1,y}), \end{aligned} \tag{2.70}$$

where $P_\pm = (1 \pm \gamma_5)/2$ are chiral projectors and κ is the four-dimensional mass parameter. This form implies that each four-dimensional slice is constructed from the same link variables and is hence identical. The boundary conditions are on the four-dimensional slices the same as for the Wilson action, namely periodic in spatial components and anti-periodic in time. The boundaries in the fifth dimension can be read of eq. 2.70 directly. In the massless case they are fixed at the boundaries at 0 and $N_5 - 1$ and only the term proportional to the mass parameter connects both ends.
The four-dimensional quark fields ψ can now be constructed from the five-dimensional fields Ψ via

$$\psi(x) = P_-\Psi(x,0) + P_+\Psi(x,N_5-1), \quad \overline{\psi}(x) = \Psi(x,N_5-1)P_- + \Psi(x,0)P_+ \tag{2.71}$$

which means, that they are located at the four-dimensional boundaries of the five-dimensional lattice. The chiral symmetry is achieved though because the chirality of the fermion fields depends on the side they life in the fifth dimension. The violation of chiral symmetry is exponentially suppressed by a factor proportional to the number of lattice points in the fifth dimension. The typical number of N_5 is $10 - 30$.

Other formulations of the fermions action than the Wilson and domain wall formulation are used for nucleon form factor calculation and they will be discussed in the following briefly.
A very similar formulation to the Wilson fermion action is the Twisted mass fermion action [97]. This formulation needs two degenerate quarks and differs from Wilson's formulation by the additional term $i\mu\gamma_5\tau_3$. The twisted mass parameter μ is a real number and the matrix τ_3 acts in flavor space only $\tau_3 = \mathrm{diag}(1,-1)$. The additional mass term acts as an infrared regulator and protects against exceptional configurations. The Dirac operator $M[U]$ itself depends on the individual configuration and hence also its eigenvalues which are given by

$$\kappa + \lambda_i[U] \tag{2.72}$$

where $\lambda_i[U]$ are the in general complex eigenvalues in the massless case and κ is the bare

quark mass parameter. Assuming that one of the $\lambda_i[U]$ is real and negative, the smallest eigenvalue of $M[U]$ is close to zero. This makes the inversion of the Dirac operator on these configurations numerically problematic. Such configurations are called exceptional (see e.g. [45]). In addition, the twisted mass formulation assures that the Dirac operator has only positive and real eigenvalues.
Another advantage is the automatic $\mathcal{O}(a)$-improvement at maximal twist [42]. This means that the parameter μ can be chosen in such a way that all contributions of $\mathcal{O}(a)$ vanish and only contributions of $\mathcal{O}(a^2)$ survive. The big disadvantage of this formulation is the flavor breaking due to the twisted mass term. The neutral and the charged pions are not degenerate like it would be for the Wilson action. This means that the later discussed excited state contributions may be larger than for Wilson fermions.

A completely different approach is the formulation for a fermion action with so called staggered or Kogut-Susskind fermions [64]. In this formulation not all 15 doubler of the naive fermion action get a mass. Four of them stay massless but in addition a subgroup of the chiral symmetry is preserved.
A space-time dependent variable transformation is used on the fermion fields which eliminates the Dirac matrices in the fermion action. This transformation mixes spinor and space-time indices in a way that the quark degrees are distributed on the corners of a hypercube on the lattice. The remaining four doublers are called tastes of staggered fermions. In a QCD simulation one would like to have two light and degenerate quark flavors (u- and d-quark) and maybe a heavy one (strange quark). This makes it necessary to take the square root of the fermion determinant to get two light quark flavors and the fourth root for the heavy quark flavor. Taking the root is not trivial from a conceptual perspective and is actually discussed, see e.g. [26].

2.4 The Hybrid Monte Carlo algorithm

The quantization of the fermion part of the QCD action can be done via the path integral formalism. Fermion degrees of freedom can be integrated out like in the continuum and the path integral for any fermion action S_F is given by

$$Z_F = \int \mathcal{D}[\overline{\Psi}, \Psi, U] e^{-S_F[\overline{\Psi}, \Psi, U]} = \int \mathcal{D}[U] \det M[U], \tag{2.73}$$

where M is the Dirac operator of the fermion action.
The action of full lattice QCD is a combination of the gauge action and the fermion action. The starting point of a simulation is the path integral

$$Z = \int \mathcal{D}[\overline{\Psi}, \Psi, U] e^{-S_F[\overline{\Psi},\Psi,U]-S_g[U]} = \int \mathcal{D}[U] \det(M[U]) e^{-S_g[U]}, \tag{2.74}$$

with any choice of the discretized fermion $S_F[U]$ and gauge $S_g[U]$ action. An observable can be computed via

$$\langle O \rangle = \frac{1}{Z} \int \mathcal{D}[U] \det(M[U]) e^{-S_g[U]} O[U], \quad \mathcal{D}[U] = \prod_{x,\mu} \mathrm{d}\, U_\mu(x), \tag{2.75}$$

where $\frac{1}{Z} \det(M[U]) e^{-S_g[U]}$ can be interpreted as a normalized probability density on the space of all configurations. The integral $\int \mathcal{D}[U]$ can not be computed analytically but it can be approximated numerically with Monte Carlo methods.
A set of N gauge field configurations $\{U_n\}$ must be generated, distributed with the probability $\det(M[U]) e^{-S_g[U]}$. The observable is than given by

$$\langle O \rangle \approx \frac{1}{N} \sum_{U_n} O[U_n] + \mathcal{O}(N^{-\frac{1}{2}}). \tag{2.76}$$

where the error $\mathcal{O}(N^{-\frac{1}{2}})$ is statistical because of the finite number of configurations.
For pure gauge theories one uses usually the heat bath algorithm [25] with overrelaxation. This does not work for dynamical simulations where the fermion determinant is not fixed. The method of choice is the so called hybrid Monte Carlo (HMC) algorithm in up to date simulations [37][1]. It is a molecular dynamic evolution in the computer or Markov time τ in the phase space of configurations where all link variables are updated simultaneously. This evolution is achieved by solving the Hamiltonian equation of motion

$$\dot{P} = -\frac{\partial H}{\partial Q} = -\frac{\partial S}{\partial Q}, \tag{2.77}$$

$$\dot{Q} = \frac{\partial H}{\partial P} = P, \tag{2.78}$$

[1] A very good introduction to the HMC-algorithm and the inversion of the Dirac operator can be found in [73]

where the Hamiltonian is defined as

$$H[Q,P] \equiv \frac{1}{2}P^2 + S[Q] \tag{2.79}$$

The variable Q corresponds to the link variables U_μ and P is its conjugate momentum. Starting from a given configuration U where the momentum field P is generated randomly according to the probability density proportional to $\exp\{-\frac{1}{2}P^2\}$. The next step is the integration of the Hamilton equations of motion from time $\tau = 0$ up to a given time $\tau = t$ of eq. 2.77 with a numerical integrator. This could be the leap-frog or the Omelyan [84] integrator. The numerical integration leads to numerical errors which can be compensated in an additional accept-reject step. The difference of the Hamiltonian of the new fields U' and the original fields U is given by

$$\Delta H = H(U',P') - H(U,P) \tag{2.80}$$

and a new configuration is then accepted or rejected according to the probability

$$P_{\text{acc.}} = \min\{1, e^{-\Delta H}\}. \tag{2.81}$$

If the new configuration is accepted it is the start configuration for a new integration step. If it is rejected the whole procedure is repeated with a new created conjugate momentum P.

One problem is the computation of the fermion determinant $\det(M[U])$. The lattice group in Mainz uses a HMC algorithm with two degenerated light quark flavors where the determinant can be written as $|\det(M[U])|^2$. The action is then given by

$$S[U] = S_g[U] - \ln|\det(M[U])|^2, \tag{2.82}$$

and it follows that the probability density $\frac{1}{Z}e^{-S[U]}$ is positive definite. This is necessary to assure the interpretation of a probability density. But the Dirac matrix is very large and its determinant cannot be computed directly. The determinant can be rewritten in terms of so called pseudo fermions

$$|\det(M[U])|^2 = \text{const} \cdot \int \mathcal{D}[\Phi] e^{-S_{\text{pf}}(U,\Phi)}, \quad \text{with} \tag{2.83}$$

$$S_{\text{pf}}(U,\Phi) = \Phi^\dagger M[U]^{-2}\Phi. \tag{2.84}$$

This step is necessary because fermions are Grassmann numbers which anti-commutate. It is currently not possible to implement Grassmann numbers in a simulation program. With the rewriting of the action with pseudo-fermions this problem is avoided, because the new fields Φ are usual complex numbers. The price for this method is the computation of the inverse of the fermion matrix $M[U]^{-2}$. This is the same as the computation of quark propagators which are needed for the computation of correlation functions in lattice QCD.
The configurations used in Mainz are created using the DD-HMC algorithm by Martin Lüscher [73]. DD stands for domain decomposition which is a geometric method to separate contributions to the fermion determinant from small eigenvalues from the ones of large eigenvalues. The lattice is divided into chess-board like sub-lattices where Ω denote all lattice points on a white sub lattice, Ω^* all points on a black sub lattice and $\partial\Omega$ and $\partial\Omega^*$ the corresponding boundary points. The fermion matrix can be rewritten:

$$M = M_\Omega + M_{\Omega^*} + M_{\partial\Omega} + M_{\partial\Omega^*}. \tag{2.85}$$

It follows that the determinant is then given by

$$\det M = \det M_\Omega \det M_{\Omega^*} \det \left\{1 - M_\Omega^{-1} M_{\partial\Omega} M_{\Omega^*}^{-1} M_{\partial\Omega^*}\right\}. \tag{2.86}$$

The computation of contributions from small eigenvalues are very expensive in terms of computing time but can be factorized from $\det M_\Omega \det M_{\Omega^*}$. They can be calculated on a local lattice with the modification that each local lattice must consist of a white and a black sub-lattice at minimum. This allows a very easy parallelization of the simulation algorithm.
The inversion of the Dirac operator is done by solving the system of linear equations

$$\sum_{z,b,\beta} M(x,z)^{ab}_{\alpha\beta} S(z,y)^{bc}_{\beta\gamma} = \eta(x,y)^{ac}_{\alpha\gamma} \tag{2.87}$$

iteratively, where $\eta(x,y)$ is a given source field, $M(x,z)$ is the Dirac operator and $S(z,y)$ the quark propagator and hence the solution of the system. To construct a propagator from a given point e.g. $x = 0$ to all other points y twelve inversion are needed. This is due to the fact that each combination of color and Dirac indices requires a new inversion. The choice of the source is arbitrary but some choices may be superior to others (see appendix C).

In the DD-HMC code a generalized conjugate residual (GCR) algorithm is implemented with an additional Schwarz pre-conditioner and low-mode deflation. This is necessary because the computation of quark propagators is very time consuming. In our measurement program roughly 80% of the computing time is spent for the inversion routine.
The inversion of the Dirac matrix becomes more and more expensive with decreasing pion mass. This is due to the fact that the eigenvalues become smaller with smaller masses. This means that the condition number of the matrix increases and hence more inversion steps are needed. For more details about the solver used see [92, 69, 70, 71, 72].

2.5 Systematic effects I

Systematic effects play a central role in all lattice QCD simulations. These effects will be discussed here in some detail. Systematic effects which do not come from the discretization itself but from the computation of correlation functions will be discussed in chapter 3.4.
Due to the discretization on the lattice, cut-off effects are introduced which are of order $\mathcal{O}(a)$ for Wilson fermions. The discretization effects of the gauge action are of $\mathcal{O}(a^2)$ and it would be good to shift the effects of the fermion action to this order. This can be done with the so called Symanzik improvement program [96]. First of all the correction terms have to be identified. They have to be ordered according to their dimension and have to be added to the action with suitable coefficients. The improved action for Wilson fermions is the so called clover action

$$S_C = S_W + c_{\mathrm{SW}} a^5 \overline{\Psi}(x) \frac{1}{2} \sigma_{\mu\nu} F_{\mu\nu}(x) \Psi(x), \tag{2.88}$$

where $F_{\mu\nu}$ is the lattice version of the field strength tensor defined in eq. 2.48. The improvement coefficient c_{SW} can be computed perturbatively [96] and non-perturbatively [76, 75] and depends on the bare coupling parameter g_0.
Using a $\mathcal{O}(a)$-improved action to generate gauge ensemble for measurements does not guarantee that all observables measured on this ensembles are automatically $\mathcal{O}(a)$-improved. Later on the vector and axial vector currents will be used. Both operators can be $\mathcal{O}(a)$-improved with the same method as for the action.

It follows

$$(A_I)_\mu(x) = A_\mu(x) + c_A a \partial_\mu P(x), \tag{2.89}$$
$$(V_I)_\mu(x) = V_\mu(x) + c_V a \partial_\nu T^{\nu\mu}(x), \tag{2.90}$$

with the pseudo-scalar density

$$P(x) = \overline{\Psi}(x)\gamma_5\Psi(x), \tag{2.91}$$

and the tensor field

$$T^{\nu\mu}(x) = \overline{\Psi}(x)\sigma^{\nu\mu}\Psi(x). \tag{2.92}$$

The determination of the improvement coefficients c_V and c_A is discussed in chapter 6. The vector and axial-vector currents are automatically improved for zero momentum transfer and spatial components. This will be an advantage when the axial charge will be computed, because it is extracted from the third component of the axial current at zero momentum transfer and hence it is automatically improved.
Cut-off effects must be controlled in general even for $\mathcal{O}(a)$-improved operators. It is not initially clear that these effects are small. We do simulations for three different lattice spacings to investigate discretization effects and we perform the continuum limit.

The limitation of computer power and the rise of cut-off effects limit the maximal size of lattice volumes. Assuming a lattice spacing smaller then 0.1 fermi and a maximal number of 64 lattice points in spatial direction limits the box size to 6.4 fermi. In modern simulations the lattice spacing is even smaller to minimize discretization effects, e.g. 0.05 fermi for our smallest lattice spacing. This would halve the physical box size to 3.2 fermi. Is this still large enough?
It was shown by Martin Lüscher [68] that the finite volume corrections for a particle in a sufficient large lattice with periodic boundary conditions in spatial directions falls off exponentially with its mass M like e^{-ML}. On a lattice with this kind of boundary conditions the particle can go a direct way from one point to another or it can cross the boundaries. The crossing of the boundary can be interpreted as a squeezing effect of the finite box (for a more detailed introduction see e.g. [45]). The lightest hadron in lattice QCD is the pion and hence, it has the largest Compton wavelength. It follows that the leading finite size effects come from the pion and that the box size must be large enough to ensure only small volume corrections for it. A rule of thumb says that the volume should be at least

three times larger than the Compton wave length of the pion: $m_\pi L > 3$. It will turn out later that this is maybe not large enough for hadronic matrix elements.
In addition to the one particle finite size effects other effects can show up when more than one particle in a finite box is described [77], e.g. for scattering processes. The interaction of the particles leads to the polynomial dependence $\mathcal{O}(1/L^3)$ of the finite size effects. This is due to the fact that the interacting particles have to be close to each other. The probability to find a particle close to another is inversely proportional to the spatial volume. However, these effects can be neglected for nucleon form factor calculations because no scattering processes are investigated.

The combination of volume and cut-off effects with the increasing computation costs for small pion masses make simulations at the physical pion mass extremely expensive. In a realistic simulation the lattice spacing is around 0.07 fm and $m_\pi L > 5$. This set-up would require 100 lattice points in one direction. The largest lattice computed within the Coordinated Lattice Effort (CLS) have 64 lattice points in spatial direction, a lattice spacing of 0.062 fm and a pion mass of roughly 200 MeV. The creation of this gauge ensemble requires roughly one million core hours to produce enough configurations for reasonable statistics. This means that an actual computer with four cores per processor would need roughly 30 years to compute this lattice. At the moment this lattice is created on the supercomputer JUGENE in Jülich with over 16000 processor cores in use. One should note that this is only the time to create the ensemble. The measurements of all observables of interest would require the same CPU time at least.
Actual simulations are usually done at significantly larger pion masses. The data presented later are computed on the ensembles summarized in appendix A where the pion mass varies between 270 and 600 MeV. The extrapolation to the physical point can be done with Chiral Perturbation Theory [95, 94]. For nucleon matrix elements Heavy Baryon Chiral Perturbation Theory (HBChPT) is used where Δ-baryon degrees of freedom are explicitly taken into account (small scale expansion (SSE)) [62, 12].

It was mentioned before that the lattice acts as a regulator because of the momentum cut-off π/a at the edge of the first Brioullin zone. This means that loop integrals in perturbation theory yield finite results. However, the formal continuum limit $a \to 0$ shifts the momentum cut-off to infinity and hence renormalization is needed to assure finite physical quantities. Even if everything stay finite, renormalization will be needed to compare lattice results with experimental data. The renormalization of quark masses and matrix

elements is discussed in chapter 6 when the final results of the simulations are presented.

It is clear that a careful investigation of systematic effects is necessary. Different limits have to be taken at the end of a simulation: the continuum limit for discretization effects, the infinite volume limit for volume effects, and a chiral extrapolation to the physical point. These effects can investigated with simulations at several combinations of pion masses, volumes, and lattice spacings. All in all twelve ensembles were used to create the data presented in this thesis. More ensembles with small pion masses and large volumes are currently under construction and will be included in the analysis at a later stage.

Chapter 3

Correlation functions

Almost all hadronic quantities like masses and matrix elements can be extracted in lattice QCD from Euclidean correlation functions. This chapter will introduce the computation of these correlation functions. The main examples will be the two- and three-point functions of the nucleon.

3.1 Two-point functions

In lattice QCD masses are extracted from two-point functions. The interpolating fields which create particles with the correct quantum numbers are [45]:

- pseudo-scalar mesons π, K: $J^P = u^a \gamma_5 d^b, \quad (u, d \to s)$
- vector mesons ρ, K^*: $J^V = u^a \gamma_i d^b, \quad (u, d \to s)$
- nucleon N: $J_\gamma = \epsilon^{abc}(u^a C\gamma_5 d^b)u^c_\gamma$
- delta-baryon Δ: $J^\Delta_{i,\gamma} = \epsilon^{abc}(u^a C\gamma_i d^b)u^c_\gamma$
- lambda-baryon Λ: $J^\Lambda_{i,\gamma} = \epsilon^{abc}(u^a C\gamma_i d^b)s^c_\gamma$
- omega-baryon Ω: $J^\Omega_{i,\gamma} = \epsilon^{abc}(s^a C\gamma_i s^b)s^c_\gamma$.

In this choice C is the charge conjugation matrix $C = i\gamma_0\gamma_2$, γ_i are the spatial gamma matrices where $i = 1, 2, 3$ and $\gamma_5 = \gamma_0\gamma_1\gamma_2\gamma_3$. Note that the gamma matrices are defined in Euclidean space time and their chiral representation was used. Their explicit form is shown in appendix B. Please note that the lattice spacing a is usually left out in mathematical expressions and calculations but it is included in pictures to avoid confusions with physical units.

3.1.1 The quark level

The two-point function of a nucleon can be written as

$$\left\langle \Gamma_{\gamma'\gamma} J_\gamma(x) \overline{J_{\gamma'}(0)} \right\rangle = -\epsilon^{abc}\epsilon^{a'b'c'} \Gamma_{\gamma'\gamma} \left\{ (u^a_\alpha)^T(x) \left[C\gamma_5\right]_{\alpha\beta} d^b_\beta(x) \right\} u^c_\gamma(x) \cdot \\ \cdot \overline{u^{c'}_{\gamma'}}(0) \left\{ \overline{d^{b'}_{\beta'}}(0) \left[C\gamma_5\right]_{\beta'\alpha'} (\overline{u^{a'}_{\alpha'}})^T(0) \right\}, \tag{3.1}$$

where a nucleon is created at the source via $\overline{J_{\gamma'}(0)}$ and annihilated at the sink via $J_\gamma(x)$. The matrix $\Gamma_{\gamma'\gamma}$ is a projection or polarization matrix which projects the interpolating baryon fields to the correct parity. The explicit form is $\Gamma = \frac{1}{2}(1 + \gamma_0)$ for unpolarized baryons. For nucleons polarized in the 3-direction is the polarization matrix given by $\Gamma = \frac{1}{2}(1 + \gamma_0)\frac{1}{2}(1 + i\gamma_5\gamma_3)$. The projection matrices are necessary because the interpolating fields for baryons do not project to the correct parity of the particle. It can be proved easily [45] that the nucleon interpolating field behaves under a parity transformation $\mathcal{P}$ (see table 3.2) like

$$J^i_\gamma(\vec{x}, t) \xrightarrow{\mathcal{P}} \gamma_0 J^i_\gamma(-\vec{x}, t). \tag{3.2}$$

After the projection a particle with definite parity is constructed which propagates forward in Euclidean time. Its parity partner propagates backwards in time due to anti-periodic boundary conditions in time.
Performing the Wick contractions of the quark fields

$$u^a_\alpha(x)\overline{u^b_\beta}(y) = [S^u(x, y)]^{ab}_{\alpha\beta}, \tag{3.3}$$

$$d^a_\alpha(x)\overline{d^b_\beta}(y) = \left[S^d(x, y)\right]^{ab}_{\alpha\beta}, \tag{3.4}$$

leads to

$$\begin{aligned}
&\left\langle \Gamma_{\gamma'\gamma} J_\gamma(x) \overline{J_{\gamma'}(0)} \right\rangle = \\
= \; & -\epsilon^{abc}\epsilon^{a'b'c'} \Gamma_{\gamma'\gamma} \left[C\gamma_5\right]_{\alpha\beta} \left[C\gamma_5\right]_{\beta'\alpha'} \left[S^d(x,0)\right]^{bb'}_{\beta\beta'} \cdot \\
& \cdot \left\{ \left[S^u(x,0)\right]^{cc'}_{\gamma\gamma'} \left[S^u(x,0)\right]^{aa'}_{\alpha\alpha'} - \left[S^u(x,0)\right]^{ac'}_{\alpha\gamma'} \left[S^u(x,0)\right]^{ca'}_{\gamma\alpha'} \right\} = \\
= \; & -\epsilon^{abc}\epsilon^{a'b'c'} \left\{ \mathrm{Tr}^{\mathrm{D}} \left[\Gamma S^{u;cc'}(x,0) \right] \mathrm{Tr}^{\mathrm{D}} \left[C\gamma_5 S^{d;bb'}(x,0) C\gamma_5 S^{u;aa'}(x,0) \right] - \right. \\
& \left. - \mathrm{Tr}^{\mathrm{D}} \left[C\gamma_5 S^{d;bb'}(x,0) C\gamma_5 S^{u;ac'}(x,0) \Gamma S^{u;ca'}(x,0) \right] \right\}, \qquad (3.5)
\end{aligned}$$

where the trace over the Dirac space Tr^{D} is explicitly written out in the last step. Equation 3.5 is the starting point of the numerical computation of the two-point function of a nucleon and the corresponding diagram is shown in fig. 3.1.

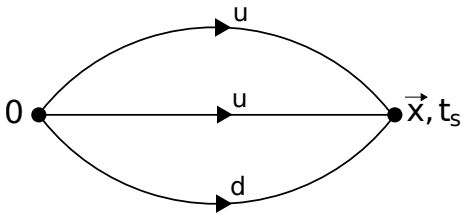

Figure 3.1: nucleon two-point function.

In our simulations the u- and d-quarks are degenerate. This means that only one propagator has to be calculated to build the full two-point function. The induction of momentum can be achieved via a spatial Fourier transformation. The two-point function of a nucleon finally becomes

$$C_2^{\text{baryon}}(t,q) = \sum_{\vec{x}} \left\langle \Gamma_{\gamma'\gamma} J_\gamma(x) \overline{J_{\gamma'}(0)} \right\rangle e^{-i\vec{p}\vec{x}}. \qquad (3.6)$$

3.1.2 The hadronic level

The correlation function for a baryon at the hadronic level can be written in Minkowski space as

$$C_2(t;\vec{p},\Gamma) = \sum_{\vec{x}} e^{-i\vec{p}\vec{x}} \Gamma_{\beta\alpha} \left\langle 0 \left| \chi_\alpha(x) \bar{\chi}_\beta(0) \right| 0 \right\rangle. \qquad (3.7)$$

With the completeness relation $\mathbb{1} = \sum_{p',s} \frac{1}{2p'_0} |p',s\rangle \langle p',s|$ where $p'_0 = \sqrt{\vec{p}'^2 + m^2}$ holds, and the translation operator $\chi(x) = e^{i\hat{p}x}\chi(0)e^{-i\hat{p}x}$ this becomes

$$C_2(t;\vec{p},\Gamma) = \sum_{\vec{x},p',s} \frac{1}{2p'_0} e^{-i\vec{p}\vec{x}} e^{-ip'x} \Gamma_{\beta\alpha} \left\langle 0 \left| \chi_\alpha(0) \right| p',s \right\rangle \left\langle p',s \right| \bar{\chi}_\beta(0) \left| 0 \right\rangle . \tag{3.8}$$

The matrix elements can be expressed by [66]

$$\langle 0| \chi_\alpha(0) \left| p',s \right\rangle = Z_B u(p',s). \tag{3.9}$$

Z_B represents the coupling strength of $\chi(0)$ to the baryon-state $|p',s\rangle$ while $u(p',s)$ is a usual Dirac spinor. Using this expression and combining both exponentials leads to

$$C_2(t;\vec{p},\Gamma) = \Gamma_{\beta\alpha} \sum_{p'_0} \frac{Z_B^2}{2p'_0} e^{-ip'_0 x_0} \sum_{\vec{x},\vec{p}',s} e^{-i(\vec{p}-\vec{p}')\vec{x}} u_\alpha(p',s)\bar{u}_\beta(p',s). \tag{3.10}$$

The spin-sum over the Dirac spinors can be evaluated [86] and the exponential representation of the δ-distribution can be used to get:

$$C_2(t;\vec{p},\Gamma) = \sum_{p_0} \frac{Z_B^2}{2p_0} \Gamma_{\beta\alpha} \left(-i\not{p} + m\right)_{\alpha\beta} e^{-ip_0 x_0}. \tag{3.11}$$

It is possible to make contact to eq. 3.5 by a Wick rotation $x_0 \to -it, p_0 \to iE$. Assuming that the ground state dominates this correlation function $\sum_{p_0} e^{-ip_0 x_0}/p_0 \to \sum_{E_p} e^{-E_p t}/E_p \approx e^{-\hat{E}_p t}/\hat{E}_p$, finally leads to

$$C_2^{\text{baryon, ground state}}(t;\vec{p},\Gamma) = C_2^{\text{b}}(t;\vec{p},\Gamma) = \frac{Z_B^2}{2\hat{E}_p} e^{-\hat{E}_p t} \operatorname{Tr}\left[\Gamma\left(-i\not{p} + m\right)\right]. \tag{3.12}$$

In this formulation $\hat{E}_p$ is the energy of the ground state of the particle with respect to the momentum p. The computation for mesons is very similar and the result is

$$C_2^{\text{meson}}(t;\vec{p},\Gamma) = \frac{G^2}{2E_p}\left(e^{-E_p t} + e^{-E_p(T-t)}\right), \tag{3.13}$$

where G is a mesonic matrix element similar to eq. 3.9.
The masses and energies can be extracted by taking ratios of the correlation function at

different Euclidean times. For the Baryons this ratio is

$$m^{\mathrm{b}}_{\mathrm{eff}}(t) = \log\left(\frac{C^{\mathrm{b}}_2(p,t)}{C^{\mathrm{b}}_2(p,t+1)}\right). \tag{3.14}$$

The correlation functions for pseudo-scalar and vector mesons are symmetric, so it can be folded around $t = T/2$ to increase statistics. The exponential expression of the two-point correlation function can be reformulated to a hyperbolic cosine. The ratio to extract their mass is

$$m^{\mathrm{m}}_{\mathrm{eff}}(t) = \operatorname{acosh}\left(\frac{C^{\mathrm{m}}_2(p,t-1) + C^{\mathrm{m}}_2(p,t+1)}{2C^{\mathrm{m}}_2(p,t)}\right). \tag{3.15}$$

3.2 Three-point functions

The computation of three-point correlation function is generally much more involved than that of two-point functions. In fig 3.2 the Feynman graph of a general baryonic three-point function is shown.

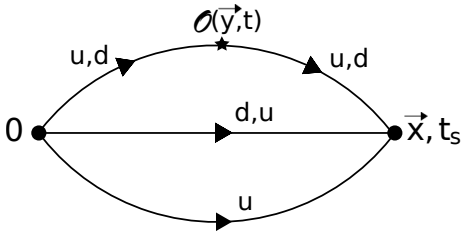

Figure 3.2: nucleon three-point function.

The difficulty in computing three-point functions in lattice QCD is the insertion of the Operator $\mathcal{O}$ at time slice t. One would like to sum over all spatial indices on this time slice for statistical reasons because the summation over all points on a time slice increases statistics by a factor proportional to the spatial volume. This is technically very difficult because an all-to-all propagator would be needed which connects all lattice points on time slice t to all points on time slice t_s. This can be solved generally in two different ways, the fixed operator method [34] or the fixed sink method [80]. These two methods are shown in figure 3.3.
The method in the left panel is the fixed operator method. A usual quark propagator

(red) from time slice 0 to time slice t is multiplied by the operator of interest at the fixed time slice t. The momentum transfer is inserted via a Fourier transformation. This object is used as a source for a new inversion from time slice t to t_s which produces a so called extended propagator (blue). It can be contracted with two propagators from 0 to t_s to build the three-point function. The advantage of this method is that the final and initial states are not fixed. This allows the computation of any baryon form factor or even the nucleon to delta transition. The drawback of this method is the fixed operator. One can only investigate one operator with one momentum transfer. For other operators or other momenta new inversions are needed.

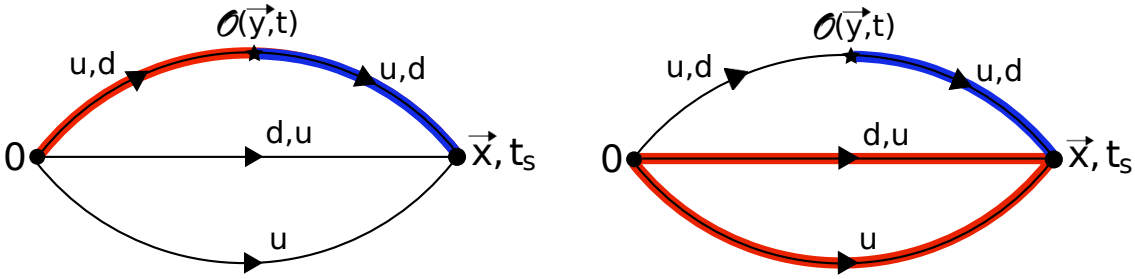

Figure 3.3: Two different ways of the computation of baryonic three-point functions. The left picture shows the fixed operator method and the right one the fixed sink method.

The second method is shown in the right panel of fig 3.3. Here the final and initial states are fixed, e.g. a nucleon. Two quark propagators (red) are contracted at time slice t_s and used as a source for a extended propagator (blue) from time slice t_s to t. The advantage of this method is that the operator and the momentum transfer can be chosen freely without a new inversion. We are generally interested in a various kind of different operators at different momentum transfers between two nucleon states, so this is our method of choice. It will be explained in the next two sections in detail.

3.2.1 The quark level

The general form of the nucleon three-point function is

$$\left\langle \Gamma_{\gamma'\gamma} J_\gamma(x) \mathcal{O}^\mu(y) \overline{J_{\gamma'}(0)} \right\rangle , \tag{3.16}$$

with operators of the form

$$\mathcal{O}^{\mu}(y) = \Psi^{f}_{\delta}(y) O^{\mu}_{\delta\epsilon} \overline{\Psi}^{f}_{\epsilon}(y) \qquad \text{with} \quad \Psi = u \vee d. \tag{3.17}$$

Although our basic formulation of the action has only two degenerate flavors one can build up two different three-point functions. This is due to the fact that the quarks have different charges. The electro-magnetic current couples to an u-quark in one case and to a d-quark in the other case.

d-quark contribution

The computation of the three-point function of the d-quark contribution starts in the same way as for the two-point function. The interpolating field of a nucleon and the operator of eq. 3.17 are inserted in eq. 3.16 where Ψ is replaced by a d-quark field. This leads to

$$\begin{aligned} & \left\langle \Gamma_{\gamma'\gamma} J_{\gamma}(x = (t_s, \vec{x})) \mathcal{O}^{\mu}(y = (t, \vec{y})) \overline{J_{\gamma'}(0)} \right\rangle = \qquad (3.18) \\ = \quad & -\epsilon^{abc}\epsilon^{a'b'c'} \Gamma_{\gamma'\gamma} \left\{ d^{b}_{\beta}(x) [C\gamma_5]_{\beta\alpha} u^{a}_{\alpha}(x) \right\} u^{c}_{\gamma}(x) \cdot d^{f}_{\delta}(y) O^{\mu}_{\delta\epsilon} d^{f}_{\epsilon}(y) \cdot \overline{u^{c'}_{\gamma'}(0)} \left\{ d^{b}_{\beta}(x) [C\gamma_5]_{\beta\alpha} u^{a}_{\alpha} \right\}. \end{aligned}$$

After the Wick contraction this becomes

$$\begin{aligned} & -\epsilon^{abc}\epsilon^{a'b'c'} \left\{ \mathrm{Tr}^{D} \left[S^{d,bf}(x,y) \mathcal{O}(y) S^{d,fb'}(y,0) C\gamma_5 S^{u,ac'}(x,0) \Gamma S^{u,a'c}(x,0) C\gamma_5 \right] - \right. \\ & \left. - \mathrm{Tr}^{D} \left[S^{d,bf}(x,y) \mathcal{O}(y) S^{d,fb'}(y,0) C\gamma_5 S^{u,aa'}(x,0) C\gamma_5 \right] \mathrm{Tr}^{D} \left[\Gamma S^{u,cc'}(x,0) \right] \right\}. \end{aligned} \tag{3.19}$$

u-quark contribution

The computation of the u-quark contribution is straight forward. With the change of the d-quarks into u-quarks in the operator one gets

$$\begin{aligned} & -\epsilon^{abc}\epsilon^{a'b'c'} \left\{ \mathrm{Tr}^{D} \left[\Gamma S^{u,cf}(x,y) \mathcal{O}(y) S^{u,fa'}(y,0) C\gamma_5 S^{d,bb'}(x,0) C\gamma_5 S^{u,ac'}(x,0) \right] + \right. \\ & \qquad + \mathrm{Tr}^{D} \left[S^{u,af}(x,y) \mathcal{O}(y) S^{u,fc'}(y,0) \Gamma S^{u,ca'}(x,0) C\gamma_5 S^{d,bb'}(x,0) C\gamma_5 \right] - \\ & \qquad - \mathrm{Tr}^{D} \left[\Gamma S^{u,cf}(x,y) \mathcal{O}(y) S^{u,fc'}(y,0) \right] \mathrm{Tr}^{D} \left[C\gamma_5 S^{d,bb'}(x,0) C\gamma_5 S^{u,aa'}(x,0) \right] - \\ & \left. \qquad - \mathrm{Tr}^{D} \left[S^{u,af}(x,y) \mathcal{O}(y) S^{u,fa'}(y,0) C\gamma_5 S^{d,bb'}(x,0) C\gamma_5 \right] \mathrm{Tr}^{D} \left[\Gamma S^{u,cc'}(x,0) \right] \right\}. \end{aligned} \tag{3.20}$$

The momentum can be inserted via a Fourier transformation like for the two-point function. This has to be done twice, one time for the initial or final state and then for the momentum transfer at the operator insertion point

$$C_3^d(p,q,t,t_s) = \sum_{\vec{x}} e^{-i\vec{p}\vec{x}} \sum_{\vec{y}} e^{-i\vec{q}\vec{y}} \left\langle \Gamma_{\gamma'\gamma} J_\gamma(\vec{x},t_s) \mathcal{O}_d^\mu(\vec{y},t) \overline{J_{\gamma'}(0)} \right\rangle, \tag{3.21}$$

$$C_3^u(p,q,t,t_s) = \sum_{\vec{x}} e^{-i\vec{p}\vec{x}} \sum_{\vec{y}} e^{-i\vec{q}\vec{y}} \left\langle \Gamma_{\gamma'\gamma} J_\gamma(\vec{x},t_s) \mathcal{O}_u^\mu(\vec{y},t) \overline{J_{\gamma'}(0)} \right\rangle. \tag{3.22}$$

We insert a momentum $\vec{p}$ at the final state and the momentum transfer $\vec{q}$ at the operator insertion point which leads automatically to the momentum at the initial state $\vec{p}'$ via $q = p - p'$.

proton, neutron, isovector and isoscalar form factors

The computed form factor depends on the linear combination of both contributions. The explicit form of the proton is

$$C_3^p = \frac{2}{3} C_3^u - \frac{1}{3} C_3^d, \tag{3.23}$$

and for the neutron

$$C_3^n = -\frac{1}{3} C_3^u + \frac{2}{3} C_3^d. \tag{3.24}$$

Two other combinations can be build, the iso-scalar (i.s.) and the iso-vector (i.v.) nucleon form factors

$$C_3^{i.s.} = C_3^p + C_3^n = \frac{1}{3}\left(C_3^u + C_3^d\right), \tag{3.25}$$

$$C_3^{i.v.} = C_3^p - C_3^n = C_3^u - C_3^d. \tag{3.26}$$

In equations 3.20 and 3.18 the disconnected parts are omitted. They are usually hard to compute because the trace $\sum_{\vec{y}} \mathrm{Tr}\left[S(y,y)\mathcal{O}\right]$ of an operator in a single point has to be calculated. An all-to-all propagator would be needed to get reasonable statistics because of the local sum over each lattice point. Several techniques are known to calculate these contributions. At Mainz, Vera Gülpers is currently working on an implementation with the so called hopping parameter expansion [52]. This will be included in the measure code for baryons in future to investigate e.g. the strangeness in the nucleon or disconnected contributions to the form factors.

In the present computation the disconnected diagrams are not needed because we focus in the iso-vector form factor of the nucleon where these contributions vanish. This can be seen directly in eq. 3.26. For degenerate quarks the disconnected contributions are identical for both three-point functions and cancel out because of the relative minus sign.

3.2.2 Extended source method

The explicit computation of the three-point function is done via the extended source method. The extended propagators are built from two quark propagators which are contracted at time slice t_s where the final momentum is induced via a Fourier transformation. This object has open spinor and color indices and is used as a source for a new inversion to create the extended propagator from time slice t to t_s

$$\Sigma_d(\vec{y},0;t_s,\vec{p}') = \sum_{\vec{x}} e^{i\vec{x}\vec{p}'} \otimes$$

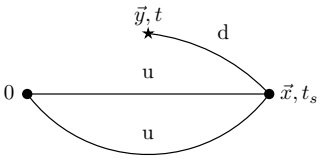

,

$$\Sigma_u(\vec{y},0;t_s,\vec{p}') = \sum_{\vec{x}} e^{i\vec{x}\vec{p}'} \otimes$$

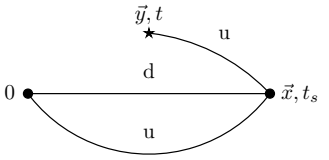

.

The two diagrams come from the two equations 3.20 and 3.18. The starting point is the general expression

$$C_3^{(u,d)}(p,q,t,t_s) = \sum_{\vec{x}} e^{-i\vec{p}\vec{x}} \sum_{\vec{y}} e^{-i\vec{q}\vec{y}} \mathcal{M}_{\beta\beta'}^{(u,d)bb'}(x,0) S_{\beta\delta}^{bf}(x,y) \mathcal{O}_{\delta\delta'}(y) S_{\delta'\beta'}^{fb'}(y,0) \tag{3.27}$$

with e.g. the extended d-source

$$\begin{aligned} \mathcal{M}_{\beta\beta'}^{(d)bb'}(x,0) &= \epsilon^{abc}\epsilon^{a'b'c'} \Gamma_{\gamma'\gamma} \left(C\gamma_5\right)_{\alpha\beta} \left(C\gamma_5\right)_{\beta'\alpha'} \cdot \\ &\quad \cdot \left\{ S_{\alpha'\gamma}^{a'c}(x,0) S_{\alpha\gamma'}^{ac'}(x,0) - S_{\gamma\gamma'}^{cc'}(x,0) S_{\alpha\alpha'}^{aa'}(x,0) \right\}. \end{aligned} \tag{3.28}$$

With this definition the extended propagator can be defined as

$$\Sigma^{(u,d)fb'}_{\delta'\beta'}(\vec{y},0;t_s,\vec{p}) = \sum_{\vec{x}} e^{i\vec{x}\vec{p}} S^{fb}_{\delta'\beta''}(x,y)\gamma^5_{\beta''\beta}\mathcal{M}^{*(u,d)bb'}_{\beta\beta'}(x,0). \tag{3.29}$$

This object propagates from the sink to the source which can be corrected by exploiting the γ_5-hermiticity ($\gamma_5 S(x,y)\gamma_5 = S(y,x)$) of the propagator which leads to

$$\gamma^5_{\delta\delta''}\Sigma^{(u,d)fb'}_{\delta''\beta}(\vec{y},0;t_s,\vec{p}) = \left[\sum_{\vec{x}} e^{i\vec{x}\vec{p}} S^{fb}_{\delta\beta'}(x,y)\mathcal{M}^{*(u,d)bb'}_{\beta\beta'}(x,0)\right]^*. \tag{3.30}$$

Including the extended propagator into eq. 3.27 gives

$$C_3^{(u,d)}(p,q,t,t_s) = \sum_{\vec{y}} e^{-i\vec{q}\vec{y}}\gamma^5_{\delta\delta''}\Sigma^{(u,d)fb}_{\delta''\beta}(\vec{y},0;t_s,\vec{p})\mathcal{O}_{\delta\delta'}(y)S^{fb}_{\delta'\beta}(y,0) \tag{3.31}$$

where the extended propagator can be calculated by solving equation 3.30. The inclusion of the later introduced smearing procedures for the extended quark propagator is explained in detail in appendix C.

electromagnetic and axial operators on the lattice

In general, we are interested in all kinds of nucleon form factors which can be built of different operators. One type of operators which can be easily programmed and are fast to compute are local operators. These operators life on a single lattice site and are in general defined as

$$O^{\text{loc.}}_{\Gamma}(x) = \overline{\Psi}(y)\Gamma\Psi(x), \tag{3.32}$$

where Γ can be one of the sixteen Dirac matrices. The operator $\Gamma = \gamma_\mu$ is related to the vector current, the operators $\Gamma = \gamma_5\gamma_\mu$ to the axial vector current and $\Gamma = \gamma_\mu\gamma_\nu$ to the tensor current. The disadvantage of these operators is that their corresponding multiplicative renormalization factors are not equal to one and have to be calculated separately. In the case of Wilson fermions this was done by the ALPHA collaboration non-perturbatively and their results are summarized in chapter 6 and have been used for the axial current.
To avoid the computation of renormalisation factors, conserved currents can be constructed in some cases. For example, the electro-magnetic current is conserved for Wilson fermions when the u- and d-quarks have the same mass. This current can be computed

via the Noether theorem which leads to

$$\begin{aligned}\mathcal{O}_{\mu}^{\mathrm{V,cons}}(x) &= \frac{1}{4}\Big\{\overline{\Psi}(x)(\gamma_\mu - 1)U_\mu(x)\gamma_\mu\Psi(x+\hat{\mu}) + \overline{\Psi}(x+\hat{\mu})(\gamma_\mu+1)U_\mu^\dagger(x)\gamma_\mu\Psi(x) + \\ &\quad + (x \to x-\hat{\mu})\Big\}\,. \end{aligned} \tag{3.33}$$

In a simulation the part $(x \to x - \hat{\mu})$ can be represented by an additional factor of two because of the sum over the spatial indices in eq. 3.27. The disadvantage of this operator is that it is more expensive than its local counterpart because of more floating point operations and eventually necessarily communications. For Wilson fermions it is not possible to construct a conserved axial current because of the explicit breaking of the chiral symmetry. Symmetry breaking terms arise which are divergent with $1/a$. In contrast, it is possible to construct a conserved axial current for actions which obey the Ginsparg-Wilson relation. However, their construction and computation is much more complicated than e.g. the local operators or the conserved vector current for Wilson fermions defined in eq. 3.33.
In our measurement code we compute all sixteen local operators and the four conserved electro-magnetic operators. This gives us access to the electro-magnetic and axial form factors and it enables us to compute the vector renormalisation constant Z_V. We have also access to the tensor currents but they will not be discussed here.

3.2.3 The hadronic level

The calculation of the three-point function at the hadronic level is straight forward and similar to the computation of the two-point function. The three-point function is defined as follows:

$$C_3^{\mathrm{b}}(t, t_s; \vec{p}, \vec{q}; \Gamma, \mathcal{O}^\mu) = \sum_{\vec{x};\vec{y}} e^{-i\vec{p}\vec{x}} e^{i\vec{q}\vec{y}} \Gamma_{\beta\alpha} \left\langle 0 \left| \chi_\alpha(x) \mathcal{O}^\mu(y) \overline{\chi_\beta}(0) \right| 0 \right\rangle . \tag{3.34}$$

With the completeness relation and the translation operator this becomes

$$\begin{aligned} &C_3^{\mathrm{b}}(t, t_s; \vec{p}, \vec{q}; \Gamma, \mathcal{O}^\mu) = \\ &\quad \sum_{\vec{x};\vec{y}} \sum_{k,s;k',s'} e^{-i\vec{p}\vec{x}} e^{-i\vec{q}\vec{y}} \frac{1}{4k_0 k_0'} \Gamma_{\beta\alpha} \cdot \\ &\quad \cdot \left\langle 0 \left| \chi_\alpha(0) e^{-ikx} \right| k, s \right\rangle \left\langle k, s \left| e^{iky} \mathcal{O}^\mu(0) e^{-ik'y} \right| k', s' \right\rangle \left\langle k', s' \left| \overline{\chi_\beta}(0) \right| 0 \right\rangle . \end{aligned} \tag{3.35}$$

Using equation 3.9, summing over the spatial components, and using $q = p - p'$ one gets

$$C_3^{\mathrm{b}}(t, t_s; \vec{p}, \vec{q}; \Gamma, \mathcal{O}^\mu) = \tag{3.36}$$
$$\sum_{p_0 p_0'} e^{-ip_0(t_s-t)} e^{-ip_0' t} Z_B^f Z_B^{*i} \frac{1}{4 p_0 p_0'} \sum_{s,s'} \Gamma_{\beta\alpha} u_\alpha(p,s) \left\langle p, s \left| \mathcal{O}^\mu(0) \right| p', s' \right\rangle \overline{u_\beta}(p', s').$$

The explicit form of the matrix element $\langle p, s \,|\mathcal{O}^\mu(0)|\, p', s'\rangle$ depends on the operator $\mathcal{O}^\mu(0)$. For the electro-magnetic current it becomes

$$\begin{aligned} \left\langle p, s \left| V^\mu(0) \right| p', s' \right\rangle &= \sqrt{\frac{M^2}{p_0 p_0'}} \overline{u}(p,s) \left\{ \gamma^\mu F_1(q^2) + \frac{i\sigma^{\mu\nu} q_\nu}{2M} F_2(q^2) \right\} u(p', s') = \\ &= \sqrt{\frac{M^2}{p_0 p_0'}} \overline{u}_\gamma(p,s) V^\mu_{\gamma\gamma'} u_{\gamma'}(p', s'), \end{aligned} \tag{3.37}$$

and for the axial current

$$\begin{aligned} \left\langle p, s \left| A^\mu(0) \right| p', s' \right\rangle &= \sqrt{\frac{M^2}{p_0 p_0'}} \overline{u}(p,s) \left\{ \gamma^\mu \gamma_5 G_A(q^2) + \frac{\gamma_5 q^\mu}{2M} G_P(q^2) \right\} u(p', s') = \\ &= \sqrt{\frac{M^2}{p_0 p_0'}} \overline{u}_\gamma(p,s) A^\mu_{\gamma\gamma'} u_{\gamma'}(p', s'). \end{aligned} \tag{3.38}$$

With the explicit form of the operators the spin sums can be calculated. An additional Wick rotation leads to

$$\sum_{E_p, E_{p'}} e^{E_p(t_s-t)} e^{E_{p'} t} Z_B^f Z_B^{*i} \sqrt{\frac{M^2}{E_p E_{p'}}} \frac{1}{4 E_p E_{p'}} \Gamma_{\beta\alpha} \left(-i\not{p} + M\right)_{\alpha\gamma} \mathcal{O}^\mu_{\gamma\gamma'} \left(-i\not{p}' + M\right)_{\gamma'\beta}, \tag{3.39}$$

where $\mathcal{O}^\mu_{\gamma\gamma'}$ can be $V^\mu_{\gamma\gamma'}$ or $A^\mu_{\gamma\gamma'}$. Assuming that the ground state dominates the correlation function at Euclidean times $t \gg 0$ and $t \ll t_s$ one gets

$$\begin{aligned} &C_3^{\text{baryon, ground state}}(t, t_s; \vec{p}, \vec{q}; \Gamma, \mathcal{O}^\mu) = \\ &= e^{\hat{E}(t_s-t)} e^{\hat{E}' t} Z_B^f Z_B^{*i} \sqrt{\frac{M^2}{\hat{E}\hat{E}'}} \frac{1}{\hat{E}\hat{E}'} \Gamma_{\beta\alpha} \left(-i\not{p} + M\right)_{\alpha\gamma} \mathcal{O}^\mu_{\gamma\gamma'} \left(-i\not{p}' + M\right)_{\gamma'\beta}. \end{aligned} \tag{3.40}$$

The extraction of the form factors $F_1(q^2)$, $F_2(q^2)$, $G_A(q^2)$ and $G_P(q^2)$ is usually done by taking ratios of the three-point function and two-point functions to cancel the exponential, kinematical and Z factors. The exact way of performing these ratios is described in

detail in chapter 5.

3.3 Symmetries

Using the symmetry properties of the action can help to improve statistics for baryons without computing new quark propagators. The basic idea is that the polarization matrix Γ does not project all relevant contributions of the baryon into the correlation function. The baryonic correlation function should be invariant under symmetry transformation with a redefinition of the polarization matrix and maybe a change of time direction. These symmetries are only fulfilled in the gauge limit with an infinite number of configurations. For a finite number of configurations it follows that statistics can be improved with this method.
The symmetry properties of the quark propagators for Wilson fermions [53] are collected in table 3.1:

parity $\mathcal{P}$	$S_F(x,y,[U])$	$\rightarrow$	$\gamma_0 S_F(x^P,y^P,[U^P])\gamma_0$
time reversal $\mathcal{T}$	$S_F(x,y,[U])$	$\rightarrow$	$\gamma_0\gamma_5 S_F(x^T,y^T,[U^T])\gamma_5\gamma_0$
charge conjugation $\mathcal{C}$	$S_F(x,y,[U])$	$\rightarrow$	$\gamma_0\gamma_2 S_F^T(x,y,[U^C])\gamma_2\gamma_0$
γ_5-hermiticity $\mathcal{H}$	$S_F(x,y,[U])$	$\rightarrow$	$\gamma_5 S_F^\dagger(x,y,[U])\gamma_5$
combined $\mathcal{CPH}$	$S_F(x,y,[U])$	$\rightarrow$	$C\gamma_0 S_F^\dagger(x^P,y^P,[U^C])\gamma_0 C^{-1}$

Table 3.1: Symmetries of the Wilson-action.

For link variables and quark fields they are summarized in table 3.2:

	$\mathcal{P}$	$\mathcal{C}$	$\mathcal{T}$
$U_0(\vec{x},t)$	$U_0(-\vec{x},t)$	$U_0^*(\vec{x},t)$	$U_{-0}(\vec{x},-t)$
$U_i(\vec{x},t)$	$U_{-i}(-\vec{x},t)$	$U_i^*(\vec{x},t)$	$U_i(\vec{x},-t)$
$\Psi(\vec{x},t)$	$\gamma_0\Psi(-\vec{x},t)$	$C\overline{\Psi}^T(\vec{x},t)$	$\gamma_0\gamma_5\Psi(\vec{x},-t)$
$\overline{\Psi}(\vec{x},t)$	$\overline{\Psi}(-\vec{x},t)\gamma_0$	$-\Psi^T(\vec{x},t)C^{-1}$	$\overline{\Psi}(\vec{x},-t)\gamma_5\gamma_0$

Table 3.2: Symmetry behavior of the link-variables and the spinors.

The properties shown in table 3.2 can be used to calculate the symmetry properties of the two-point correlation function of the nucleon. The starting point is eq. 3.1 which becomes under time transformation

$$\begin{aligned} & \left\langle \Gamma_{\gamma'\gamma} J_\gamma(t) \overline{J_{\gamma'}(0)} \right\rangle \xrightarrow{\mathcal{T}} \left\langle \Gamma_{\gamma'\gamma} J_\gamma(-t) \overline{J_{\gamma'}(0)} \right\rangle = \\ = \quad & -\epsilon^{abc}\epsilon^{a'b'c'} \Gamma_{\gamma'\gamma} \left\{ (\gamma_0\gamma_5 u^a)^T_\alpha(-t) \left[C\gamma_5\right]_{\alpha\beta} (\gamma_0\gamma_5 d^b)_\beta(-t) \right\} (\gamma_0\gamma_5 u^c)_\gamma(-t) \cdot \\ & (\overline{u^{c'}}\gamma_5\gamma_0)_{\gamma'}(0) \left\{ (\overline{d^{b'}}\gamma_5\gamma_0)_{\beta'}(0) \left[C\gamma_5\right]_{\beta'\alpha'} (\overline{u^{a'}}\gamma_5\gamma_0)^T_{\alpha'}(0) \right\}, \end{aligned} \tag{3.41}$$

With the properties of the Dirac matrices one can see that

$$\gamma_5\gamma_0 C\gamma_5\gamma_0\gamma_5 = C\gamma_5 \tag{3.42}$$

holds. A redefinition of the polarization matrix Γ

$$\Gamma \to \Gamma' = \gamma_5\gamma_0\Gamma\gamma_0\gamma_5 \tag{3.43}$$

leads to the result of eq. 3.5 where the particle propagates now backwards in time and due to anti-periodic boundary conditions in time this means: $-t = T - t$. So the baryon propagates backward in Euclidean time.
Under charge conjugation eq. 3.2 becomes

$$\begin{aligned} & \left\langle \Gamma_{\gamma'\gamma} J_\gamma(t) \overline{J_{\gamma'}(0)} \right\rangle \xrightarrow{\mathcal{C}} \left\langle \Gamma_{\gamma'\gamma} J^{\mathcal{J}}_\gamma(x) \overline{J^{\mathcal{J}}_{\gamma'}(0)} \right\rangle = \\ = \quad & -\epsilon^{abc}\epsilon^{a'b'c'} \Gamma_{\gamma'\gamma} \left\{ \left((C\overline{u}^T)^a_\alpha\right) T(x) \left[C\gamma_5\right]_{\alpha\beta} (C\overline{d}^T)^b_\beta(x) \right\} (C\overline{u}^T)^c_\gamma(x) \cdot \\ & (u^T(0)C^{-1})^{c'}_{\gamma'} \left\{ (-d^T(0)C^{-1})^{b'}_{\beta'} \left[C\gamma_5\right]_{\beta'\alpha'} \left((u^T(0)C^{-1})^{a'}_{\alpha'} \right)^T \right\}, \end{aligned} \tag{3.44}$$

and combined with

$$C^T C\gamma_5 C = C\gamma_5, \tag{3.45}$$

$$C^{-1} C\gamma_5 (C^{-1})^T = C\gamma_5, \tag{3.46}$$

eq. 3.2 follows with the redefinition of the polarization matrix

$$\Gamma \to \Gamma'' = C^{-1}\Gamma C. \tag{3.47}$$

The transformation under parity does not give any extra information because of the spa-

tial Fourier transformation. This means that this symmetry is full filled on each configuration. However, instead of treating charge conjugation and time reversal independently both can be combined. The calculation is straightforward and with the redefinition of the polarization matrix

$$\Gamma \to \Gamma''' = \gamma_5\gamma_0 C^{-1}\Gamma C\gamma_0\gamma_5 \tag{3.48}$$

eq. 3.2 follows again. For an unpolarized nucleon with the polarization matrix $\Gamma = \frac{1}{2}(1+\gamma_0)$ only the time reversal can help to improve statistics. This is because the polarization matrix does not change under the transformations of eq. 3.47 and 3.48. Nevertheless statistics should be doubled without extra quark propagator computation. This is used e.g. for the scale determination runs on the N-lattices (see appendix A). All four cases can be used if the nucleon is polarized in a spatial direction. The explicit form of the polarization matrices is

$$\Gamma = \frac{1}{2}(1+\gamma_0)\frac{1}{2}(1-i\gamma_3\gamma 5), \tag{3.49}$$

$$\Gamma^{\mathcal{T}} = \gamma_5\gamma_0\Gamma\gamma_0\gamma_5 = \frac{1}{2}(1-\gamma_0)\frac{1}{2}(1+i\gamma_3\gamma 5), \tag{3.50}$$

$$\Gamma^{\mathcal{C}} = C^{-1}\Gamma C = \frac{1}{2}(1-\gamma_0)\frac{1}{2}(1-i\gamma_3\gamma 5), \tag{3.51}$$

$$\Gamma^{\mathcal{TC}} = \gamma_5\gamma_0 C^{-1}\Gamma C\gamma_0\gamma_5 = \frac{1}{2}(1+\gamma_0)\frac{1}{2}(1+i\gamma_3\gamma 5). \tag{3.52}$$

It can be seen that time reversal interchanges the parity states which end up in the backward propagating nucleon and that the charge conjugation changes the polarization. Here it becomes clear that these transformations cannot help for an unpolarized nucleon. The conclusion may be that one always wants to use a polarized baryon because of the additional factor of possible symmetries. In fact this is not true. The unpolarized correlation functions yield exactly the same information as the combination of the two oppositely polarized ones. Adding the polarization matrices of eq. 3.49 and 3.50 would cancel out the polarization part and only the parity projection part $\frac{1}{2}(1+\gamma_0)$ would survive. Even in computation time is no difference, because the number of floating point operations is equal in both cases. This can be seen by using the explicit form of the Dirac matrices of appendix B.

3.3.1 Numerical tests

Several numerical test were done to investigate the effectiveness of the procedure. The symmetries were tested on a unit gauge configuration on a $24^3 \cdot 48$ lattice first where a polarized nucleon was used.

	am_N (unit gauge)			
t	Γ	$\gamma_5\gamma_0\Gamma\gamma_0\gamma_5$	$C^{-1}\Gamma C$	$\gamma_5\gamma_0 C^{-1}\Gamma C\gamma_0\gamma_5$
1	3.82865176	3.82865176	3.82865176	3.82865176
2	3.23518176	3.23518176	3.23518176	3.23518176
3	2.63575776	2.63575776	2.63575776	2.63575776
4	2.21107029	2.21107029	2.21107029	2.21107029
5	1.95938463	1.95938463	1.95938463	1.95938463
6	1.80765799	1.80765799	1.80765799	1.80765799
7	1.70786280	1.70786280	1.70786280	1.70786280
8	1.63672123	1.63672123	1.63672123	1.63672123
9	1.58284196	1.58284196	1.58284196	1.58284196
10	1.54012743	1.54012743	1.54012743	1.54012743

Table 3.3: Effective mass of the nucleon on a $24^3 \cdot 48$ unit gauge configuration with a point source for different symmetry implementations where Γ is defined in eq. 3.49.

	am_N (on one configuration)			
t	Γ	$\gamma_5\gamma_0\Gamma\gamma_0\gamma_5$	$C^{-1}\Gamma C$	$\gamma_5\gamma_0 C^{-1}\Gamma C\gamma_0\gamma_5$
1	3.23746333	3.20810556	3.25763674	3.21511013
2	2.61698026	2.45148180	2.65746371	2.43873602
3	1.94582826	1.74421940	1.95342781	1.71493731
4	1.06588204	1.27094530	1.12741865	1.24675807
5	0.72067928	1.18773517	0.77644065	1.00231185
6	0.68346265	0.68587261	0.68695906	0.57373558
7	0.63018481	0.80701582	0.66378687	0.72709548
8	0.67529857	0.71870522	0.75565792	0.63389439
9	0.69291943	0.58812292	0.72190671	0.47572330
10	0.81512947	0.58197591	0.67760304	0.50670618

Table 3.4: Effective mass of the nucleon on a single $24^3 \cdot 48$ configuration with $\beta = 5.3$ and $\kappa = 0.13590$, created with a point source for different symmetry implementations.

In table 3.3 the effective masses of the different polarized nucleons are shown. For the time reversal in the rows 3 and 5 the time is changed by hand from $T - t$ to t for a better readability. The symmetries are perfectly preserved up to all digits shown. This is because of the unit gauge configuration. On 'real' configurations these symmetries hold only in the gauge average, so one would expect very similar but different values for the four cases. So the second test was done on a single $24^3 \cdot 48$ configuration with $\beta = 5.3$ and $\kappa = 0.13590$.
The effective masses of this test are shown in table 3.4. One can see that one gets similar but not identical values for the four polarization matrices. Averaging over the four polarizations and a lot of configurations should improve statistics significantly compared to a single polarization.

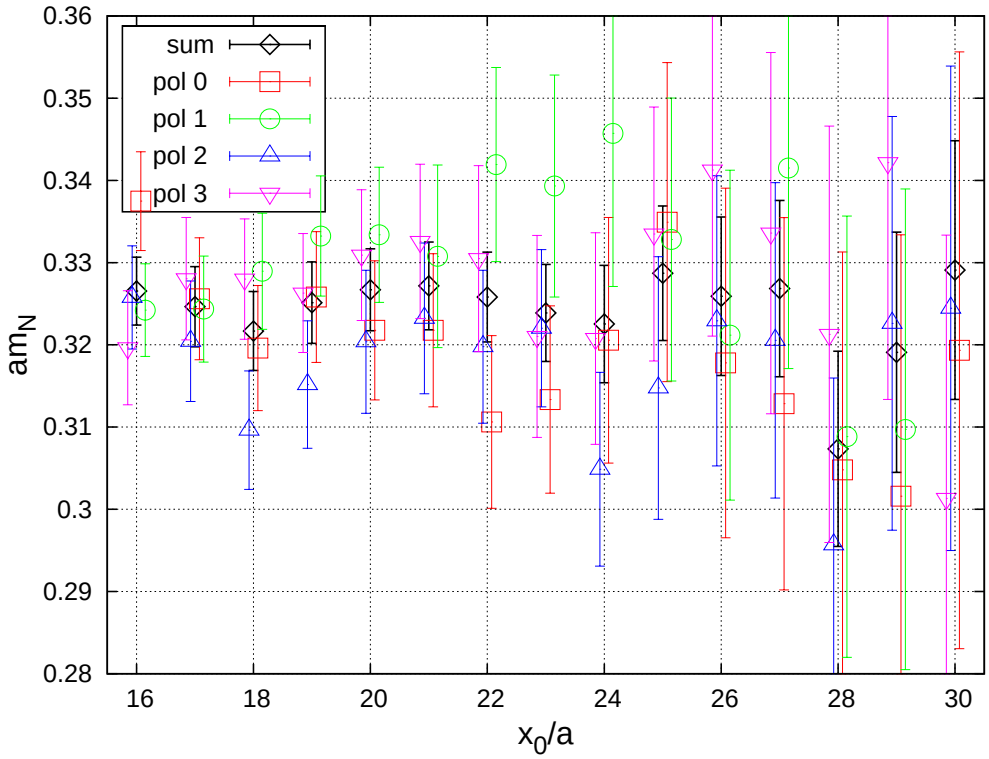

Figure 3.4: Effective mass of a nucleon created with a smeared source and a smeared sink in the plateau region. It is measured on 150 N5 configurations where for each polarization four source positions are used. The polarization matrices are as follows: pol0 = eq. 3.49, pol1 = eq. 3.50, pol2 = eq. 3.51, pol3 = eq. 3.52.

The effectiveness of the method in terms of statistics is shown in fig. 3.4. This is the effective mass of the nucleon in the plateau region measured on 150 N5 configurations where for each polarization matrix four source positions were used. It is compared to the average over the four polarizations. All four polarizations give a compatible mass plateau while the sum over all four fluctuates much less and the error is smaller.
In fig. 3.5 the noise-to-signal ratio is shown for the same data set. One can see a statistical gain of roughly a factor of 2. One would need four times more configurations to get the same improvement in statistics assuming $\sigma \approx 1/\sqrt{N}$ holds! This is a dramatic improvement for the baryonic two-point functions. The alternative procedure is computing new quark propagators for different source positions, which was already used here to improve statistics further. But even the computation of a quark propagator is much more expensive (roughly one order of magnitude) than computing a baryonic two-point function with a new polarization matrix.

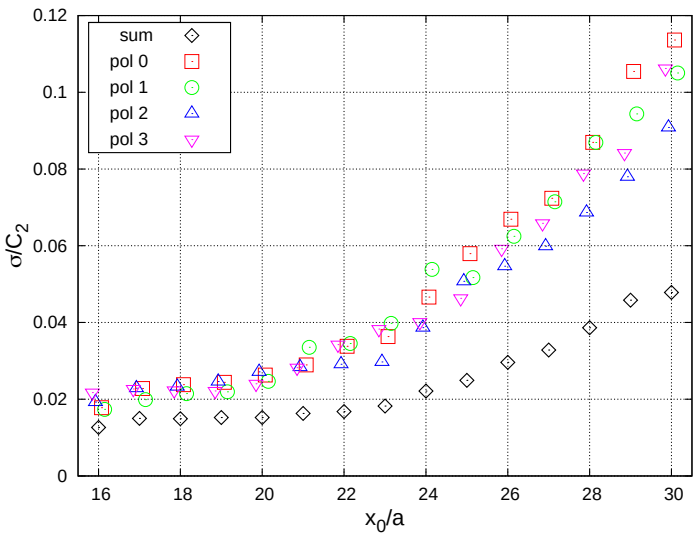

Figure 3.5: The noise-to-signal ratio σ/C_2 of the same data set shown in fig. 3.4.

For baryonic three-point functions the efficiency is not as good as for two-point functions because the polarization matrix Γ is used to construct the extended sources (see eq. 3.28). This means that any change of the polarization matrix needs a new inversion of the extended propagator. We use four to eight different source positions for our form factor computations on each configuration. In order to reduce autocorrelations for the different source positions different polarization matrices are used. To have a rough estimate of

the autocorrelations the pre-binning procedure was used (see appendix D) with different pre-bin sizes. No autocorrelation effects have been seen for the observables which are presented here.

3.4 Systematic effects II

The computation of correlation function suffers from additional systematic effects than those coming from the action itself which were discussed in chapter 2.5 already. These effects, their influence on the different correlations functions. and possible solutions to avoid or minimize them will be discussed here.

3.4.1 Discretized momenta

It was shown in chapter 2 that the momentum is discretized in lattice QCD on the inverse lattice

$$\Lambda_E^* = \left\{ p \in \mathbb{R}^4 \,\middle|\, p^0 = \frac{2\pi}{T} n^0, p^j = \frac{2\pi}{L} n^j, j = 1, 2, 3, \right\} \tag{3.53}$$

with its cut-off

$$-\frac{\pi}{a} < p_\mu \leq \frac{\pi}{a}. \tag{3.54}$$

This is usually no problem for two-point functions because one is interested in the effective masses or other quantities of the ground state at zero momentum transfer. In contrast, for form factors this is an unwanted constraint because they are momentum dependent. This means that it is not possible to simulate at very small momentum transfers and one is limited in the total range of momenta because of cutoff effects at large momenta.

A possible solution for the first problem is to use twisted boundary conditions [9, 28]. The trick is that the quark field Ψ picks up a phase θ when it crosses the boundary of the lattice in spatial k-direction $\Psi(x + L_k) = e^{i\Theta_k}\Psi(x)$. This results in a modified spatial momentum

$$p = n\frac{2\pi}{L} + \frac{\Theta}{L}. \tag{3.55}$$

The advantage of this technique is that the phase factor can be chosen freely which allows arbitrary and hence small momenta.
In simulations these boundary conditions are only applied in the computation of quark propagators and not in the creation of the configurations because of numerical costs. This approach is called 'partially twisted boundary condition' (pTBC). It leads to finite size effects because of the breaking of rotational and flavor symmetry. These effects were investigated in chiral perturbation theory (χPT) for mesons in [93] where it was shown that the finite size effects are exponentially suppressed in processes without final state interactions.
For the nucleon electro-magnetic form factors similar investigations via Heavy Baryon Chiral Perturbation Theory (HBχPT) have been done in [61, 60]. It was shown that the volume effects induced by the pTBC are not negligible for small twist angles. These effects have been studied numerically as well in [49] for the nucleon electro-magnetic form factors at a pion mass of $m_\pi = 630$ MeV and a volume with $m_\pi L = 5.7$. Their conclusion was that some data points with pTBCs scatter more than without and that further investigations are needed.
In our measurement code pTBC are included and are very successfully used for pion form factor computations [20]. For baryons first tests were done for the energies of the nucleon. The results are shown in table 3.5.

Four. mom.	t.a. (q,q,q)	aE_N	aE_N dis.rel.(con.)	aE_N dis.rel.(lat.)
(0,0,0)	(ut,ut,ut)	0.504(9)	0.505	0.505
	(tw,ut,ut)	0.527(10)	0.523	0.520
	(tw,tw,ut)	0.581(12)	0.575	0.562
	(tw,tw,tw)	0.644(15)	0.652	0.621
(-1,0,0)	(ut,ut,ut)	0.545(9)	0.542	0.536
	(tw,ut,ut)	0.508(8)	0.508	0.508
	(tw,tw,ut)	0.513(7)	0.511	0.510
	(tw,tw,tw)	0.553(8)	0.549	0.542

Table 3.5: Nucleon energies for the twist angles ($\theta_1 = 4.4, \theta_{2,3} = 0$) applied to the three quark propagators of the nucleon. The first column shows the Fourier momentum, the second one which quark propagators are twisted while each ut or tw represents an untwisted (ut) or a twisted (tw) quark propagator. The third one shows the data extracted from fits to the correlation function and the last two show data computed via the continuum and the lattice versions of the dispersion relation.

The data for the energies are extracted via fits to the effective mass. In column 4 data are shown computed via the continuum dispersion relation $E^2 = \vec{p}^2 + m^2$. The mass was taken from the fit to the correlation function at zero momentum ($m = 0.504$). The lattice version of the dispersion relation for fermions is

$$\sinh^2(E) = \sin^2(\vec{p}) + \sinh^2(m). \tag{3.56}$$

All results are compatible to the predictions of the continuum case within the statistical errors. In the future further test are necessary to investigate systematically all effects of the twisted boundary conditions. These tests will be in principle very expensive because each twist angle needs a new inversion to create a corresponding quark propagator.

3.4.2 Noise-to-signal ratio

The noise-to-signal ratio behaves differently for different particles. In fig. 3.6 the effective masses of a pion, a ρ-meson and a nucleon measured on 150 N5 configurations are shown. For small time slices contributions from excited states can be observed which will be discussed in the next section. For larger Euclidean times the noise-to-signal ratio for the nucleon and the ρ-meson starts to increase while it remains constant for the pion.

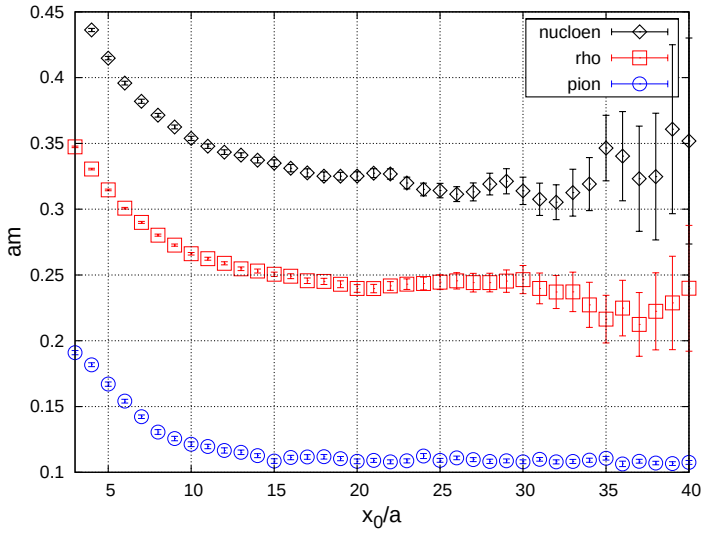

Figure 3.6: Effective mass of a pion, a ρ-meson and a nucleon created with a smeared source and a local sink. They were computed on 150 N5 configurations with four source positions and for the nucleon additionally with four polarizations.

In fig. 3.7 the noise-to-signal ratio of the same data set of fig. 3.6 is shown. A clear exponential growth of the noise-to-signal ratio for the ρ-meson and the nucleon can be observed.
This behavior is explained in [67] and will be summarized here briefly. The formula for the variance of the pion on N configurations can be written as

$$N\sigma_\pi^2 \approx \left\langle \mathrm{Tr}\left[S\gamma_5 S^\dagger \gamma_5\right]^2 \right\rangle - \langle C_2^\pi \rangle^2 \tag{3.57}$$

with C_2^π of eq. 3.13 and S is a usual quark propagator. Both terms fall off approximately exponentially like $e^{-2m_\pi t}$ because the left one can be interpreted as two pions propagating from time 0 to t. For the signal-to-noise ratio follows

$$\frac{\langle C_2^\pi \rangle}{\sigma_\pi} \approx \sqrt{N} \cdot \text{const.} \tag{3.58}$$

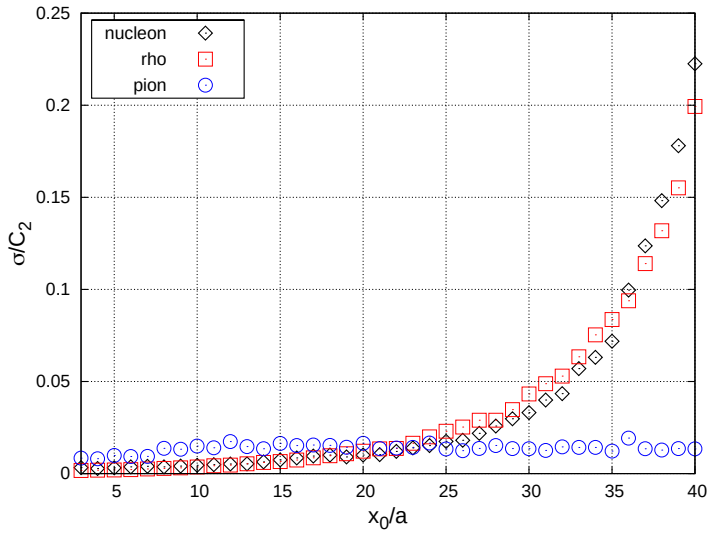

Figure 3.7: The noise-to-signal ratio for several hadrons on the same data set shown in fig. 3.6.

The situation is more involved for baryons. The correlation function of a nucleon consist of three quarks propagating from time 0 to time t and can be written generically as

$$C_2^b = \langle S(t,0)S(t,0)S(t,0)\rangle \,. \tag{3.59}$$

The variance of a baryon computed on N configurations is

$$N\sigma_b^2 \approx \left\langle S^3 S^{\dagger 3} \right\rangle - \left\langle C_2^b \right\rangle^2. \tag{3.60}$$

The second term falls off exponentially with the baryon mass but the first term does not. The lightest particles in QCD which can be build up of three quark propagators and three anti-quark propagators are not a baryon and a anti-baryon but three pions which fall off like $e^{-3m_\pi t}$. For the signal-to-noise ratio for a baryon follows

$$\frac{\left\langle C_2^b \right\rangle}{\sigma_b} \approx \sqrt{N} \cdot e^{-(m_b - \frac{3}{2}m_\pi)t}, \tag{3.61}$$

which leads to the exponential error growth observed in fig. 3.7. The computation for the vector meson is similar with the result

$$\frac{\left\langle C_2^v \right\rangle}{\sigma_v} \approx \sqrt{N} \cdot e^{-(m_v - m_\pi)t}. \tag{3.62}$$

This problem becomes more important for small quark masses because the difference between the baryon or vector masses and the pion masses becomes smaller. This leads to a faster exponential error growth. For baryons an additional problem emerges due to the anti-parity state propagating backward in Euclidean time which overlaps of course in the middle of the lattice with the baryon state one is interested in. One possible solution may be the fixing of the baryon number on each configuration similar to fixing the parity for glue-ball computations in [31]. But this must be investigated in the future.

3.4.3 Excited state contributions

Excited state contributions for a pion, a ρ-meson, and a nucleon can be observed in fig. 3.6. Before the effective mass builds a plateau, higher states can contribute for small Euclidean times. In the calculation at the hadronic level of a correlation function it is assumed that only the ground state contributes $\sum_{E_p} e^{-E_p t} \approx e^{-\hat{E}_p t}$. This is only true for large Euclidean times but for smaller times an exponential decay of the higher states can be observed. Especially for vector mesons and baryons the situation can become difficult because of the increasing noise-to-signal ratio discussed in the previous section. In the worst case higher states did not disappear when the error becomes very large on the

effective mass. This would made the extraction of particle masses impossible.
To calculate the excited state contribution eq. 3.11 is a good starting point. Looking at the energy dependent part including the first excited state one gets

$$\begin{aligned} C_2^{\text{excited}} &\propto \sum_{E_p} \frac{(\not{p}+M)}{E_p} e^{-E_p t} = \\ &= \frac{(\not{p}_0+M)}{E_0} e^{-E_0 t} + \frac{(\not{p}_1+M)}{E_1} e^{-E_1 t} + \mathcal{O}\left(e^{-E_2 t}\right) \approx \\ &\approx \frac{(\not{p}_0+M)}{E_0} e^{-E_0 t} \cdot \left\{1 + \frac{E_0\,(\not{p}_1+M)}{E_1\,(\not{p}_0+M)} e^{-\Delta t}\right\} \\ \Rightarrow C_2^{\text{excited}} &= C_2^{\text{ground state}} \cdot \left\{1 + A \cdot e^{-\Delta t}\right\}, \end{aligned} \tag{3.63}$$

where $\not{p}_0$ and $\not{p}_1$ mean momenta with energies E_0 and E_1 respectively, and A is introduced as an abbreviation for later calculations. The contributions of the first excited state fall off exponentially with the Euclidean time proportional to the energy gap $\Delta = E_1 - E_0$. We assume that the energy gap of the ground state and the first excited state for stable particles is proportional to twice the pion mass [29]. This means that excited state contributions become more and more important with decreasing pion masses. It is crucial to control them in the chiral regime. In addition, we tried fits where the gap was a free fit parameter. However, the statistical errors of these fits were so large that no additional informations about this state could be made.
The basic idea to reduce excited state contributions is the so called Gaussian- or Jacobi-smearing of the source and the sink. As mentioned before a quark propagator can be constructed by solving a linear equation of eq. 2.87. Instead of using the point source $\eta^{ab}_{\alpha\beta}(x,y) = \delta_{ab}\delta^{\alpha\beta}\delta(x-y)$ a smearing procedure can be applied to get an Gaussian shape source. This is motivated by the exponential form of the charge distribution of the proton. With this method the overlap of the ground state with the vacuum should be increased which leads to a suppression of the excited states. A detailed description of the method can be found in appendix C.
The contribution of the first excited state to the three-point function can be calculated in the same way as for the two-point function. Starting point is eq. 3.40 which leads to

$$
\begin{aligned}
C_3^{\text{excited}} &\propto \sum_{E_p} \frac{(\not{p} + M)}{E_p^{\frac{3}{2}}} e^{-E_p(t_s - t)} \sum_{E_p'} \frac{(\not{p}' + M)}{E_p'^{\frac{3}{2}}} e^{-E_p' t} = \\
&= \left\{ \frac{(\not{p}_0 + M)}{E_0^{\frac{3}{2}}} e^{-E_0(t_s - t)} + \frac{(\not{p}_1 + M)}{E_1^{\frac{3}{2}}} e^{-E_1(t_s - t)} + \mathcal{O}\left(e^{-E_2(t_s - t)}\right) \right\} \cdot \\
&\quad \cdot \left\{ \frac{(\not{p}_0' + M)}{E_0'^{\frac{3}{2}}} e^{-E_0' t} + \frac{(\not{p}_1' + M)}{E_1'^{\frac{3}{2}}} e^{-E_1' t} + \mathcal{O}\left(e^{-E_2' t}\right) \right\} \approx \\
&\approx \frac{(\not{p}_0 + M)}{E_0^{\frac{3}{2}}} e^{-E_0(t_s - t)} \frac{(\not{p}_0' + M)}{E_0'^{\frac{3}{2}}} e^{-E_0' t} \cdot \\
&\quad \cdot \left\{ 1 + \frac{E_0^{\frac{2}{3}} (\not{p}_1 + M)}{E_1^{\frac{3}{2}} (\not{p}_0' + M)} e^{-\Delta(t_s - t)} \right\} \left\{ 1 + \frac{E_0'^{\frac{3}{2}} (\not{p}_1 + M)}{E_1'^{\frac{2}{3}} (\not{p}_0' + M)} e^{-\Delta' t} \right\} \\
\Rightarrow C_3^{\text{excited}} &= C_3^{\text{ground state}} \cdot \left\{ 1 + B \cdot e^{-\Delta(t_s - t)} \right\} \cdot \left\{ 1 + B' \cdot e^{-\Delta' t} \right\}. \qquad (3.64)
\end{aligned}
$$

In contrast to excited state contributions for two-point functions these effects are much more important for three-point functions. They have to decay from the source and in addition from the sink side of the correlation function. A consequence is that the source-sink separation t_s must be large enough to ensure that the three-point function can reach the ground state. Having a look at the effective mass, t_s must be at least twice as large as the first time slice where a plateau is observed (see chapter 5). But in most cases the noise-to-signal ratio will be bad for these large Euclidean times because of the exponential error growth. As for the two-point functions smearing can be applied for three-point functions as well but it will be shown later that this is not enough to ensure a large enough suppression of the excited states.

A closer look at excited state contributions to effective masses will be done in chapter 4 and for the three-point functions in chapter 5.

Chapter 4

Scale setting

The continuum limit has to be taken by performing simulations at different values of the lattice spacing which enables us to do an extrapolation to $a = 0$. This is only possible if the relation of the lattice spacing in physical units to the bare coupling strength β of the gauge action and the bare quark masses parameter κ_{sea} is known very precisely [105]. This can be done non-perturbatively by computing a dimensionful quantity O which is known from experiment as well at a fixed combination of β and κ_{sea}. The scale can then be set by taking the ratio of this observable computed on the lattice and the corresponding physical one

$$a[\text{MeV}^{-1}] = \frac{aO_{\text{lat}}|_{\beta,\kappa_{\text{sea}}}}{O_{\text{phys}}[\text{MeV}]}. \tag{4.1}$$

Various kinds of observables have been used to set the scale, e.g. the static potential $V(r)$ with respect to the Sommer parameter r_0 [100], the nucleon mass m_N [5] or the kaon decay constant f_K [79]. Here we want to use the omega mass m_Ω because it has some advantages. The omega baryon is a stable particle in QCD and not a resonance like e.g. the vector kaon K^*. Its light quark mass dependence should be mild compared with e.g. the nucleon, because its constituent quarks are only strange quarks. However, the lattice formulation used has no dynamical strange quark. In order to extract the omega mass the strange quark mass has to be determined quenched.
The strategy to extract the scale is as follows. On each ensemble the masses for pseudoscalar mesons, vector mesons, the nucleon and the omega baryon are computed. Three types of ratios are formed: A method which was used at CERN first and which is de-

scribed in [29] where the Kaon is divided by it vector partner, $R_1 = \left(\frac{m_K}{m_{K^*}}\right)^2$. This can be chirally improved by leading order Chiral Perturbation theory, $R_2 = \frac{(m_K^2 - \frac{1}{2}m_\pi^2)}{m_{K^*}^2}$. The advantage is that the leading order sea quark contributions of the Kaon are eliminated. In the third ratio the excited Kaon is replaced by the Ω-baryon, $R_3 = \frac{(m_K^2 - \frac{1}{2}m_\pi^2)}{m_\Omega^2}$ to minimize sea quark effects further. These ratios are determined for several values of κ_v and a fixed β. It is demanded that these ratios are equal to their physical values which leads to a value for κ_s. These values are then plotted and fitted against $(m_\pi/m_N)^2$ for each ensemble with the same value of the coupling strength β and extrapolated to the physical point. Other ratios than $(m_\pi/m_N)^2$ have been used to extrapolate to the physical point. In the parallel data analysis by Georg von Hippel $(m_\pi r_0)^2$ has been used. The ratio $(m_\pi/m_\Omega)^2$ is not a good choice because the omega mass will be used to set the scale. The extrapolated value is then taken as the bare strange quark mass parameter κ_s to extract the omega mass. This omega mass is then plotted against $(m_\pi/m_N)^2$ and extrapolated to its physical value. The scale can finally be set by eq. 4.1:

$$a[\text{fm}] = \hbar c \frac{a m_\Omega^{\text{lat}}\big|_{\text{extr.}}}{m_\Omega^{\text{phys}}[\text{MeV}]}. \tag{4.2}$$

4.1 Particle masses

Particle masses can be extracted from the two-point functions with a fit to the correlation functions of eq. 3.13 for mesons or eq. 3.12 for baryons. As an alternative a fit to the effective masses of eq. 3.14 and 3.15 can be done. All examples for masses which are shown in this chapter are from the N5-ensemble with the bare parameters $\beta = 5.5$ and $\kappa_{\text{sea}} = 0.13660$.

The pseudo-scalar meson masses are the easiest to extract, because excited state contributions are relatively small and their noise-to-signal ratio remains constant with increasing Euclidean time. The pseudo-scalar masses measured on the N5-ensemble are shown in fig. 4.1. The pion is represented by the red and black points where the red points are from a correlation function computed with a local source and the black points with a Gaussian smeared source. The other three effective masses represent Kaons where one quark mass is equal to the sea quark mass of $\kappa_{\text{sea}} = 0.13660$ and the other one of the one shown in the legend of the plot. All Kaons are only computed with a smeared source in order to save

CPU time. Each new κ-value would need an individual inversion of the Dirac-operator for the point source and the smeared source. The point-source correlation function for the pion has the advantage of cross checking the smearing procedure. No deviations can be observed in the plateau region except a smaller error for the smeared data.

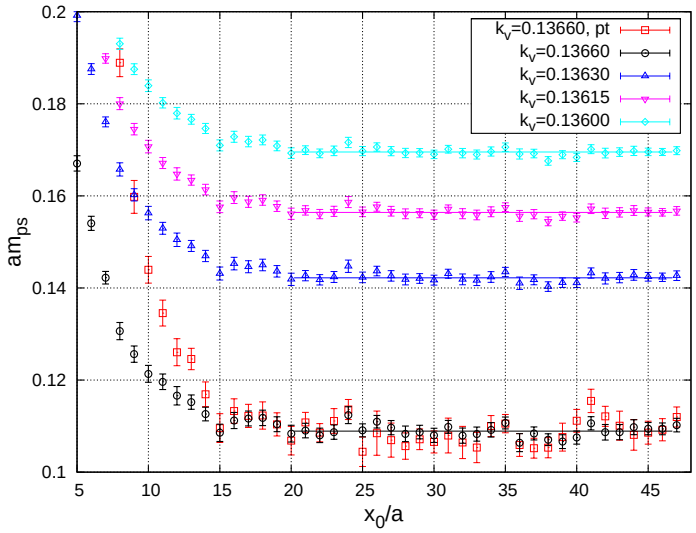

Figure 4.1: Effective mass plot of the pseudo-scalar mesons for different values of the valence quark mass on the N5-ensemble. The lines denote our best fit results to the two-point correlation function. Error bands of the fits are not shown, because they are too small.

The fits are done as follows. We do an uncorrelated fit and in addition a correlated fit with a frozen covariance matrix [89] to each bootstrap sample (see appendix D) of the correlation function. The fit interval is tuned in a way that the reduced correlated chi square defined as $\frac{\chi^2}{\text{degrees of freedom}}$ is close to 1 with a maximally large fit range. For the pseudo-scalar mesons this is always the interval $[t_{\text{min}}, T/2]$, where T is the maximal number of time slices and t_{min} is tuned. The maximal value $T/2$ can be taken because no exponential error growth is present for pseudo-scalar mesons. The fit results are shown as lines in fig. 4.1 but the errors of these fits are too small to show error bands.
The situation completely changes for vector mesons. Their effective mass plots are shown in fig. 4.2. The lowest mass corresponds to a ρ-meson while the higher masses correspond to the K^*-meson. The coloring is the same as for the pseudo-scalar mesons. One can see excited state contaminations for small Euclidean times and noise-to-signal growth for large Euclidean times. To control the excited state contributions and to allow fits from relatively small time slices a fit to the effective mass of eq. 3.15 is done where excited

states are explicitly taken into account. The fit function becomes

$$f(m_{\text{eff}}, c, \Delta) = m_{\text{eff}} + ce^{-\Delta x_0} \tag{4.3}$$

where m_{eff}, c and Δ are in principle free fit parameters. It turned out that the nonlinear fits with a free Δ are very unstable and lead to extremely large errors. We tried to fix the gap proportional to the vector mass plus a pion state with momentum [29]

$$\Delta^V = \sqrt{M_V^2 + k^2} + \sqrt{m_\pi^2 + k^2}, \quad k = \frac{2\pi}{L} \tag{4.4}$$

but the fits could not be stabilized. However, the choice $\Delta = 2m_\pi$ gives stable results and a good χ^2. This leads to the fits shown in fig. 4.2.

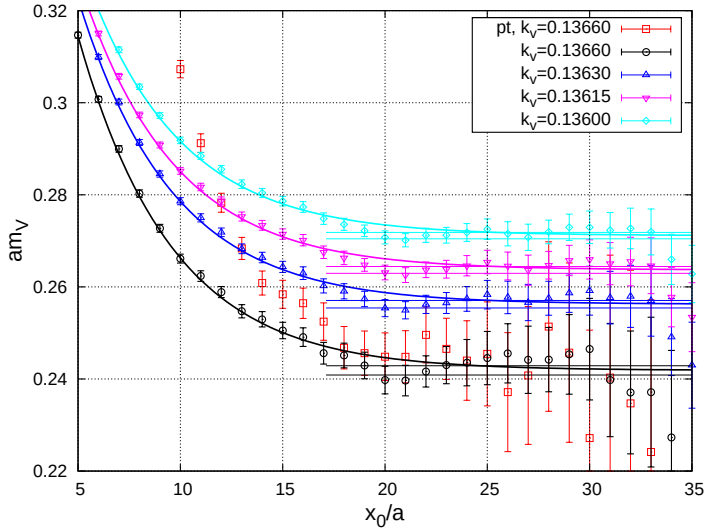

Figure 4.2: Effective mass plot of the vector mesons for different values of the valence quark mass computed on the N5-ensemble. The lines through the points denote our best fit results to the effective mass. The horizontal lines denote the error bands of the effective mass from these fits.

The effective mass of the nucleon is shown fig. 4.3. This plot is a nice example for the effectiveness of the source smearing. The excited states are suppressed and the noise-to-signal ratio is enhanced in comparison to the point source. The fits are done with respect to eq. 4.3 including the first excited state with the fixed gap $\Delta = 2m_\pi$. The same procedure was taken for the Ω-baryon whose effective mass is shown in fig. 4.4.

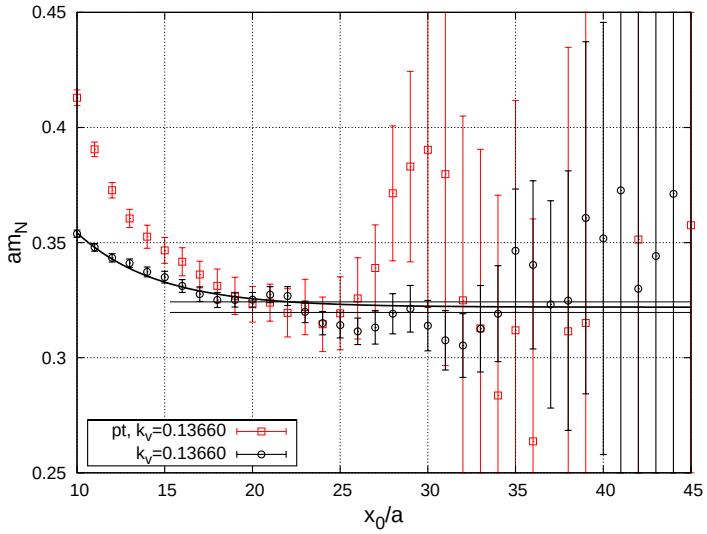

Figure 4.3: Effective mass plot of the nucleon for a point source and a smeared source computed on the N5-ensemble. The lines through the points denote our best fit results to the effective mass. The horizontal lines denote the error bands of the effective mass from these fits.

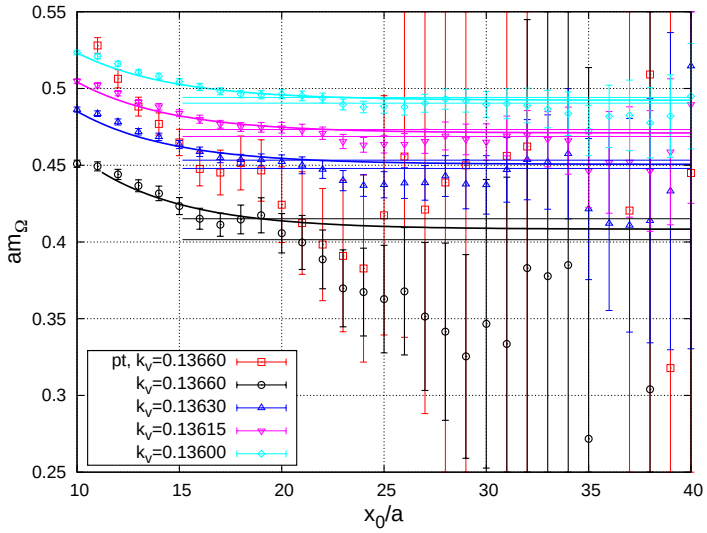

Figure 4.4: Effective mass of the Ω-baryon for different values of the valence quark mass.

Systematic errors for these fit procedures can be determined in different ways. Different fit function could be used, like a plateau fit, a plateau fit with fixed excited state gap and one with a non fixed gap. The results of these different fits can be compared and the deviation is an indication for the size of the systematic error. Another procedure would be to fit only with one fit function but for a couple of intervals of points. As long as the reduced χ^2 is reasonable (say smaller than 1.5) it can be assumed that these fits are good.

The size of the systematic error can be estimated by the maximal deviation of these fits of the mean value. It turned out, that for both methods the systematic error is in the range of the statistical one.

4.2 The strange quark hopping parameter κ_s

With the computation of all relevant particle masses the value for kappa strange κ_s can be determined on each ensemble. We use the three aforementioned scale independent ratios R_1, R_2 and $R3$. The third ratio is plotted against the inverse mass parameter $\frac{1}{\kappa_v}$ in fig. 4.5. Two different methods for the interpolation have been used, a direct interpolation between two neighboring points and a quadratic fit in $\frac{1}{\kappa_v}$ through all points. The values and their errors from both methods are absolutely compatible and it has no effect on the final result which method is further used. In this work the quadratic fit was used.

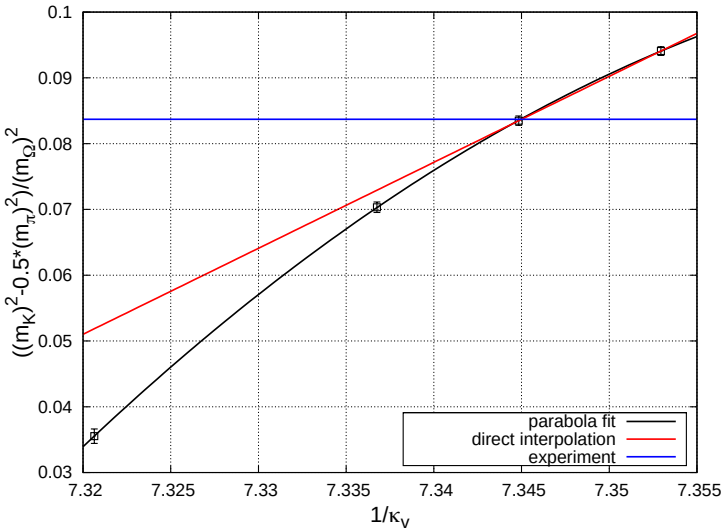

Figure 4.5: The ratio $R_3 = \frac{(m_K^2 - \frac{1}{2}m_\pi^2)}{m_\Omega^2}$ plotted against $\frac{1}{\kappa_v}$. The difference between a quadratic fit and a direct interpolation is negligible.

The blue line represents the physical value of this ratio and the strange quark mass parameter κ_s is extracted from its intercept with the quadratic interpolation.

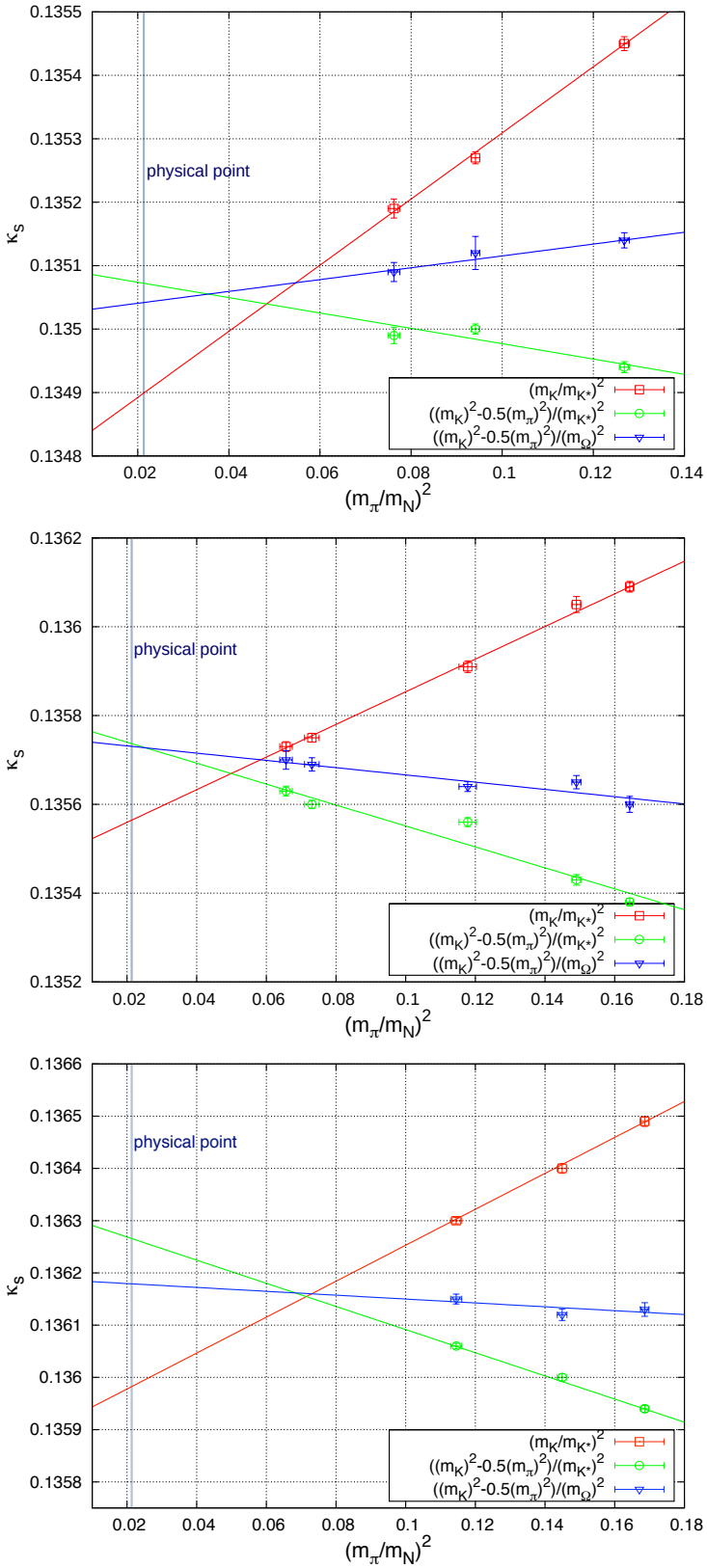

Figure 4.6: Estimates for κ_s for the three methods. The top picture shows data for $\beta = 5.2$, the middle one for $\beta = 5.3$ and the bottom one for $\beta = 5.5$.

One usually has an educated guess about the κ_s-values for the different methods from previous simulations with same β but different κ_{sea}. As shown in the example the advantage is that the interpolation distance is small. The plots for the other methods look very similar to the one of fig. 4.5 and the same procedure was used to extract the values for κ_s.

These intercepts are computed for several β and κ_{sea} for all three methods. The ensembles used are A3, A4 and A5 for $\beta = 5.2$, E3, E4, E5, F6 and F7 for $\beta = 5.2$ and finally N3, N4 and N5 for $\beta = 5.5$. The results can be seen in fig. 4.6. In these plots the values for all three methods are shown in dependence of $(m_\pi/m_N)^2$. One can see that the difference between the three methods become smaller with smaller pion masses, and one would expect that they agree at the physical point up to cut-off effects. The physical point is indicated by the blue-grey vertical line. The three methods have different strong dependence on $(m_\pi/m_N)^2$. The dependence for the chiral method with the omega mass has the smallest dependence and hence the smallest dependence on the light quark masses. Because of this, this will be the method of choice to determine κ_s.

To extrapolate the data to the physical point a linear fit in $(m_\pi/m_N)^2$ to all three methods are done which are represented by the blue, green and red lines. One can see that both chirally improved methods give close values for κ_s to each other (within 1-3 σ) while the original CERN method is relatively far away (more than 5 σ). The values for κ_s which will be used later are summarized in table 4.1.

β	5.2	5.3	5.5
κ_s	0.135041(32)	0.135730(20)	0.136179(34)

Table 4.1: Values for κ_s for the ratio $\frac{(m_K^2 - \frac{1}{2}m_\pi^2)}{m_\Omega^2}$ extrapolated to the physical point.

4.3 Setting the scale via the Ω-mass

Two different values for κ_s are used to extract the omega mass on each ensemble, the chirally extrapolated one shown in table 4.1 and the one determined on each ensemble. The omega mass is plotted in fig. 4.7 against $\frac{1}{\kappa_v}$. A linear fit is used to interpolate between the different κ values. The blue line represents the value for κ_s extracted via the chiral extrapolation and the red line the value extracted directly on this ensemble via $\frac{(m_K^2 - \frac{1}{2}m_\pi^2)}{m_\Omega^2}$. Both values for the omega masses are used to do chiral extrapolations to the physical point. The results are shown in fig. 4.8 where the red curves are for $\beta = 5.2$, the green curves for $\beta = 5.3$ and the blue ones for $\beta = 5.5$. Within these linear fits no difference can be seen in the extrapolated values for the two methods. This means that the result for the chiral extrapolated omega mass depends only weakly on the value of κ_s at the physical point.

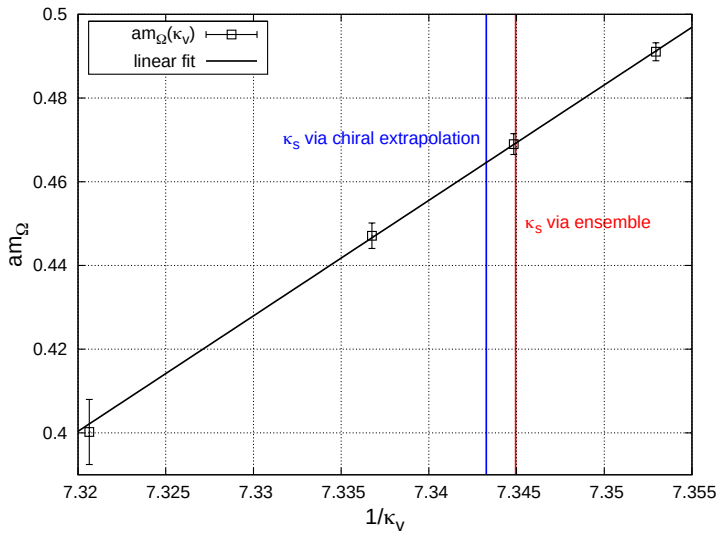

Figure 4.7: Extraction of the omega mass via two different choices of κ_s on the N5-ensemble.

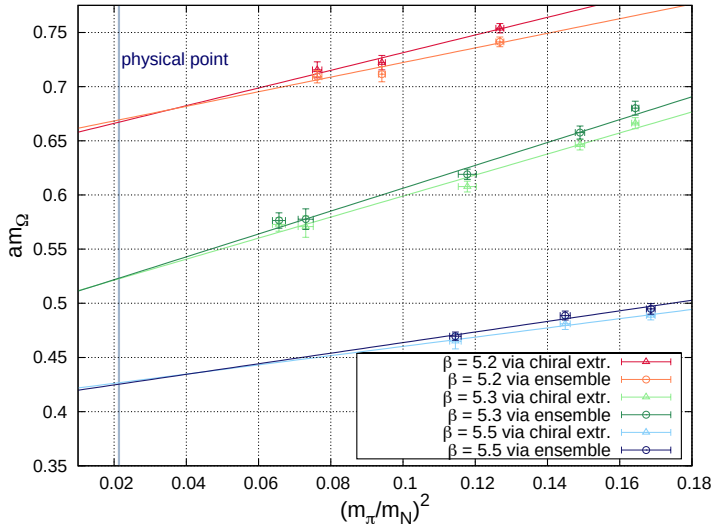

Figure 4.8: Extrapolation of the omega mass to the physical point for all three β-values and both extracted omega masses.

Having a closer look at the green points in fig. 4.8 may lead to the suspicion that discarding the two points for the heaviest pion masses would lead to higher value for the scale, since the extrapolated omega mass would increase. This is true but the value is within one standard deviation from the other value. In addition to a linear chiral extrapolation one could think about a quadratic extrapolation as well. With the data presented here, this would be only possible for the $\beta = 5.3$ data-set, because of the number of points. However, the error increases for this fit, and the value is compatible with the linear fit within statistical errors.

With these chirally extrapolated omega masses the scale can be determined for each β value via eq. 4.2. The final results are summarized in the first row of table 4.2 and compared to two different evaluations. The second row shows the data from a similar analysis from Mainz from Georg von Hippel [101]. We used the same data sets to extract the scale, but with two differences. While in this thesis the nucleon mass was used to get a scale in-depend way of setting the physical point, in the other analysis the Sommer parameter r_0 was used, which was computed in Berlin by Björn Leder [65] on the same ensembles. To make contact between the r_0 data and our data computed in Mainz, the so-called UWerr [106] method was used to compute the errors. Within the errors our results agree very well.

The second completely independent analysis of the scale was done by Marina Marinkovic [79] and her data are shown in the third row of table 4.2. She used two different ways

of extracting the scale. First via the Kaon decay constant f_K and the second via the PCAC-mass relation. It is remarkable that all values are in a very good agreement with each other in spite of the different methods to extract these data.

β	5.2	5.3	5.5
a[fm] (B.K.)	0.079(1)	0.062(1)	0.050(2)
a[fm] (G.v.H.)	0.079(3)	0.063(2)	0.052(3)
a[fm] (M.M.)	0.075(3)	0.065(1)	0.0481(5)

Table 4.2: Values for the scale extracted in three different ways.

As mentioned before all dimensionful quantities have to be renormalized with the lattice spacing. For the $\beta = 5.2$ and $\beta = 5.3$ ensembles the relative error of the determination lies around 1.5% which is good but leaves space for further improvement. Some of the measured quantities will have relative errors much smaller than those on the scale, so their errors would be artificially blown up. The error of the scale for $\beta = 5.5$ is quite large, around 3.0% because of the relatively large chiral extrapolation. In the future this will be further enhanced by additional data points on the ensembles N6 and O7 which have much smaller pion masses. For the other two beta values additional lattices are planned, the G8 and B6 lattices, which will improve the values for the scale as well.

Chapter 5

Form factors

5.1 Extracting matrix elements

The computation of form factors was discussed in detail in chapter 3. Matrix elements of the form $\langle p', s \,|\mathcal{O}^{\mu}|\, p, s' \rangle$ must be extracted via ratios of the three-point function and two-point functions to cancel all unwanted prefactors. The three-point function of the nucleon at the hadronic level was derived in chapter 3.2 and will be recapitulated here:

$$C_3^{\text{baryon, ground state}}(t, t_s; \vec{p}, \vec{q}; \Gamma, \mathcal{O}^{\mu}) = \tag{5.1}$$
$$= e^{\hat{E}(t_s - t)} e^{\hat{E}' t} Z_B^f Z_B^{*i} \sqrt{\frac{M^2}{\hat{E}\hat{E}'}} \frac{1}{\hat{E}\hat{E}'} \Gamma_{\beta\alpha} \left(-i\not{p} + M\right)_{\alpha\gamma} \mathcal{O}^{\mu}_{\gamma\gamma'} \left(-i\not{p}' + M\right)_{\gamma'\beta} .$$

The operators $\mathcal{O}^{\mu}_{\gamma\gamma'}$ are defined in equations 3.37 and 3.38. The aim would be to find a ratio which cancels all prefactors so that only $\mathcal{O}^{\mu}_{\gamma\gamma'}$ survives. It will be shown that this becomes difficult when excited state contributions become large. We investigated two methods to handle these effects: Excited state contributions are explicitly taken into account in our fits (see section 5.1.2) and, we use the so called summation method (section 5.1.3).

5.1.1 Ratio method

Several ratios have been studied in [6] where it turned out that

$$R(\vec{q},t,t_s) = \frac{C_3(\vec{q},t,t_s)}{C_2(\vec{0},t_s)} \sqrt{\frac{C_2(\vec{q},t_s-t)C_2(\vec{0},t)C_2(\vec{0},t_s)}{C_2(\vec{0},t_s-t)C_2(\vec{q},t)C_2(\vec{q},t_s)}} \tag{5.2}$$

is the best ratio to obtain the matrix elements. Inserting eq. 3.12 and eq. 3.40 into this ratio leads to:

$$\begin{aligned}
R(\vec{q},t,t_s) &= \frac{e^{-E_p(t_s-t)}e^{-E_{p'}t} Z'_B Z^*_B \sqrt{\frac{M^2}{E_pE_{p'}}} \frac{1}{4E_pE_{p'}} \operatorname{Tr}\left[\Gamma\left(-i\not{p}'+M\right)\mathcal{O}^\mu\left(-i\not{p}+M\right)\right]}{\frac{Z_B^2}{2E_p}e^{-E_pt_s}\operatorname{Tr}\left[\Gamma\left(-i\not{p}+M\right)\right]} \cdot \\
&\quad \cdot \sqrt{\frac{\frac{Z_B'^2}{2E_{p'}}e^{-E_{p'}(t_s-t)} \cdot \frac{Z_B^2}{2E_p}e^{-E_pt} \cdot \frac{Z_B^2}{2E_p}e^{-E_pt_s}\operatorname{Tr}\left[\Gamma\left(-i\not{p}+M\right)\right]}{\frac{Z_B^2}{2E_p}e^{-E_p(t_s-t)} \cdot \frac{Z_B'^2}{2E_{p'}}e^{-E_{p'}t} \cdot \frac{Z_B'^2}{2E_{p'}}e^{-E_{p'}t_s}\operatorname{Tr}\left[\Gamma\left(-i\not{p}'+M\right)\right]}} = \\
&= \frac{e^{-E_{p'}t}e^{E_pt} Z'_B \sqrt{\frac{M^2}{E_pE_{p'}}} \frac{1}{2E_{p'}} \operatorname{Tr}\left[\Gamma\left(-i\not{p}'+M\right)\mathcal{O}^\mu\left(-i\not{p}+M\right)\right]}{Z_B\operatorname{Tr}\left[\Gamma\left(-i\not{p}'+M\right)\right]} \cdot \\
&\quad \cdot \sqrt{\frac{e^{-E_{p'}(t_s-t)} \cdot e^{-E_pt} \cdot \frac{Z_B^2}{2E_p}e^{-E_pt_s}\operatorname{Tr}\left[\Gamma\left(-i\not{p}+M\right)\right]}{e^{-E_p(t_s-t)} \cdot e^{-E_{p'}t} \cdot \frac{Z_B'^2}{2E_{p'}}e^{-E_{p'}t_s}\operatorname{Tr}\left[\Gamma\left(-i\not{p}'+M\right)\right]}} = \\
&= \frac{e^{-E_{p'}t}e^{E_pt} \sqrt{\frac{M^2}{E_pE_{p'}}} \frac{1}{2E_{p'}} \operatorname{Tr}\left[\Gamma\left(-i\not{p}'+M\right)\mathcal{O}^\mu\left(-i\not{p}+M\right)\right]}{\sqrt{\operatorname{Tr}\left[\Gamma\left(-i\not{p}+M\right)\right]\operatorname{Tr}\left[\Gamma\left(-i\not{p}'+M\right)\right]}} \cdot \sqrt{\frac{E_{p'}e^{2E_{p'}t}}{E_pe^{2E_pt}}} = \\
&= \frac{M}{2E_pE_{p'}} \frac{\operatorname{Tr}\left[\Gamma\left(-i\not{p}'+M\right)\mathcal{O}^\mu\left(-i\not{p}+M\right)\right]}{\sqrt{\operatorname{Tr}\left[\Gamma\left(-i\not{p}+M\right)\right]\operatorname{Tr}\left[\Gamma\left(-i\not{p}'+M\right)\right]}}
\end{aligned} \tag{5.3}$$

In eq. 5.3 all exponentials and Z-factors are cancelled and only kinematical pre-factors have survived. The explicite form of the matrix element depends of course on the operator $\mathcal{O}^\mu$ and in addition on the polarization matrix Γ. We used a nucleon polarized in 3-direction with the polarization matrix $\Gamma = \frac{1}{2}(1-\gamma_0)\frac{1}{2}(1-i\gamma_3\gamma_5)$. This gives us in principle access to all four electro-magnetic and axial form factors $G_E(q^2)$, $G_M(q^2)$, $G_A(q^2)$ and $G_P(q^2)$. An unpolarized nucleon would only give access to $G_E(q^2)$ and $G_A(q^2)$ and the other two form factors are canceled out in the ratio.
The computation of the form factor content of eq. 5.3 is in principle straight forward but

has to be done for each operator and for each polarization matrix individually. A Mathematica script was used to obtain the results. For our choice of the polarization matrix we get

$$\mathrm{Re}\left[R(\vec{q},t,t_s)_{\gamma_0}\right] = \sqrt{\frac{M+E}{2E}} \underbrace{\left\{F_1(q^2) - \frac{\vec{p}'^2}{2M(M+E)}F_2(q^2)\right\}}_{\xrightarrow{n.r.lim} G_E(q^2)}, \tag{5.4}$$

$$\mathrm{Re}\left[R(\vec{q},t,t_s)_{\gamma_i}\right]_{i=1,2} = \epsilon_{ij}p_j\sqrt{\frac{1}{2E(E+M)}} \underbrace{\left\{F_1(q^2)+F_2(q^2)\right\}}_{=G_M(q^2)}, \tag{5.5}$$

$$\mathrm{Im}\left[R(\vec{q},t,t_s)_{\gamma_5\gamma_3}\right] = \sqrt{\frac{M+E}{2E}}\left\{G_A(q^2) - \frac{2p'^2_3}{ME}G_P(q^2)\right\} \xrightarrow{q\to 0} g_A. \tag{5.6}$$

The extraction of the form factors can be done by taking the real or the imaginary part of the ratios for a certain combination of momentum transfer q and the sink time slice t_s. The time dependence of the ratio was only manifest in the exponentials of the three-point function, which were canceled out by taking the ratios. So finally the signal must be a plateau in Euclidean time.

For this choice of the polarization matrix other linear combinations of form factors contribute. The form factors could be extracted from these components as well but they are much more noisy than the one shown in eq. 5.4-5.6 and no additional informations could be gained.

Not all kinematical factors are cancelled but they can be easily computed from the nucleon two-point functions (see chapter 4). The problem is that for higher momenta the plateaux for the energies become very noisy which results in large errors. Indeed we use the mass of the nucleon and compute the energies via the lattice version of the dispersion relation of eq. 3.56. The errors from the energies computed via the dispersion relation are much smaller and are in a good agreement with the direct fit results.

The electric form factor $G_E(q^2)$ is only accessible from eq. 5.4 in the non-relativistic limit of small momentum transfers. This may lead to systematic effects. A comparison of the non-relativistic limit and the exact form of eq. 5.4 shows no differences larger than the statistical error. This means that both form factors $G_E(q^2)$ and $G_M(q^2)$ can be directly extracted from these ratios safely.

The extraction of the axial form factors is a bit more involved because both form factors appear in the same ratio. This is not a real problem because $G_P(q^2)$ is proportional to the

third component of the initial momentum p'_3. As long as this component is zero, $G_A(q^2)$ can be extracted safely. $G_P(q^2)$ can be extracted from the ratios then where p'_3 is non zero by subtracting the previously determined $G_A(q^2)$

$$G_P(q^2) = \frac{M}{2p'^2_3}\left\{G_A(q^2) - \sqrt{\frac{2E}{M+E}}\,\mathrm{Im}\left[R(\vec{q},t,t_s)_{\gamma_5\gamma_3}\right]\right\}. \tag{5.7}$$

The problem with this method is that the axial form factors cannot be extracted for all Fourier momenta with this choice of the polarization matrix. Momentum combinations where all three spatial components of the momentum transfer are non-zero cannot be disentangled. Hence, the statistical error for the axial form factors is larger than the ones for the electro-magnetic ones, because less momenta contribute to the same ratio. This is acceptable for the presented calculations because we focus on the electro-magnetic form factors and the axial charge. To be able to get more precise information about the two axial form factors other polarization matrices must be taken into account. This would be much more expensive because additional extended propagators need to be computed.
The different methods are presented for the unrenormalized axial charge $G_A(0) = g_A$ in this and the following sections. The ratio for the axial charge should be independent of Euclidean time t and the sink position t_s as shown before. In fig. 5.1 ratios for four different sink position for the unrenormalized axial charge on 150 N5 configurations are shown where the quark propagators are created with a Gaussian smeared source and sink.

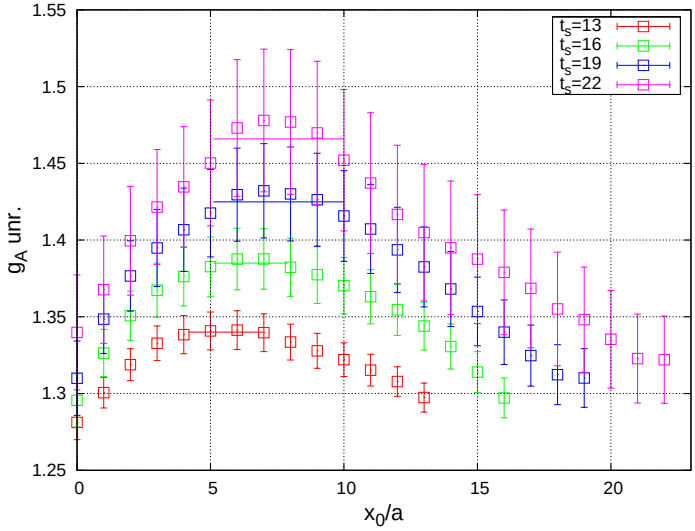

Figure 5.1: Unrenormalized axial charge computed on 150 N5 configurations with a Gaussian smeared source and sink for four different sink positions $t_s = 13, 16, 19, 22$. The lines denote uncorrelated fits to the plateaux.

Excited state contributions can be observed which decay exponentially from the source and the sink side until the ratio reaches a relatively short plateau. The plateaux were fitted by a constant and the fit results are shown as lines in fig. 5.1 and are summarized in table 5.1.

	$t_s = 13$	$t_s = 16$	$t_s = 19$	$t_s = 22$
g_A	1.340(12)	1.385(19)	1.425(29)	1.466(44)
χ^2/d.o.f.	0.011	0.023	0.054	0.078

Table 5.1: Results of the plateau fits on the N5 ensemble.

The reduced χ^2 is in general bad for uncorrelated and correlated fits (see appendix D). However, the uncorrelated fits give reasonable results while correlated fits are totally off of the fitted data points. This was observed for all matrix elements on all ensembles. Hence, only uncorrelated fit results are shown in the following figures.
The shortness of the plateaux would not be a serious problem in general if the plateaux would be equal for the different sink positions. Unfortunately this is not the case and one can see a clear trend to higher values of g_A for higher values of t_s. The conclusion is that the excited state contributions are so large that fake plateaux are built which lead to the increasing values. But how large must the source-sink separation be to get safe and unaffected plateaux?
One hint can be given by the two-point correlation function of the nucleon. In fig. 5.2 a direct comparison of the three-point function with the effective mass of the nucleon is shown. The upper four panels show the normalized value ρ of the axial charge for the four values of t_s where $\rho = \frac{G_A(q^2=0,t)}{G_A(q^2=0,t_s/2)}$ is the axial charge normalized by its value at $t = t_s/2$. The deviations from a perfect plateau which should be 1 can be clearly seen for all four values of t_s.
In the bottom panel the mass of the nucleon is shown. The plateau starts at $t = 15$ where large contributions from excited states can be seen for smaller Euclidean times. For three-point functions the excited state contributions come not only from the source but also from the sink. It follows that the source-sink separation should be at least twice as large as the first time slice of the plateau of the mass plot. In this special case this would mean that the minimal value must be $t_s = 30$. The problem is that the nucleon suffers from the exponential error growth with increasing t_s as can be clearly seen in fig.

5.1.
It follows that the ratio method is insufficient to deal with excited state contributions. Other methods have to be developed to take these contributions into account.

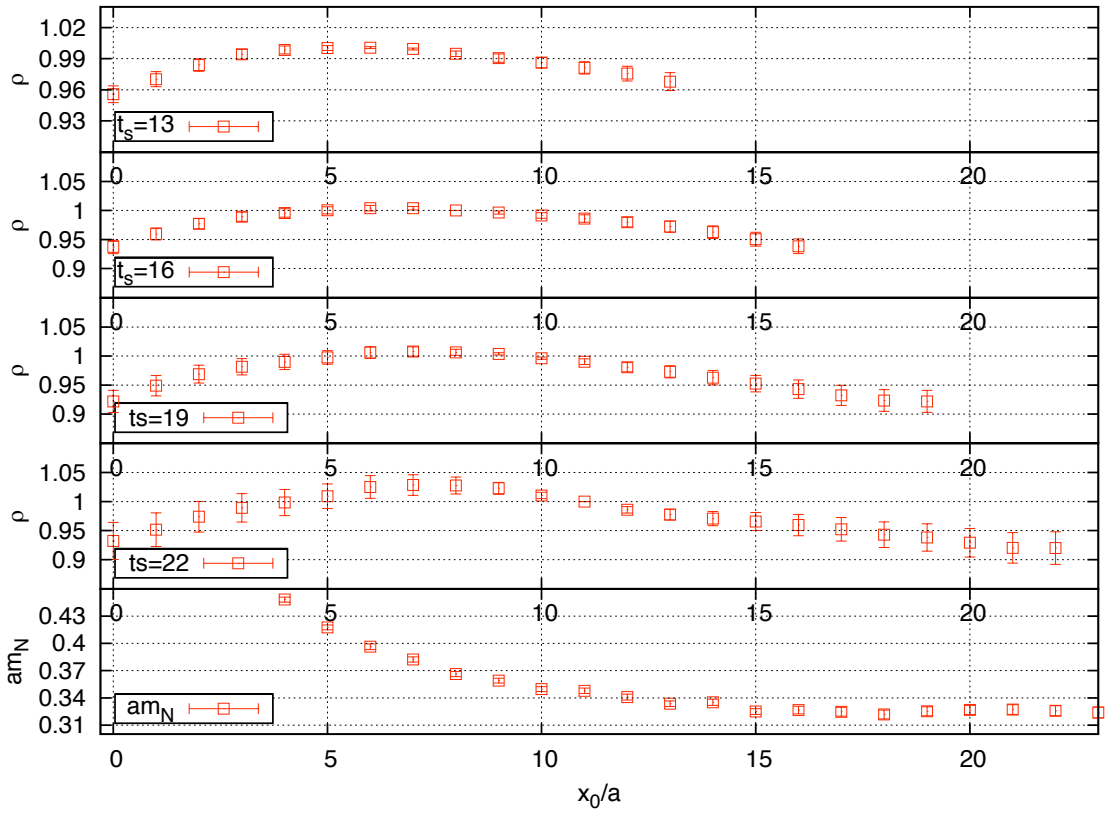

Figure 5.2: The upper four panels show the ratio $\rho = \frac{G_A(q^2=0,t)}{G_A(q^2=0,t_s/2)}$ for the four values of t_s. The bottom panel shows the effective mass of the nucleon.

5.1.2 Including excited state contributions

The excited state contributions were already computed for the two-point and the three-point functions in chapter 3.4.3. This has to be done for the ratio of eq. 5.2 as well. It can directly be seen that the contributions from the first excited state factorizes from the ground state contributions via

$$R^{0+1}(\vec{q},t,t_s) = R^0(\vec{q},t,t_s) \cdot R^1(\vec{q},t,t_s) \tag{5.8}$$

with

$$R^1(\vec{q},t,t_s) = \frac{\left(1+B\cdot e^{-\Delta(t_s-t)}\right)\left(1+B'\cdot e^{-\Delta' t}\right)}{\left(1+A\cdot e^{-\Delta t_s}\right)}\cdot \cdot \sqrt{\frac{\left(1+A'\cdot e^{-\Delta'(t_s-t)}\right)\left(1+A\cdot e^{-\Delta t}\right)\left(1+A\cdot e^{-\Delta t_s}\right)}{\left(1+A\cdot e^{-\Delta(t_s-t)}\right)\left(1+A'\cdot e^{-\Delta' t}\right)\left(1+A'\cdot e^{-\Delta' t_s}\right)}}, \tag{5.9}$$

and $R^0(\vec{q},t,t_s)$ from eq. 5.3. Using the Taylor expansion of the square root and omitting all higher terms this results in

$$\begin{aligned} R^1(\vec{q},t,t_s) &= 1+Be^{-\Delta(t_s-t)}+B'e^{-\Delta' t}+ \\ &\quad +\frac{1}{2}\left\{A'e^{-\Delta'(t_s-t)}+Ae^{-\Delta t}-Ae^{-\Delta(t_s-t)}-A'e^{-\Delta' t}-A'\cdot e^{-\Delta' t_s}-Ae^{-\Delta t_s}\right\}. \end{aligned} \tag{5.10}$$

It can be clearly seen in eq. 5.10 that excited state contributions contaminate the ground state matrix elements from both sides. This corresponds to the observations in fig. 5.2. Equation 5.10 becomes much easier when equal gaps are assumed $\Delta = \Delta'$. This is legitimate for the axial charge, because the initial and final states are equal. For two-point functions it was assumed that the gap between the ground state and the first excited state is proportional to twice the pion mass. This is assumed here as well. Both assumptions lead to the somewhat handier expression for the excited state contributions

$$R^{0+1}(\vec{q},t,t_s) = R^0(\vec{q},t,t_s)\cdot\left(1+\mathcal{O}\left(e^{-\Delta t}\right)+\mathcal{O}\left(e^{-\Delta(t_s-t)}\right)+\mathcal{O}\left(e^{-\Delta t_s}\right)\right), \tag{5.11}$$

with the explicit representation $\Delta = 2m_\pi$. This gap can be included explicitly in the fits to the ratios like for the two-point functions. The fit function can be directly read off of eq. 5.11 and is

$$f(\vec{q},t,t_s) = g_A + c_1 e^{-\Delta t} + c_2 e^{-\Delta(t_s-t)} + c_3 e^{-\Delta t_s}, \tag{5.12}$$

with the four free fit parameters g_A, c_1, c_2 and c_3. To improve the stability and the statistical error of the fits it is assumed that all fit parameters and the energy gap Δ are independent of t_s. This results in a simultaneous fit to all values of t and t_s. In fig. 5.3 the result of the uncorrelated fit on the N5 ensemble is shown and summarized in table 5.1.2.

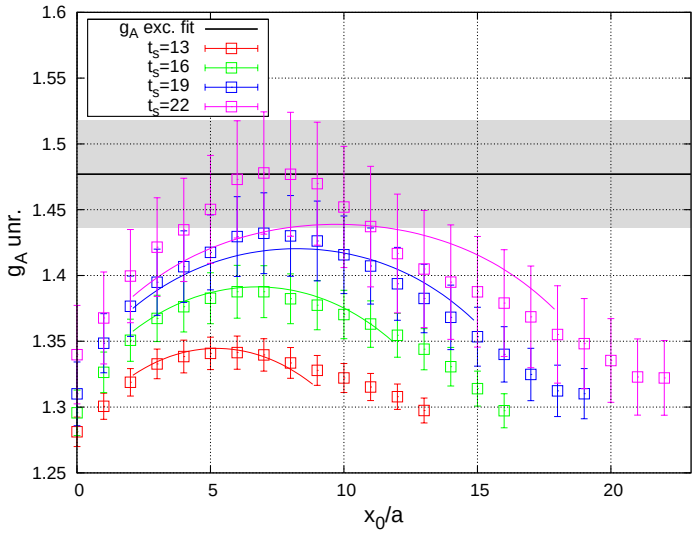

Figure 5.3: The same data set as in fig. 5.1 is shown here. The lines of the fits are results of fits to the function of eq. 5.12 with fixed energy gap $\Delta = 2m_\pi$.

g_A	c_1	c_2	c_3	χ^2/d.o.f.
1.477(41)	-0.131(40)	-0.229(59)	-0.823(402)	0.248

Table 5.2: Results of a fit to eq. 5.12 on the N5 ensemble.

The reduced χ^2 is very small for the uncorrelated fit like for the plateau fits but it is in a good agreement with the data points. Correlated fits have been used here as well. The χ^2 of the correlated fits is reasonable but the fitted curves do not hit the data points (not shown in fig. 5.3). This may be due to the fact that these kinds of fits are highly dominated by the data points with small errors for the smallest sink-source separation. It could be that this is misinterpreted as large correlations. The value of g_A extracted from this fit is shown with its error band in fig. 5.3. One can see that this value is in a very good agreement with the plateau points for the largest t_s.

5.1.3 The summation method

The disadvantage of the method introduced in the last chapter is that many assumptions have to be made. A different ansatz is the so called summation method which was al-

ready used previously [78, 55, 35]. The idea is to sum the ratio in eq. 5.11 over all time slices t up to the sink t_s. Starting point for the computation is eq. 5.10. The sum over the exponentials can be worked out with the representation of the geometric sum

$$\sum_{t=0}^{t_s} e^{-\Delta t} = \frac{e^{-\Delta(t_s+1)} - 1}{e^{-\Delta} - 1}. \tag{5.13}$$

After a straight forward computation and omitting all terms smaller than $t_s e^{-\Delta t_s}$ one finds

$$\sum_{t=0}^{t_s} R^{0+1}(\vec{q}, t, t_s) = R^0(\vec{q}, t, t_s) \cdot t_s + c(\Delta, \Delta') + \mathcal{O}\left(t_s e^{-\Delta t_s}\right) + \mathcal{O}\left(t_s e^{-\Delta' t_s}\right). \tag{5.14}$$

This is obviously an improvement compared to eq. 5.11 because the source-sink separation t_s is much larger than t or $t_s - t$. To get roughly the same level of suppression of excited state contributions with the plateau method, t_s must be twice as large as for the summation method.

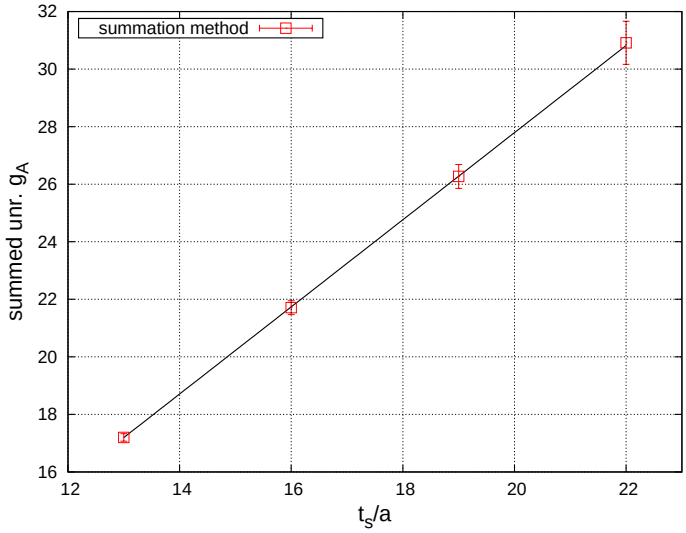

Figure 5.4: The summation method for four different values of t_s. The data are fitted to the function of eq. 5.15.

The matrix element can be extracted from eq. 5.14 by computing it for different values of t_s. A straight line of the form

$$f(g_A, c1) = g_A t_s + C \tag{5.15}$$

can be fitted. The result of such a fit is shown in fig. 5.4 and the fit parameter are summarized in table 5.1.3.

g_A	C	χ^2/d.o.f.
1.514(58)	-2.48(72)	0.0145

Table 5.3: Results of a fit to eq. 5.15 on the N5 ensemble.

The data extracted with the summation method are in good agreement with the values extracted from the excited state fits and the one from the plateau fit to the largest t_s on this data set. This is not always true and the values extracted with the summation method can be much larger than the one from the largest plateau. However, it is usually in good agreement with the results from the excited state fits but with the advantage that no assumptions have to be made about the gap .
The drawback of the method is the relative large statistical error and the high simulation costs. Each new value for t_s needs a new computation of an extended propagator and a new contraction. However, we believe that this interchange is worth it because it is difficult to estimate these systematic effects a priori. In addition the statistical error can be decreased by using more configurations and more source positions and by the use of the symmetries discussed in chapter 3.3.

5.2 Excited state contributions revisited

It was shown that excited state contributions cannot be ignored for nucleon matrix elements. The situation is summarized in figure 5.5 for the renormalized axial charge extracted with the standard plateau method for all values of t_s and all ensembles except A4 and A5 (see appendix A). In the left panel the data are plotted against $m_\pi L$ which characterizes the size of volume effects. One can see that for large $m_\pi L$ the plateaux for different values of t_s agree within their statistical errors. These points are from

simulations with the largest pion masses and hence the gap should be large. The same situation can be observed for the smallest values of $m_\pi L$. This may come from an interplay of volume effects and excited state contributions. In the region $5 < m_\pi L < 7$ large contributions from excited states can be observed.
In the right panel of fig. 5.5 g_A is plotted against $\exp(-2m_\pi t_s)$ which is a parameter for the size of excited state contributions. One can see a clear trend towards larger values for g_A for smaller values of the excited state contributions. This is a clear indication that these effects have to be controlled carefully on all ensembles and for all quantities.

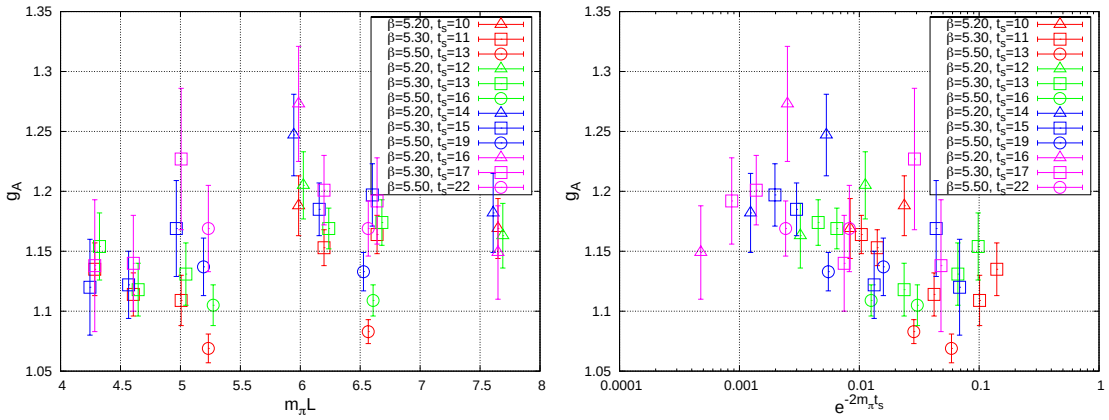

Figure 5.5: Summary of all points for the renormalized axial charge extracted with the standard plateau method for all values of t_s and all ensembles except A4 and A5. In the left picture the data are ordered according to their volume effects proportional to $m_\pi L$ and in the right picture to the size of the excited states $\exp(-2m_\pi t_s)$.

The momentum transfer dependence of the form factors is effected by excited state contribution as well. Figure 5.6 shows the electric and magnetic form factors for four values of t_s and the summation method. It can be seen that the contribution from excited states are large for small q^2 in both cases. The form factors seem to be much steeper which would lead to larger radii. For the magnetic form factor this would lead to a larger value of the magnetic moment as well. It will be discussed in chapter 6 in detail but at this point it should be noted that this is a large improvement.

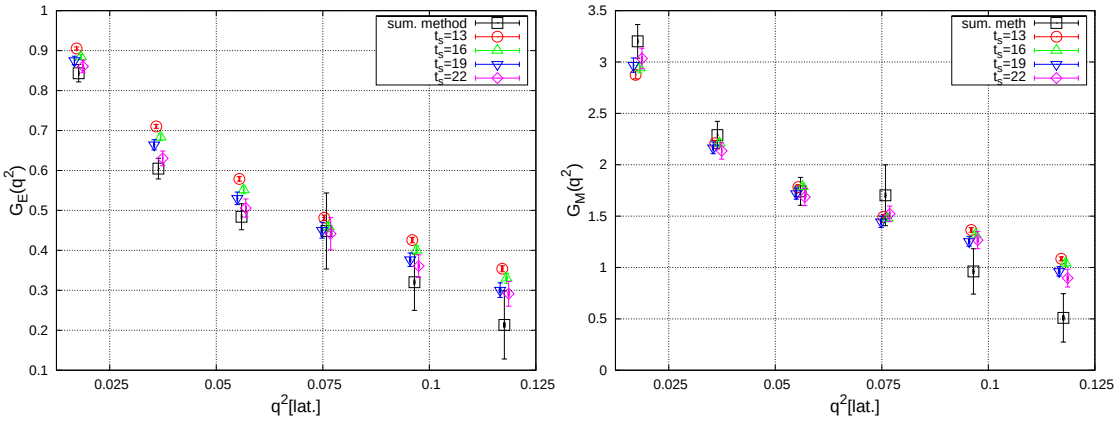

Figure 5.6: The left picture shows the electric form factor $G_E(q^2)$ and the right one the magnetic form factor $G_M(q2)$ on the N5 ensemble for the local currents. Different colors represent different values for t_s while the black points come from the summation method. The maximal momentum transfer is roughly $q^2_{\text{max}} = \frac{0.12}{a^2}\hbar c = 1.86\text{GeV}^2$.

Two papers were published recently, one by the European Twisted Mass Collaboration (ETMC) [34] and one by the ALPHA collaboration [22]. Both investigated excited state contributions.

The ETM collaboration has concentrated on the axial charge and the unpolarized isovector parton distribution $\langle x \rangle_{u-d}$ by using the fixed sink and the fixed operator method on one lattice ensemble with a pion mass of $\approx$ 380MeV and a lattice spacing of 0.078fm. They used 2+1+1 flavor twisted mass fermions to generate this ensemble. Their results are shown in figure 5.7.

The experimental values are represented by the dark grey band while the lattice data from the fixed sink method is represented by the light grey band. The fixed operator method is used to investigate excited state contributions from the sink. The operator is inserted at a relative large time separation of $9a$ where no excited state contributions have been observed in the effective mass. Through the fixed operator method it is possible to shift the sink position in Euclidean time without any new computations of the extended propagator. One can see that these data points (red) build a very good plateau for the axial charge. The situation changes for the unpolarized isovector parton distribution, where large excited state contributions can be observed.

It seems surprising that the ETMC does not see contributions from excited states to the axial charge what is in contradiction to our observations. However, they may be in the lucky position that they used an optimal source and sink smearing which was able to

reduce these effects to a minimum. On the other hand it is possible that other systematic effects like volume effects contaminate their results. The value $m_\pi L$ is around 4.8 which is in the region where we may not see large excited state contribution either, see the left picture in fig. 5.5. In addition, the time separation of the source and the operator in the fixed operator method is too small and excited state contributions from both sides may overlap and a fake plateau is built.

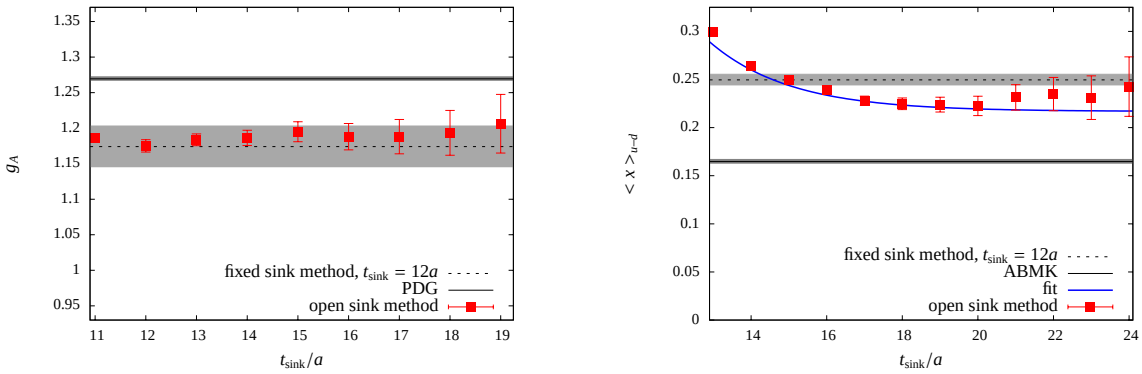

Figure 5.7: ETMC data [34] for the axial charge and the unpolarized isovector parton distribution for the fixed sink and the fixed operator method. The experimental values are shown as dark grey lines. The light grey error band indicates the values extracted from a plateau for $t_s = 12a \approx 0.94$ fm. The values which are computed with the fixed operator method are shown as red points, where the source-operator distance is fixed at $t_{\text{operator}} - t_{\text{initial}} = 9a \approx 0.7$ fm.

The ALPHA collaboration has used toy models to investigate the effectiveness of various methods to control excited state contributions. Matrix elements are constructed with small and large excited state contributions. In figure 5.8 both models are shown, in the left panel the one with small excited state contributions and in the right panel the model with large contributions. The scale r_0 is in principle arbitrary and it was set to $r_0 \approx 0.5$fm to get a realistic situation comparable to QCD.
The grey dotted and dashed lines show the situation for the standard plateau method and the summation method for two choices of sources (k=1,2). One can see, that the summation method is far superior to the standard plateau method, because the ground state value is reached earlier in terms of t/r_0. Another used method to reduce excited state contributions is the generalized eigenvalue problem (GEVP) [16] which is represented by the red lines. It converges even earlier to the ground state than the summation method.

In this method a basis of different smearing levels is used to build a matrix of correlation functions $C(t)$. The solution $\lambda_n(t, t_0)$ of the equation $C(t)\nu(t, t_0) = \lambda_n(t, t_0)C(t_0)\nu(t, t_0)$ where $t > t_0$ is directly related to the different energy levels. This method is usually used in spectroscopy because it provides not only informations about the ground states but also about the excited states.

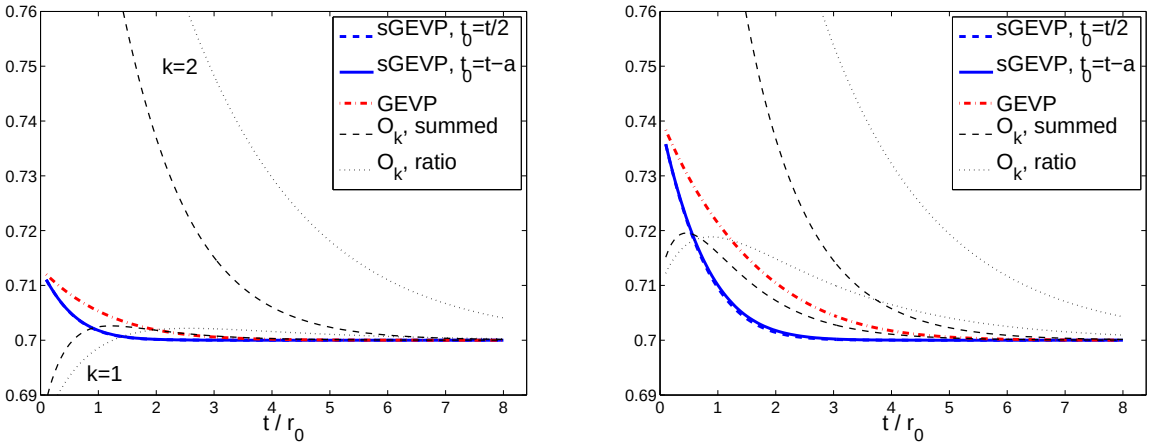

Figure 5.8: Data from the ALPHA collaboration [22]. The left picture shows the ground state matrix elements of a model with small excited state contributions. The right one shows a model with large contributions. Different methods have been used to control excited state contributions: the standard plateau method (ratio), the summation method (summed), the GEVP (Generalized EigenValue Problem) and a combination of GEVP and summation method (sGEVP). Two different kinds of sources have been used for the ratio and the summation method (k=1,2).

A new method was developed in addition, a combination of the GEVP and the summation method which is called sGEVP. It seems to be the best method to minimize contributions from excited state (blue lines). The ALPHA collaboration claim in their paper that a good tuning of all parameters can lead to a significant improvement in the reduction of excited state contributions without a dramatic increase in CPU time. The great advantage is, that smaller values for t_s can be used which would lead to smaller statistical errors.

5.3 Fitting form factors

The matrix elements for form factors are extracted with the summation method for each momentum transfer q. At large momentum transfers it happened that the statistical noise is so large that the summation method was not applicable. Whenever that happened the results from excited state fits were used instead. The form factor data at each momentum transfer were plotted against the momentum transfer squared and fitted with several functions. This was done in lattice units without renormalization and the radii were then normalized with the lattice spacing. The coupling constants are dimensionless and there is no need for normalization.
The standard way of fitting the nucleon form factor is a dipole fit of the form

$$F(q^2) = \frac{F(0)}{(1 + MQ^2)^2} \tag{5.16}$$

with the two free parameters $F(0)$ and M. Another often used form is the tripole

$$F(q^2) = \frac{F(0)}{(1 + MQ^2)^3}. \tag{5.17}$$

In [48] a more generalized fit function was used

$$F(q^2) = \frac{F(0)}{1 + c_1 Q^2 + c_2 Q^4} \tag{5.18}$$

with the three free fit parameters $F(0)$, c_1 and c_2. The derived quantities (the coupling constants and the radii) are in very good agreement within their statistical errors for all three methods. However, the statistical error of the dipole fit is the smallest, so these fit results will be taken to compute the physical quantities.
We perform individual fits to the local and the conserved electro-magnetic form factors. The only difference in both data sets should be the vector renormalization constant Z_V and discretization effects of $\mathcal{O}(a)$, so a combined fit to both data sets is done with three free fit parameters $F_{\text{loc.}}(0)$, $F_{\text{csv.}}(0)$ and M. Please note, that the local current was not renormalized for the form factor fits because we are interested in the derived quantities where the renormalization factor drops out. The results of the dipole fits to the N5 ensemble data are shown in figure 5.9 and summarized in table 5.4. One can see that the values for the individual fits and the combined fits agree very well within their statistical

errors.

	conserved	local (bare)	combined	
$G_E(0)$	0.9999(2)	1.307(2)	0.999(2)	1.307(2)
M_E	11.8(9)	12.7(9)	12.3(9)	
$G_M(0)$	3.36(27)	4.71(37)	3.35(27)	4.73(38)
M_M	12.0(2.1)	11.8(2.1)	11.9(2.0)	

Table 5.4: Dipole fit results for the local, conserved and combined fits.

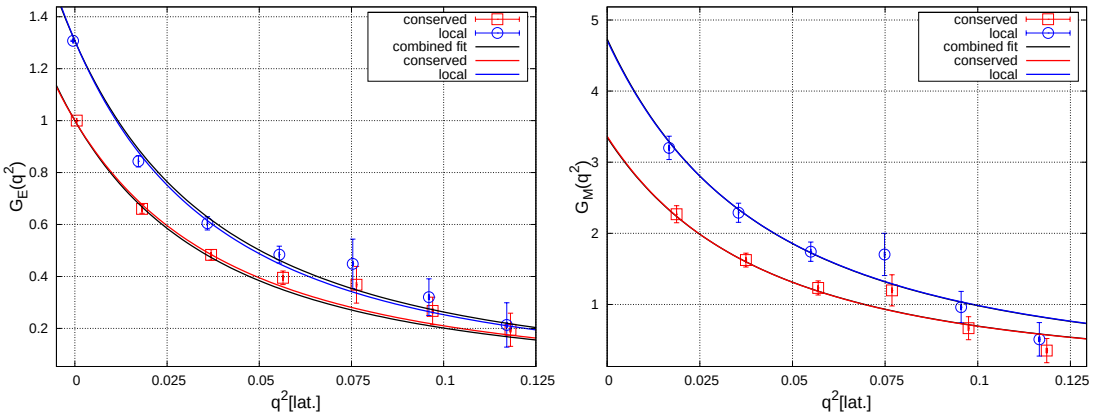

Figure 5.9: The left picture shows the electric form factor $G_E(q^2)$ and the right one the magnetic form factor $G_M(q2)$ on the N5 ensemble for the bare local (blue) and conserved (red) currents. The colored lines represent the individual uncorrelated fits to the local and the conserved data sets. The black line represent a combined fit to both data sets.

It is assumed in phenomenology that the radii for the electric and magnetic form factors should be very close to each other. The ratio $\frac{\mu G_E(q2)}{G_M(q2}$ is often plotted [14] to verify this issue. One can usually see small deviations from this behavior for momentum transfers smaller than 1 GeV^2. However, the statistical errors in lattice QCD are usually larger than in experiments and one may not see these deviations there. This fact can be used to get a better access to the magnetic form factor at zero momentum transfer, the magnetic moment of the nucleon $\mu = G_M(0)$.
The ratio $\mu = \frac{G_M(q^2)}{G_E(q^2)}$ is plotted in figure 5.10 for the local and the conserved currents. In general two different fit functions have been used, a constant fit which is shown in the

figure and a linear fit in q^2 with two free fit parameters. The reduced χ^2 is close to one in both cases and the fit results agree within their statistical errors for the extrapolated value $\mu = \frac{G_M(0)}{G_E(0)}$. The linear fits have a much larger error than the fits to a constant, so the constant fit is used in general. The difference in the fit results to the local and conserved data will be discussed later in this chapter. The advantage of this method is that the vector renormalization constant drops out in this ratio because both form factors are extracted from the electro-magnetic current.
If it is assumed that the radii of the electric and magnetic form factors are equal, a combined fit with five fit parameters to all four data sets can be done. The result is shown in the right picture of figure 5.10 for the N5 ensemble. The values at zero momentum transfer for the magnetic form factor are from the constant extrapolation of $\frac{G_M(q^2)}{G_E(q^2)}$. The fit reproduces the data very well and the result is shown in table 5.5.

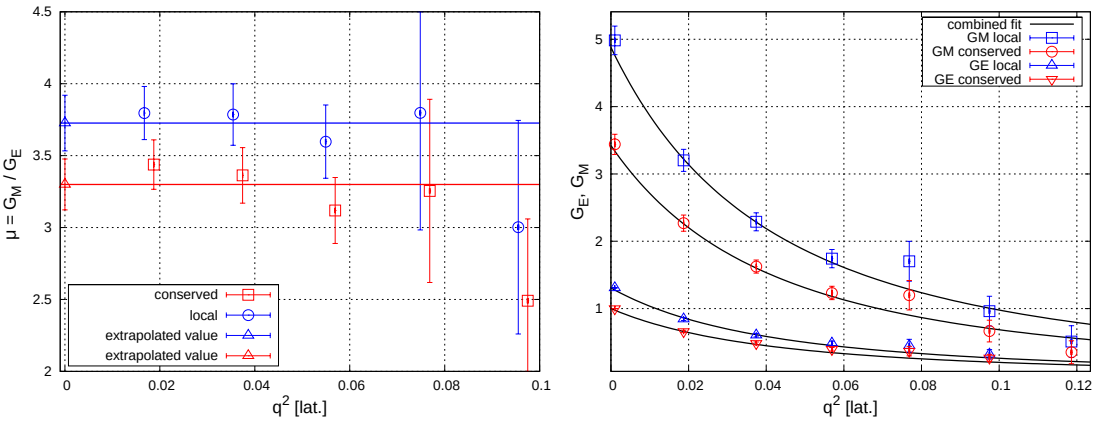

Figure 5.10: In the left picture the ratio $\mu = \frac{G_M(q^2)}{G_E(q^2)}$ for the local and conserved data is shown. The right picture shows a combined fit to all electro-magnetic data sets on the N5 ensemble. The values for $G_M(0) = \mu$ are taken from the extrapolation of $\frac{G_M(q^2)}{G_E(q^2)}$ to zero momentum transfer.

	$G_E(0)$	$G_M(0)$	M
local (bare)	1.307(2)	4.88(21)	12.3(9)
conserved	0.9999(2)	3.42(15)	

Table 5.5: Fits results to a combined fit to all data sets.

It is remarkable that the fit results do agree within their statistical errors with the indi-

vidual fits. The statistical error of the magnetic moment of the nucleon is smaller for the constant fit to the ratio $\frac{G_M(q^2)}{G_E(q^2)}$ than for the form factor fit. Both values agree very well within statistics. The value extracted from the ratio will be used later to determine the chiral dependence of the magnetic moment.
The axial form factors are shown in figure 5.11. The left panel shows $G_A(q^2)$ and the right one $G_P(q^2)$. A dipole fit to both form factors was used to extract their coupling constants at zero momentum transfer and their radii. The missing point at a momentum transfer around $q^2 \approx 0.055$ comes from the way how these form factors are extracted. This momentum transfer corresponds to the Fourier momentum $q = (1,1,1)\frac{2\pi}{L}$ where $G_A(q^2)$ and $G_P(q^2)$ cannot be disentangled.

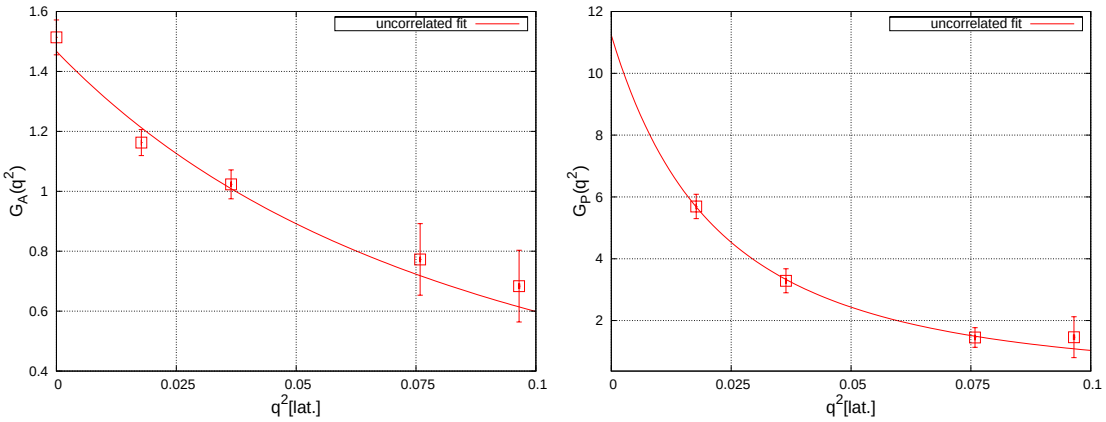

Figure 5.11: The unrenormalized axial form factors $G_A(q^2)$ and $G_P(q^2)$.

5.4 $\mathcal{O}(a)$-improvement of the currents

A discrepancy in the local and conserved data for the ratio $\frac{G_M(q^2)}{G_E(q^2)}$ can be observed in figure 5.10. One explanation of the difference are discretization effects which are of oder $\mathcal{O}(a)$. It was already mentioned that the vector and axial-vector currents can be $\mathcal{O}(a)$-improved. The leading order discretization effects are shifted to the order $\mathcal{O}(a^2)$, see chapter 2.5. The explicit form of the improved currents was presented in eq. 2.89 and is repeated here

$$(A_I)_\mu(x) \quad = \quad A_\mu(x) + c_A a \partial_\mu P(x),$$

$$(V_I)_\mu(x) \quad = \quad V_\mu(x) + c_V a \partial_\nu T^{\nu\mu}(x).$$

The derivatives of the pseudo-scalar density $P(x)$ and the tensor field $T^{\nu\mu}(x)$ are needed to do the improvement. At the moment spatial derivatives of these operators are implemented in the code but not tested yet, so they were not computed in our simulations. This means that only the time derivatives can be performed, because the correlation functions are only time dependent. This improvement for our choice of the axial current would be

$$(A_I)_3(x) = A_3(x) + c_A a \partial_3 P(x). \tag{5.19}$$

It follows that the improvement term cannot be computed for the axial current at the current status of the project because of the spatial derivative. It is the same situation for the electric form factor where the improved current is

$$G_E \propto (V_I)_0(x) = V_0(x) + c_V a \partial_\nu T^{\nu 0}(x), \tag{5.20}$$

where $\partial_i T^{i0}(x)$ can not be computed because of the previous mentioned reasons and $T^{00}(x)$ is zero. However, one can get an impression of the size of the improvement for the magnetic form factor. It is proportional to

$$G_M \propto (V_I)_{1,2}(x) = V_{1,2}(x) + c_V a \partial_\nu T^{\nu(1,2)}(x) \tag{5.21}$$

and the time derivative can be computed. It is averaged over the spatial components to improve statistics and the derivative term is shown in figure 5.12 for the smallest momentum transfer on the F6 ensemble. The data are extracted from a plateau fit which is shown in the left picture and the summation method in the right picture. The dependence of the improvement term on the momentum is shown in table 5.12.

$(aq)^2$	0.0175	0.0358	0.0546	0.0738	0.0936
$\partial_0 T^{0(1,2)}$	0.175(56)	0.191(47)	0.208(49)	0.134(65)	0.168(53)

Table 5.6: Results of the improvement Term T on the F6 ensemble extracted with the summation method.

One can see that the improvement term is constant in the momentum transfer within sta-

tistical errors. This means that the effect becomes more and more important at higher q^2 values because the improvement term stays constant but the form factor becomes smaller. This effect can be understood because one gets closer to the momentum cutoff at $\frac{\pi}{a}$ with increasing momentum transfer.

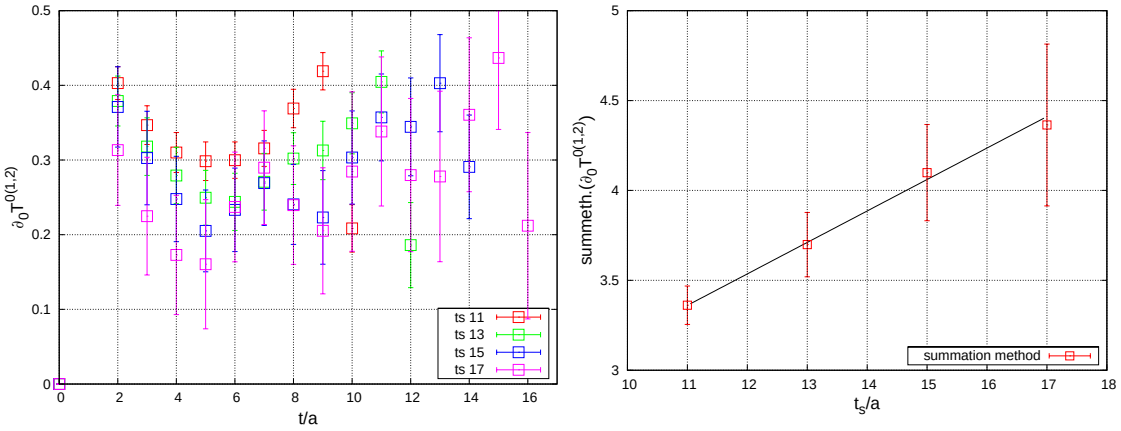

Figure 5.12: The contribution $\partial_0 T^{0(1,2)}$ to the improvement term of the magnetic form factor on the F6 ensemble for the smallest momentum transfer. This ensemble was chosen because the statistics are as good as for the N5 ensemble but the discretization effects should be larger. The ratios for different values for t_s are shown in the left panel and the summation method result is shown in the right panel.

The coefficient of the local vector current $c_V^{\text{loc.}}$ is known perturbatively [17] up to one-loop and can be computed via the formula

$$c_V^{\text{loc.}} = -0.01225\frac{4}{3}g^2, \tag{5.22}$$

while the one for the conserved current is only known at tree level which is zero. The values for the local improvement coefficients are summarized in table 5.7.

β	5.2	5.3	5.5
g^2	1.15	1.13	1.09
c_V^{loc}	0.019	0.018	0.018

Table 5.7: The improvement coefficient c_V^{loc} for three values of β.

This makes a quantitative comparison of discretization effects for the local and conserved currents impossible at the moment. However, the small values for $c_V^{\text{loc.}}$ and a value of the derivative around 0.18 impose cut-off effects smaller than 1%. The values for μ for the local and conserved currents on the F6 ensemble are $\mu^{\text{loc.}} = 4.25(43)$ and $\mu^{\text{csv.}} = 3.69(38)$. The deviation of the mean values is around 0.56 which larger than the individual statistical errors and much larger than the expected cut-off effects. A detailed analysis of discretization effects is needed but must be postponed to later simulations.

Chapter 6

Results

6.1 The PCAC-relation, $\kappa_{\text{crit.}}$ and quark masses

The bare subtracted quark mass

$$am_q = \frac{1}{2}\left(\frac{1}{\kappa_v} - \frac{1}{\kappa_c}\right), \tag{6.1}$$

is needed for the $\mathcal{O}(a)$-improvement of the vector and axial-vector renormalization constant where κ_c is the hopping parameter at vanishing quark mass. The $\mathcal{O}(a)$-improved renormalization constants are defined as

$$Z_V^I = Z_V(1 + b_V am_q), \tag{6.2}$$
$$Z_A^I = Z_A(1 + b_A am_q). \tag{6.3}$$

The factor b_A is known only perturbatively but tadpole improved [15] (ultraviolet divergent contributions to eq. 2.44 proportioal to the coupling constant are removed) and can be computed via

$$b_A^{\text{TI}} = u_0^{-1}\left(1 + \left(0.11414 \cdot \frac{4}{3} - \frac{1}{12}\right)\frac{g_0^2}{u_0^4}\right) \tag{6.4}$$

with $u_0 = 1 - \frac{1}{12}g_0^2 + \mathcal{O}(g_0^4)$. The factor b_V is not needed because we use the conserved vector current which does not need to be renormalized. The local vector current will be

used to extract the vector renormalization constant and the improvement factor.
The critical hopping parameter can be computed via the pion mass which is directly related to the quark mass at lowest order of chiral perturbation theory [95]

$$m_\pi^2 = 2B_0 m_{u,d}. \tag{6.5}$$

The parameter B_0 is a low energy constant of ChPT and it is assumed that the light quarks are degenerate.
Another way to determine κ_c is via the partially conserved axial current (PCAC) relation, a Ward Identity which connects the axial current, the pseudo-scalar density and the so called PCAC mass. The unrenormalized but $\mathcal{O}(a)$-improved axial current is defined as

$$A_\mu^{\text{impr.}}(x) = \overline{\Psi}(x)\gamma_\mu\gamma_5\Psi(x) + ac_A\partial_\mu\overline{\Psi}(x)\gamma_5\Psi(x). \tag{6.6}$$

It can be renormalized by

$$A_\mu = Z_A(1 + b_A a m_q)A_\mu^{\text{impr.}}(x). \tag{6.7}$$

The renormalized PCAC-masses of two flavors i and j can be computed as follows:

$$m_i^{\text{PCAC}} + m_j^{\text{PCAC}} = \frac{Z_A(1 + b_A a m_q)}{Z_P(1 + b_P a m_q)} \frac{\left\langle (\partial_0 + \partial_0^*)A_0^{\text{impr.}}(x)\mathcal{O}\right\rangle}{\langle P(x)\mathcal{O}\rangle}, \tag{6.8}$$

where the masses m_i^{PCAC} and m_j^{PCAC} are equal for the two light quarks. Renormalization is not needed to extract κ_C because the PCAC mass is multiplicatively renormalized.
The data are shown in figure 6.1. They are extrapolated to vanishing quark masses by a linear fit in $\kappa_v^{-1} = \kappa_{\text{sea}}^{-1}$ and the results are summarized in table 6.1. The same procedure was used where the PCAC mass was replaced by the squared pion mass. This is shown in the table as well. Please note that all fits discussed in this chapter have been performed uncorrelated.

β	5.2	5.3	5.5
$\kappa_c(m_{\text{PCAC}})$	0.136051(2)	0.136456(1)	0.136779(1)
$\kappa_c(m_\pi^2)$	0.136052(2)	0.136454(1)	0.136776(2)

Table 6.1: κ_c extracted from the PCAC-mass and the pion mass.

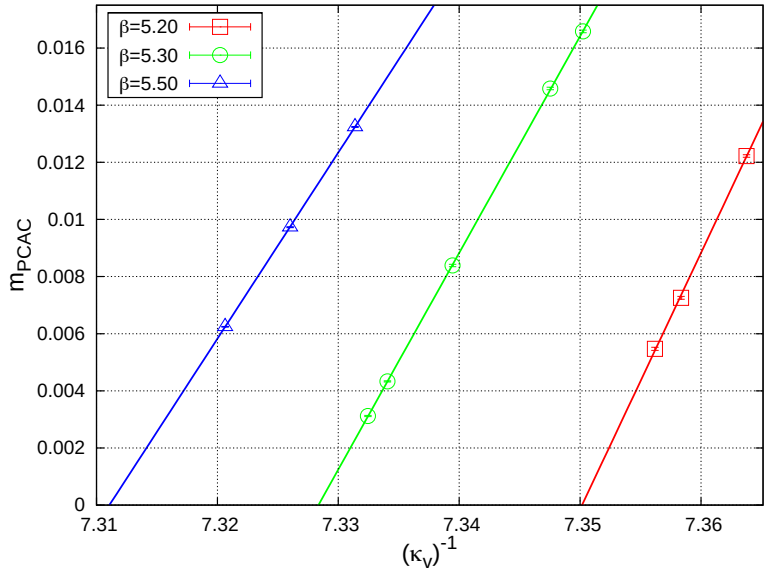

Figure 6.1: Extrapolation of the PCAC mass to the chiral point for three values of β.

The linear fit works well and the κ_c values extracted from the PCAC relation and the pion mass are statistically comparable.

The physical quark masses can be computed either from the subtracted quark mass or from the PCAC mass. The bare subtracted quark mass can be related to the bare PCAC mass via

$$\frac{Z_m Z_P}{Z_A} \frac{(1 + b_m a m_q)(1 + b_P a m_q)}{(1 + b_A a m_q)} m_q = m^{\text{PCAC}}, \tag{6.9}$$

where the factor $Z = \frac{Z_m Z_P}{Z_A}$ and the improvement coefficients were computed non-perturbatively in [44]. To be able to connect the quark masses computed on the lattice to the quark masses cited by the Particle Data Group (PDG), the lattice results have to converted into the $\overline{\text{MS}}$-scheme at a scale of $\mu = 2$ GeV.
The PCAC mass can be related to the renormalization group invariant (RGI) quark mass in an intermediate step via

$$m^{\text{RGI}} = Z_m m^{\text{PCAC}}, \tag{6.10}$$

where the parameter Z_m is known non-perturbatively [30]. The conversion factor from the RGI-scheme into the $\overline{\text{MS}}$-scheme at a scale of $\mu = 2$ GeV is given in [30] as well.
Both quark masses, the subtracted and the PCAC mass, are used to compute the physical quark masses. The renormalized quark masses in the $\overline{\text{MS}}$-scheme at a scale of $\mu = 2$ GeV are shown in figure 6.2 as a function of m_π^2. The black lines in the figures denote the experimental values of the quantities plotted on the x- and y-achsis.

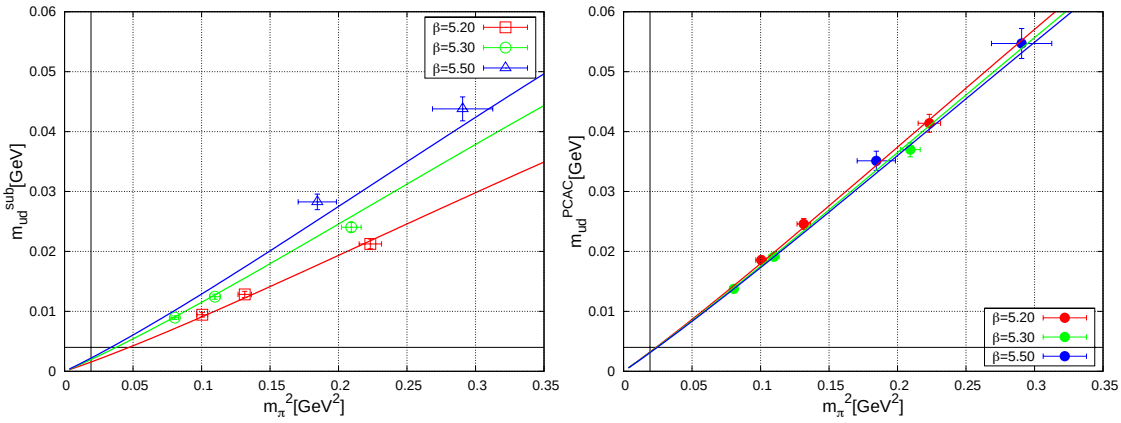

Figure 6.2: Chiral extrapolation of the light quark masses in the $\overline{\text{MS}}$-scheme at a scale of $\mu = 2$ GeV to the physical point with a maximal pion mass of ≈ 540 MeV. The left picture shows the quark mass computed from the subtracted quark mass and the right picture the quark mass computed from the PCAC quark mass. The shown fit function is defined in eq. 6.11.

One can see that discretization effects are large for the subtracted quark mass which is shown in the left panel. Hence, the $SU(2)$ chirally motivated fit function of eq. 6.5 is modified by a term proportional to a^2. In addition, it is modified by the higher order term $c_2 m_\pi^2 \log m_\pi^2$. It should be noted that the logarithm depends usually on an intrinsic scale μ with the explicit form: $\log \frac{m_\pi^2}{\mu^2}$. The ChPT formulae are independent of this scale [94] and indeed the μ dependent part can be absorbed in one of the other free fit parameters. In the fits the scale is set to 1 GeV which could become important when the fit parameters are compared to fits with an different scale μ.
The explicit form of the fit function is

$$m_{ud}(m_\pi^2) = c_1 m_\pi^2 \left(1 + c_2 m_\pi^2 \log m_\pi^2\right)\left(1 + c_3 a^2\right), \tag{6.11}$$

where c_1, c_2 and c_3 are free fit parameters. To be able to investigate systematics in the chiral extrapolation a second fit function was used where the $\log$ was Taylor expanded. Its explicit form is given by

$$m_{ud}(m_\pi^2) = \left(c_4 m_\pi^2 + c_5 m_\pi^4\right)\left(1 + c_6 a^2\right), \tag{6.12}$$

with the free fit parameters c_4, c_5 and c_6. In addition we fit our data with two cuts in the maximal pion mass: $m_\pi < 660$ MeV and $m_\pi < 540$ MeV. This is relatively heavy and sim-

ulations at smaller pion masses are needed in the future to have a smaller extrapolation range and to reduce the largest pion masses in the extrapolations. The continuum limit can easily be taken by setting $a^2 \to 0$ in both equations. All extrapolated values for both fit functions are summarized in table 6.2.

	$m_\pi < 540$ MeV		$m_\pi < 660$ MeV	
fit to:	eq. 6.11	eq. 6.12	eq. 6.11	eq. 6.12
$m_{\text{ud}}^{\text{PCAC}}$[MeV]	3.03(17)	3.14(16)	3.28(16)	3.40(16)
$m_{\text{ud}}^{\text{sub.}}$[MeV]	2.65(22)	2.82(21)	2.95(21)	3.12(20)

Table 6.2: Light quark masses in the $\overline{\text{MS}}$-scheme at $\mu = 2$ GeV in the continuum limit.

One can see that all values agree within in their statistical errors but that the values extracted from the subtracted quark mass are smaller compared to the ones from the PCAC mass. We take the lower median of the different extrapolation results as our final result for the light quark mass. The maximal deviation to the farthest point away from this point is an estimate for the systematic error of the chiral extrapolation. The final value of this analysis is

$$m_{ud}^{\overline{\text{MS}}}(\mu = 2\text{ GeV}) = 3.03(17)(38)\text{ MeV}. \tag{6.13}$$

where the first error is the statistical and the second one the systematic error of the chiral extrapolation.

The extraction of the strange quark mass is very similar to the one of the light quark mass. The bare subtracted strange quark mass is defined in the same way where κ_{sea} is changed into κ_s. No chiral extrapolation is needed in this case because the value for κ_s at the physical point was already determined in the scale setting procedure in chapter 4.
The PCAC-relation of eq. 6.8 can be used to extract the strange quark mass as well but the quark masses m_i^{PCAC} and m_j^{PCAC} of eq. 6.8 are not identical in this case. This means that the light quark mass from the previous calculation must be subtracted to separate the strange quark mass. It should be noted that all renormalization constants are the same for the light and the strange quark mass.
The fit function is motivated by Chiral Perturbation Theory and modified by a term proportional to the lattice spacing to investigate discretization effects. Its explicit form is given by

$$m_s = \left(c_1 + c_2 m_\pi^2\right)\left(1 + c_3 a^2\right), \tag{6.14}$$

where c_1, c_2 and c_3 are the free fit parameters. In addition, the term $c_4 m_\pi^4$ was added but it turned out that c_4 is statistically compatible with zero and it only blows up the error on the extrapolated value. Two different cuts in the maximal pion mass have been investigated (460 and 540 MeV) but the deviation in the extrapolated values was close to zero. The data points and the fits for the renormalized strange quark mass extracted from the PCAC mass are shown in figure 6.3.

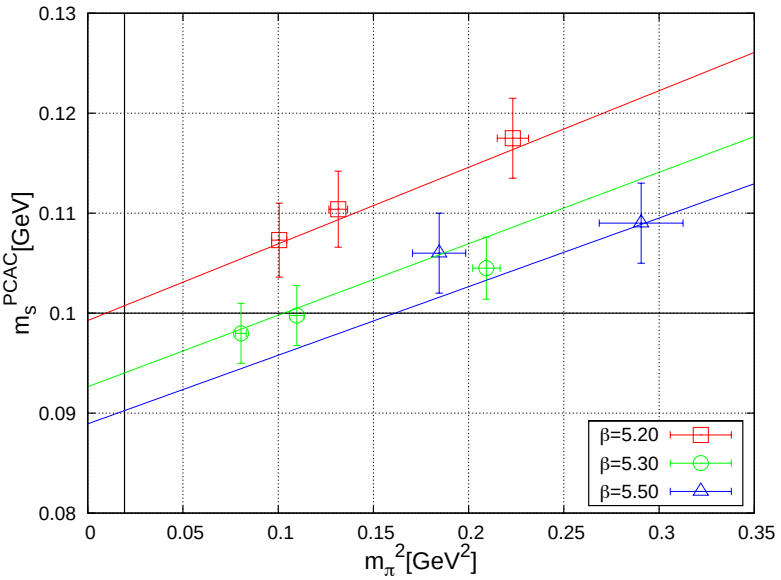

Figure 6.3: Chiral extrapolation of the strange PCAC-mass in the $\overline{\text{MS}}$-scheme at $\mu = 2$ GeV to the physical point.

No chiral extrapolation is needed for the strange quark mass computed from the subtracted quark mass but a continuum extrapolation is necessary. Two fits have been performed in a^2, a constant fit, and a linear fit. Both fits are shown in figure 6.4. The extrapolated values for the strange quark mass are

$$(m_s^{\text{sub}})_{\text{const}} = 85.4(2.9)\text{ MeV}, \quad (m_s^{\text{sub}})_{\text{lin.}} = 92.7(4.6)\text{MeV}, \tag{6.15}$$

$$(m_s^{\text{PCAC}}) = 83.2(4.0)\text{ MeV}. \tag{6.16}$$

The values of the strange quark mass extracted from the PCAC mass and the subtracted mass (linear fit) do not agree well. To be able to guess the size of the discretization effects on the PCAC mass, a naive fit without the fit parameter c_3 was performed. The results is $(m_s^{\text{PCAC}})_{c_3=0} = 98.1(3.3)$ MeV. At this stage, we cannot give a final number for the

strange quark mass because the discrepancies in the extracted values are too large but we can guess the systematic error from discretization effects. It varies from 7.3 MeV for the subtracted quark mass up to 14.9 MeV for the PCAC mass which is a $8 - 14\%$ effect.

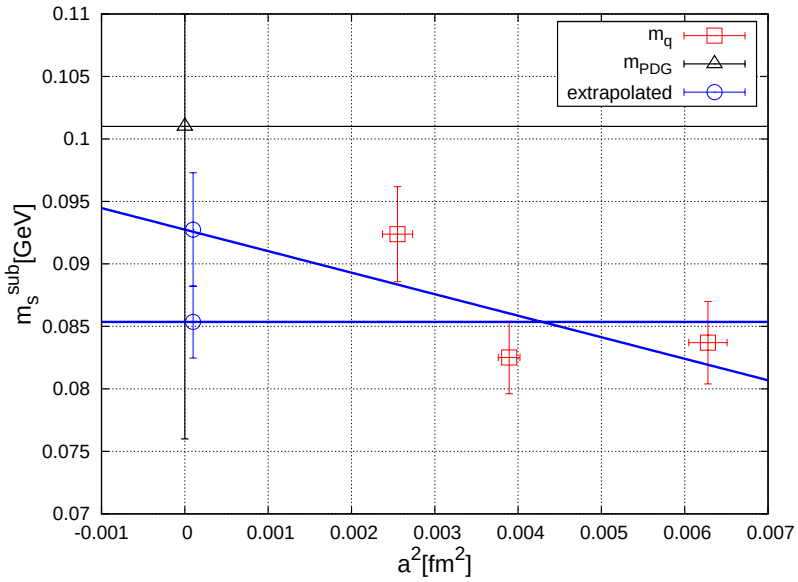

Figure 6.4: Continuum limit of the strange quark mass extracted from the subtracted quark mass in the $\overline{\text{MS}}$-scheme at $\mu = 2$ GeV.

The experimental data from the Particle Data Group [7] for the quarks are

$$m_{ud}^{\overline{\text{MS}}}(\mu = 2\,\text{GeV})_{\text{PDG}} \approx 3.5\,\text{MeV}, \tag{6.17}$$

$$m_{s}^{\overline{\text{MS}}}(\mu = 2\,\text{GeV})_{\text{PDG}} = 104^{+26}_{-34}\,\text{MeV}, \tag{6.18}$$

where m_{ud} is just the average over the values for the d- and u-quark mass. Results from other lattice collaborations are collected by the FLAG working group in [23]. Their global estimates for $N_f = 2$ lattice simulation results are

$$m_{ud}^{\overline{\text{MS}}}(\mu = 2\,\text{GeV})_{\text{FLAG}} = 3.6(2)\,\text{MeV}, \tag{6.19}$$

$$m_{s}^{\overline{\text{MS}}}(\mu = 2\,\text{GeV})_{\text{FLAG}} = 95(6)\,\text{MeV}. \tag{6.20}$$

Our light quark mass is in agreement with the PDG and the FLAG data within errors but is lower than those. Both values of the strange quark mass are in agreement with the PDG and FLAG data within their statistical and systematic errors. However, the large

systematic of the strange quark mass must be investigated in the future.

6.2 Meson and baryon masses

Some hadron masses have been already computed to set the scale. These masses will be extrapolated to the physical point and into the continuum.
The kaon mass m_K is shown in figure 6.5 in dependence of the squared pion mass. The fit function is motivated by Chiral Perturbation Theory and is given by

$$m_K = (c_1 + c_2 m_\pi^2 + c_3 m_\pi^4)(1 + c_4 a^2). \tag{6.21}$$

One would usually expect that the squared kaon mass depends on the squared pion mass. However, extracting the square root and Taylor expanding in m_π^2 would lead to eq. 6.21. The fit function is upgraded with a lattice spacing dependent part $c_4 a^2$. This is necessary to perform the continuum extrapolation. The four free fit parameters are the c_i.

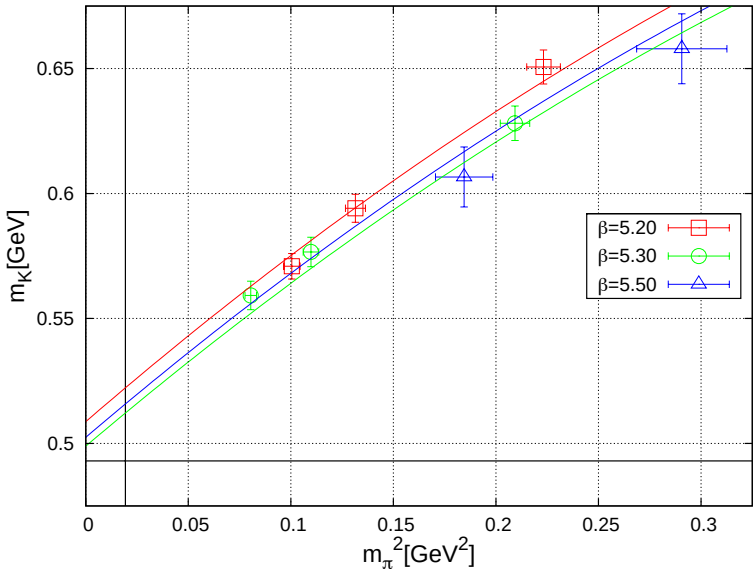

Figure 6.5: Chiral extrapolation of the kaon mass m_K.

To get an estimate of the systematic effect of the chiral extrapolation, the fit has been performed with three different cuts in the maximal pion masses of roughly 660, 540 and 450 MeV. The extrapolated value depends only very weak on the maximal pion mass. Hence,

the chiral extrapolation is very stable.
The parameters c_3 and c_4 are statistically compatible with zero and the extrapolated values are compatible to a fit where these two parameters were left out. However, one might see a trend in the lattice spacing (β values) towards smaller values of the kaon mass for larger values of β in fig. 6.5 which is not correctly reproduced by the fit. This may come from the large errors of the kaon masses for the largest β value which do not constrain the fit enough.
The systematic effects seem to be small because of the afore mentioned reasons. Our final value for the kaon mass is $m_K = 505(10)$ MeV which is the continuum and chiral extrapolated value of a fit to eq. 6.21 with the maximal pion mass of roughly 540 MeV. Although the strange quark is not dynamical, the chirally and continuum extrapolated value for the kaon mass is in statistical agreement with the PDG value of $493.677(16)$ MeV.
The ρ and K^* vector mesons are resonances and have a decay width. It is difficult to treat them correctly in lattice QCD [40, 43]. The analysis presented here is somewhat naive because it is assumed that the vector mesons are stable particles. It was already seen in the chapter about the scale setting procedure that the ratios including the vector masses are not as stable as the ratio with the Ω mass. The masses are shown in figure 6.6 and 6.7. Several fits have been done. First of all a naive fit of the form

$$m_V = c_1 + c_2 m_\pi^2 \tag{6.22}$$

to all data points and then to each individual value of β. To investigate discretization effects and the dependence on the chiral behavior a fit to eq. 6.21 has also been performed. The results of the a^2 dependent fit are shown in the left pictures and the individual fits are shown in the right pictures of the figures 6.6 and 6.7. The naive fit to all data points is shown in all pictures and is represented by the black line.

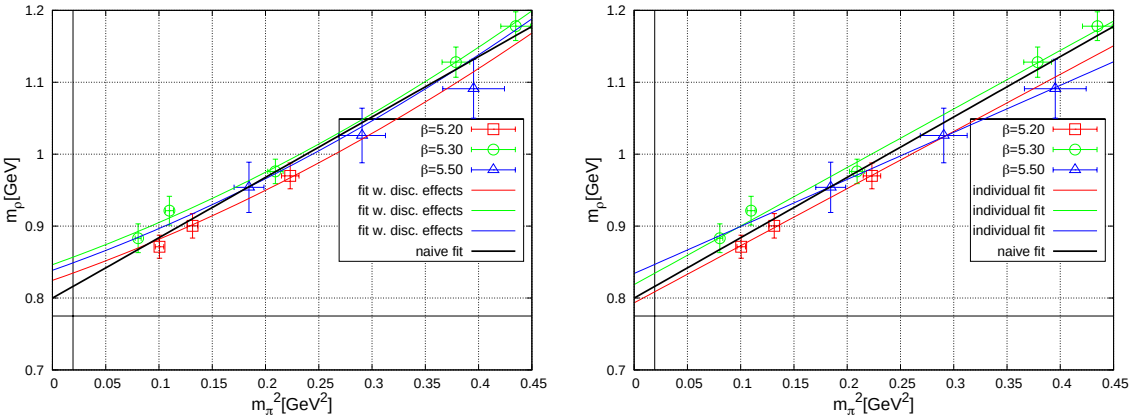

Figure 6.6: Chiral extrapolation of the ρ-meson mass. The left picture shows the chiral extrapolation with the fit function of eq. 6.21 and the right picture shows the extrapolation with individual chiral fits with eq. 6.22.

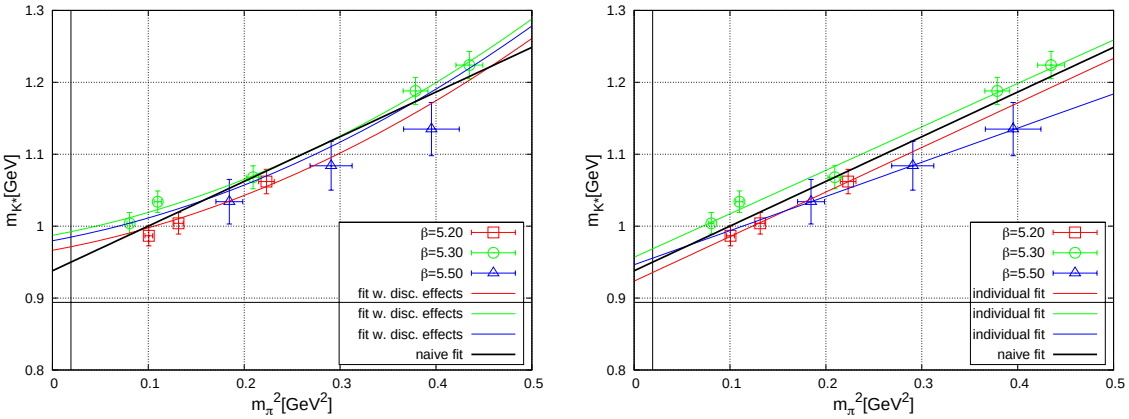

Figure 6.7: Chiral extrapolation of the K^*-meson mass. The left picture shows the chiral extrapolation with the fit function of eq. 6.21 and the right picture shows the extrapolation with individual chiral fits with eq. 6.22.

The fits to eq. 6.21 have been performed with three different maximal pion masses of 660, 540 and 450 MeV. It turned out that the parameters c_3 and c_4 are statistically compatible with zero and that the extrapolated values agree very well and are almost independent of the maximal pion mass. In addition, the extrapolated value of the mass are in a very good agreement with the naive fit. Finally, no clear trend in the dependence of the lattice spacing can be seen except in the individual fits to the different β values of the rho meson mass. Unfortunately, the trend shows the wrong direction to larger masses what

is certainly not correct. This means that cut-off effects and the dependence on the chiral extrapolation seem to be small. At the moment it seems reasonable to quote the value from the naive fit with the maximal pion mass of 660 MeV as our best estimate for the vector meson masses. These are

$$m_\rho = 0.816(11)\ \text{GeV} \qquad m_{K^*} = 0.950(9)\ \text{GeV} \tag{6.23}$$

where no systematic error can be presented. However, the systematic errors are certainly large because of the naive treatment of the resonances. Finally, our data do not agree with the PDG values for the $\rho(770)$ mass $m_\rho = 775.49(34)$MeV and for the $K^*(892)^\pm$ mass $m_{K^*} = 891.66(26)$MeV.

The nucleon and Δ-baryon masses are shown in picture 6.8. Two different fits have been used for the nucleon mass, both motivated from HBChPT [4] but of different order. These are

$$m_B(p^3) = c_1 + c_2 m_\pi^2 + c_3 m_\pi^3, \tag{6.24}$$

and

$$m_B(p^4) = m_B(p^3) + c_4 m_\pi^4 + c_5 m_\pi^4 \log m_\pi. \tag{6.25}$$

The fit of $\mathcal{O}(p^3)$ works well but the errors on all five fit parameters of the fit to $\mathcal{O}(p^4)$ are of the order of 100%.

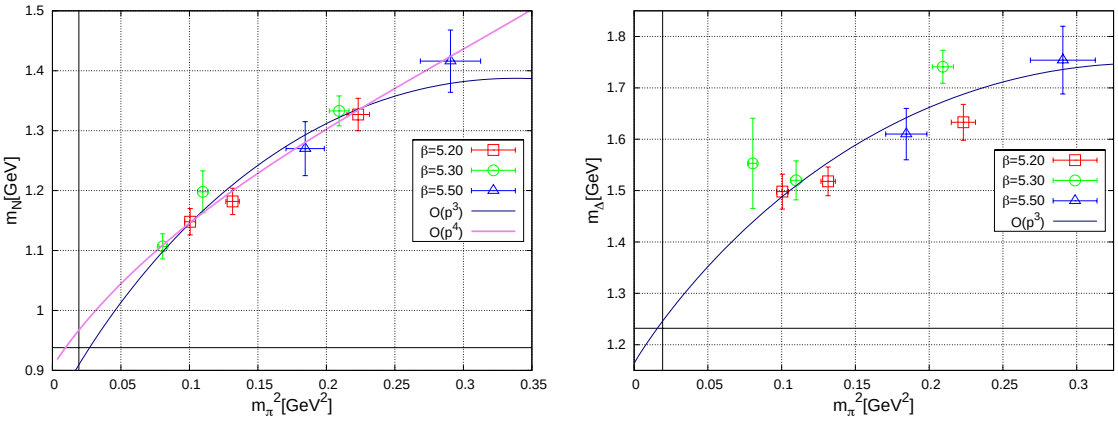

Figure 6.8: Chiral extrapolation of the nucleon and the Δ-baryon mass.

The chiral expression of the parameter c_3 for the nucleon is given by

$$c_3 = -\frac{3g_A^2}{32\pi f_\pi^2} \tag{6.26}$$

and it can be fixed by the experimental values of the axial charge $g_A = 1.26$ and the pion decay constant $f_\pi = 0.092$ GeV. This reduces the free fit parameters to 2 (4) with the effect that the errors on the left free parameters is reduced. The parameter c_5 can also be fixed and expressed by a linear combination of $1/c_1$ and c_2. It is given by

$$c_5 = -\frac{3}{32\pi^2 f_\pi^2}\left(a - 2c_2 + 4b\frac{g_A^2}{c_1}\right), \tag{6.27}$$

where the low energy constants $a = 3.2\,\text{GeV}^{-1}$ [41] and $b = -3.45\,\text{GeV}^{-1}$ [90, 13] are known. The effect of this fixing is the reduction of the errors on the left three free fit parameters and hence on the chiral extrapolation. The other three free fit parameters cannot be fixed because they are not known experimentally or the constraints to the fits (only one free fit parameter in eq. 6.24) are too large.
The value for c_3 in a completely free fit to eq. 6.24 was roughly 7 with 80% error which is in a good agreement with the constraint value of 5.68. The parameter c_5 was in the fixed and the non fixed case compatible with zero within its error.
The dependence on the lattice spacing has been investigated in the fit to eq. 6.24 to the nucleon with and without the fixing of c_3 with the additional term $(1 + c_a a^2)$. It turned out that the parameter c_a was compatible with zero in both cases, so cut-off effects should be small.
Both fit functions with fixed coefficients have been used with three different cuts in the maximal pion mass: 660, 540 and 450 MeV and the results are summarized in the table 6.4.

fit to:	$m_\pi < 450$ MeV	$m_\pi < 540$ MeV	$m_\pi < 660$ MeV
eq. 6.24	950(30) MeV	909(16) MeV	829(11) MeV
eq. 6.25	977(88) MeV	967(30) MeV	962(18) MeV

Table 6.3: Fit results of the nucleon mass.

It can be seen that the fit to $\mathcal{O}(p^4)$ is very stable in the maximal pion mass, only the statistical error grows. The fit to $\mathcal{O}(p^3)$ shows a trend towards higher values of the nucleon

mass with an simultaneous error growth. This can be a hint that the chiral extrapolation of the nucleon mass is potentially dominated by the relative large pion masses. This situation has to be investigated in more detail in the future when smaller pion masses will be accessible. At the moment it seems to be save to quote $m_N = 977(88)$ MeV as our best estimate for the nucleon mass. Within this large statistical error this value is in good agreement with the PDG value of $m_N = 938.27203(8)$ MeV.
The Δ mass was only fit with eq. 6.24 because the next higher order becomes rather complicated [102]. As for the nucleon, it is possible to fix the fit parameter c_3 which is given by

$$c_3 = -\frac{25}{81}\frac{3H_A^2}{32\pi f_\pi^2} \tag{6.28}$$

in HBChPT where the parameter H_A is known in SU(6) chiral perturbation theory: $H_A = \frac{9}{5}g_A$. It follows, that the $\mathcal{O}(p^3)$ fit function for the Δ has the same form as for the nucleon. The discretization effects on the Δ mass have been investigated in the same way as for the nucleon mass and have found to be small. The fit results with three different maximal pion masses are summarized in table 6.4.

fit to:	$m_\pi < 450$ MeV	$m_\pi < 540$ MeV	$m_\pi < 660$ MeV
eq. 6.24	1297(37) MeV	1246(32) MeV	1163(22) MeV

Table 6.4: Fit results of the Δ mass.

One can see a trend to larger values of the mass with the decreasing cut in the maximal pion mass. This is not surprising and can be observed in the chiral extrapolation of the nucleon mass as well. The value from the fit with the smallest maximal pion mass is mainly dominated by the values at the four smallest pion masses which could build a plateau in m_π^2. Finally, it seems reasonable to quote $m_\Delta = 1246(32)$ MeV as our best fit value for the Δ mass which is in good agreement with the PDG value of $m_\Delta \approx 1232$ MeV.

6.3 Nucleon charges and radii

6.3.1 Vector renormalisation constant Z_V and improvement coefficient b_V

The vector renormalization constant can be computed from the local electric form factor at zero momentum transfer via the condition

$$Z_V(1 + b_V am_q)G_E^{\text{loc.}}(q^2 = 0) = Q = 1, \tag{6.29}$$

where Q is the charge of the nucleon. It is plotted against the bare quark mass am_q in figure 6.9.

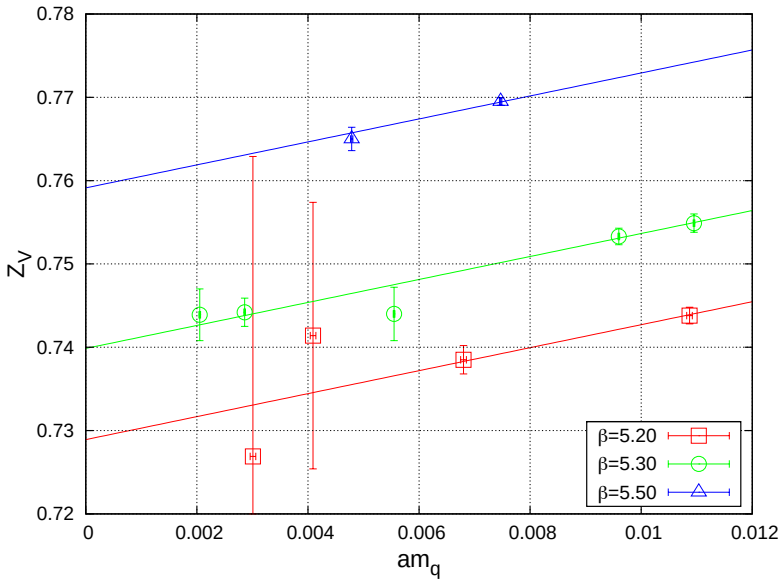

Figure 6.9: Chiral extrapolation of the vector renormalization constant Z_V.

The data are chirally extrapolated with a combined linear fit in am_q to all data points with the fit function

$$Z_V(\beta, m_q) = Z_V(\beta)(1 + b_V). \tag{6.30}$$

It was assumed that the improvement coefficient b_V is β independent. This is not correct but it will be shown later that this is comparable to lattice perturbation results. However, at the current status of the simulations an individual fit to each β would be only possible to $\beta = 5.3$. For $\beta = 5.5$ it would be an interpolation of two points only and the errors are

too large at small quark masses for $\beta = 5.2$. The fit results for Z_V and b_V are summarized in table 6.5.

β	5.2	5.3	5.5
Z_V	0.729(2)	0.740(2)	0.759(1)
b_V	1.87(26)		

Table 6.5: The vector renormalization constant Z_V and the improvement coefficient b_V.

The vector renormalization constant was already calculated by the ALPHA collaboration [32]. They give an interpolation function to compute Z_V for values of $5.2 < \beta < 9.6$

$$Z_V(g_0^2) = \frac{1 - 0.6715 g_0^2 + 0.0388 g_0^4}{1 - 0.5421 g_0^2}, \tag{6.31}$$

where the error is 0.005 for all values of β. The renormalization constant computed from eq. 6.31 is summarized in table 6.6.

β	5.2	5.3	5.5
Z_V	0.739(5)	0.750(5)	0.767(5)

Table 6.6: Vector renormalization constant Z_V from the ALPHA collaboration.

It is not surprising that the values from the ALPHA collaboration and the data presented here do not agree perfectly within errors. First of all the ALPHA collaboration used the so called Schrödinger functional approach [74, 98] which could differ by discretization effects from the here presented analysis. Additionally, the extrapolation with the β independence of b_V may introduce additional systematics.
The improvement constant b_V is only known perturbatively for $N_F = 2$ [99]. The perturbative formula is given by

$$b_V = 1 + 0.11492 \frac{4}{3} g_0^2 + \mathcal{O}(g_0^4) \tag{6.32}$$

where the values are summarized for our β in table 6.7.

β	5.2	5.3	5.5
b_V	1.18	1.17	1.17

Table 6.7: Improvement coefficient b_V from perturbation theory.

One can see that the β dependence of the improvement coefficient from perturbation theory is very mild what supports the assumption of a β independent b_V. However, the perturbative values do not agree with our calculation. A β dependent non-perturbative extraction and a perturbative calculation up to higher order may resolve this issue.
The renormalization constant was computed in the pion form factor calculations here in Mainz [19] as well. The values do agree well with the results from the nucleon form factor but they have roughly a five times smaller error. The higher accuracy comes from the absence of the exponential error growth and hence larger source-sink separations for the pion three-point functions.

6.3.2 Dirac radius $\langle r_1^2 \rangle$

The radii of the nucleon can be calculated by a derivative of the form factor with respect to the momentum transfer. The form factor fits were already discussed in detail in the previous chapter but their functional form will be recapitulated here:

$$G_E(q^2) = \frac{1}{\left(1 + \frac{q^2}{M_E^2}\right)^2}, \qquad G_M(q^2) = \frac{G_M(0)}{\left(1 + \frac{q^2}{M_M^2}\right)^2}. \tag{6.33}$$

From the form factors the radii can be computed via

$$\left\langle r_{E,M}^2 \right\rangle = \frac{6}{G_{E,M}(0)} \left. \frac{\partial G_{E,M}(Q^2)}{\partial Q^2} \right|_{Q=0}. \tag{6.34}$$

Note that the renormalization constant would drop out in this calculation due to the normalization by the form factor at zero momentum transfer. With the explicit form of

the fit functions of eq. 6.33 the radii are directly related to the dipole masses $M_{E/M}$ via

$$\langle r_E^2 \rangle = \frac{12}{M_E^2} \qquad \text{and} \qquad \langle r_M^2 \rangle = \frac{12}{M_M^2}. \tag{6.35}$$

In lattice simulations the Dirac and Pauli form factors are usually used instead of the Sachs form factors. They are directly related to each other via eq. 1.3. The isovector magnetic moment for the Pauli form factor becomes

$$\kappa = G_M(0) - 1 = \mu - 1, \tag{6.36}$$

where the radii can be computed via

$$\frac{1}{M_E^2} = \frac{r_1^2}{12} + \frac{\kappa}{8m_N^2}, \qquad \frac{1}{M_M^2} = \frac{r_1^2 + \kappa r_2^2}{12(1+\kappa)}. \tag{6.37}$$

The magnetic moment is usually measured in units of the nucleon mass. It is useful to normalize the magnetic moment with the nucleon mass computed on the lattice by $\frac{m_N^{\text{lat.}}}{m_N^{\text{phys.}}}$ because the pion mass dependence of the nucleon mass drops out [21].
The data points of the Dirac radius computed on the lattice are shown in figure 6.10 where the black lines indicate the experimental values. A clear trend to the physical value for decreasing pion masses can be seen. Within the statistical errors no deviations in the data for different lattice spacings can be observed.

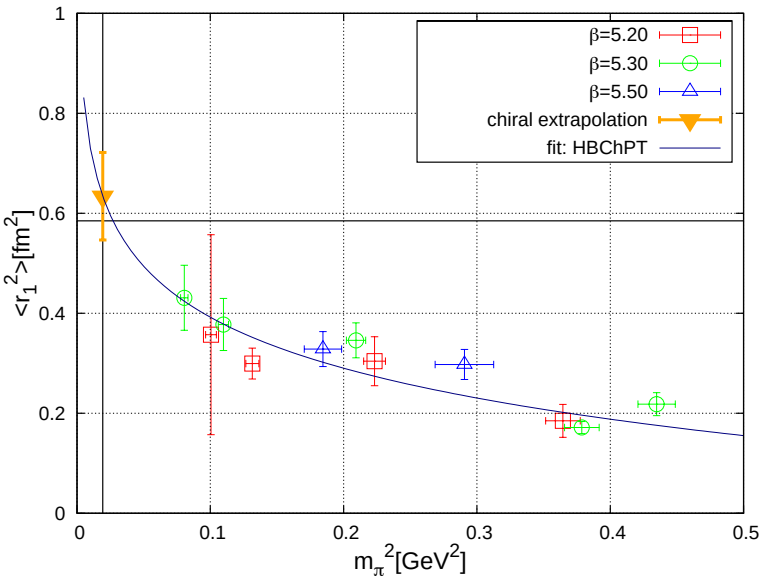

Figure 6.10: The Dirac radius in dependence of the pion mass squared.

These data can be extrapolated to the physical point via a SSE fit [47]

$$\begin{aligned}\langle r_1^2\rangle^{\text{SSE}} &= -\frac{1}{(4\pi f_\pi)^2}\left\{1+7g_A^2+\left(10g_A^2+2\right)\ln\left(\frac{m_\pi}{\lambda}\right)\right\}+\frac{c_A^2}{54\pi^2 f_\pi^2}\Bigg\{26+30\ln\left(\frac{m_\pi}{\lambda}\right)\\ &+ 30\frac{\Delta m_{\Delta N}}{\sqrt{\Delta^2-m_\pi^2}}\ln\left(\frac{\Delta}{m_\pi}+\sqrt{\frac{\Delta^2}{m_\pi^2}-1}\right)\Bigg\}-\frac{12B_{10}^{(r)}(\lambda)}{(4\pi f_\pi)^2}\,,\end{aligned} \tag{6.38}$$

where $f_\pi = 0.092$ GeV is the pion decay constant, $g_A = 1.267$ is the axial charge, $\Delta = 0.2711$ GeV is the mass splitting of the nucleon and the Δ-baryon, and $c_A = 1.5$ GeV is the axial nucleon to Δ-baryon coupling constant. The scale $\lambda = 1$ GeV is absorbed in the low energy constant $B_{10}^{(r)}(\lambda)$. All these parameters are meant to be at the physical point. The fit function of eq. 6.38 is only applicable for pion masses smaller than the mass splitting $\Delta = 0.2711$ GeV but all of our pion masses are larger. This issue can be solved by an analytical continuation of the logarithm and the square root factor. The analytical continuation of the logarithm is given by

$$\arccos(y) = -i\log\left(y+i\sqrt{1-y^2}\right), \tag{6.39}$$

which leads to

$$\frac{1}{\sqrt{\Delta^2-m_\pi^2}}\ln\left(\frac{\Delta}{m_\pi}+\sqrt{\frac{\Delta^2}{m_\pi^2}-1}\right)\rightarrow\frac{1}{\sqrt{m_\pi^2-\Delta^2}}\arccos\left(\frac{\Delta}{m_\pi}\right), \tag{6.40}$$

in combination with the square root. For pion masses smaller than the mass splitting the left part of eq. 6.40 is used, for larger pion masses the right part is used. This kind of analytical continuation is necessary in all following SSE formulae.
Several variations of eq. 6.38 have been used to perform the chiral extrapolation of the Dirac radius. Different combinations of free and fixed parameters have been tried but only one combination gave reasonable χ^2 values and was in good agreement with the data points. The fit function is a modified HBChPT function where c_A is explicitly set to zero which means that no Δ-baryon degrees of freedom are included. It is given by

$$\langle r_1^2\rangle = c_1 + c_2\log\left(m_\pi^2\right) \tag{6.41}$$

with the free fit parameters c_1 and c_2. In addition, a fit was done where the term $(1+c_3 a)$ was multiplied to perform a continuum extrapolation. It turned out that the fit parameter c_3 is statistically compatible with zero. The extrapolated values from both fits do agree

well within their statistical errors. Fits to the data extracted from the local current were also performed to investigate discretization effects further. The values extracted from the local and the conserved currents are almost identical with an deviation much smaller than their statistical error.
The fit function parameters and the extrapolated value are shown in figure 6.10 and the data are summarized in table 6.8.

c_1	c_2	$\langle r_1^{\text{extra.}} \rangle$[fm^2]	$\langle r_1^{\text{exp.}} \rangle$[fm^2] from [10]
0.074(24)	-0.280(39)	0.627(54)	0.585(17)

Table 6.8: Chiral extrapolation of the Dirac radius $\langle r_1^2 \rangle$.

The extrapolated value agrees with the experimental values from [10] and with the PDG value of $0.635(7)$ fm^2 within errors. This is a large improvement compared to previous results from other collaborations [3, 47, 108, 21] where chirally extrapolated value for the Dirac radius was found to be much smaller (≈ 0.35 fm^2). We believe that this improvement comes from the minimization of excited state contributions through the summation method (see chapter 5.2).

6.3.3 Pauli radius $\langle r_2^2 \rangle$ and the anomalous magnetic moment κ

The SSE expression of the Pauli radius is given by [47]

$$\langle r_2^2 \rangle^{\text{SSE}} = \frac{m_N}{\kappa(m_\pi)} \left\{ \frac{g_A^2}{8\pi f_\pi^2 m_\pi} + \frac{c_A^2}{9\pi^2 f_\pi^2 \sqrt{\Delta^2 - m_\pi^2}} \ln\left(\frac{\Delta}{m_\pi} + \sqrt{\frac{\Delta}{m_\pi^2} - 1} \right) + 24 B_{c2} \right\} \quad (6.42)$$

and of the magnetic moment by

$$\begin{aligned} \kappa^{\text{SSE}} &= \kappa^0 - \frac{g_A^2\, m_\pi m_N}{4\pi F_\pi^2} + \frac{2c_A^2 \Delta m_N}{9\pi^2 F_\pi^2} \left\{ \sqrt{1 - \frac{m_\pi^2}{\Delta^2}} \ln\left(\frac{\Delta}{m_\pi} + \sqrt{\frac{\Delta^2}{m_\pi^2} - 1} \right) \right. \\ &+ \left. \ln\left(\frac{m_\pi}{2\Delta} \right) \right\} + \frac{4 c_A c_V g_A m_N m_\pi^2}{9\pi^2 F_\pi^2} \ln\left(\frac{2\Delta}{\lambda} \right) + \frac{4 c_A c_V g_A m_N m_\pi^3}{27\pi F_\pi^2 \Delta} \end{aligned}$$

$$- \quad \frac{8c_A c_V g_A \Delta^2 m_N}{27\pi^2 F_\pi^2}\left\{\left(1-\frac{m_\pi^2}{\Delta^2}\right)^{3/2}\ln\left(\frac{\Delta}{m_\pi}+\sqrt{\frac{\Delta^2}{m_\pi^2}-1}\right)\right.$$
$$+ \quad \left.\left(1-\frac{3m_\pi^2}{2\Delta^2}\right)\ln\left(\frac{m_\pi}{2\Delta}\right)\right\} - 8E_1^{(r)}(\lambda)m_N m_\pi^2. \tag{6.43}$$

An individual fit to the radius is difficult because it depends on κ^{SSE} explicitly. Two different strategies have been used to handle this problem:

- The magnetic moment and the combination $\kappa \cdot \langle r_2^2 \rangle$ have been fitted. In a second step the radius was calculated by dividing $\kappa \cdot \langle r_2^2 \rangle$ by κ at the physical point.

- A combined fit to both quantities was performed.

The combination $\kappa \cdot \langle r_2^2 \rangle$ was fitted independently with the advantage that the implicit pion dependence of κ in eq. 6.42 drops out. After that an individual fit was performed to the magnetic moment with eq. 6.43. A combination of these results at the physical point made it possible to extract the Pauli radius.
The explicit fit function to $\kappa \cdot \langle r_2^2 \rangle$ is

$$\kappa \cdot \langle r_2^2 \rangle = \frac{d_1}{m_\pi} + \frac{d_2}{\sqrt{\Delta^2 - m_\pi^2}}\ln\left(\frac{\Delta}{m_\pi}+\sqrt{\frac{\Delta}{m_\pi^2}-1}\right), \tag{6.44}$$

where Δ has been set to its physical value of 0.2711 GeV, and d_1 and d_2 are free fit parameters. The low energy constant B_{c2} of eq. 6.42 was treated as a free fit parameter but it turned out that it is statistically compatible with zero. To reduce the degrees of freedom of the fits, B_{c2} was set to be zero. The free fit parameters of eq. 6.43 were the isovector nucleon to Δ-baryon coupling constant c_V, a low energy constant of HBChPT $E_1(\lambda)$ and the magnetic moment at the chiral point κ^0. All other parameters were fixed at the values from the previous section.
The fit results to the data computed with the conserved current are shown in the left panel of figure 6.11. The right panel shows the values for κ and the extrapolated values are summarized in table 6.9.

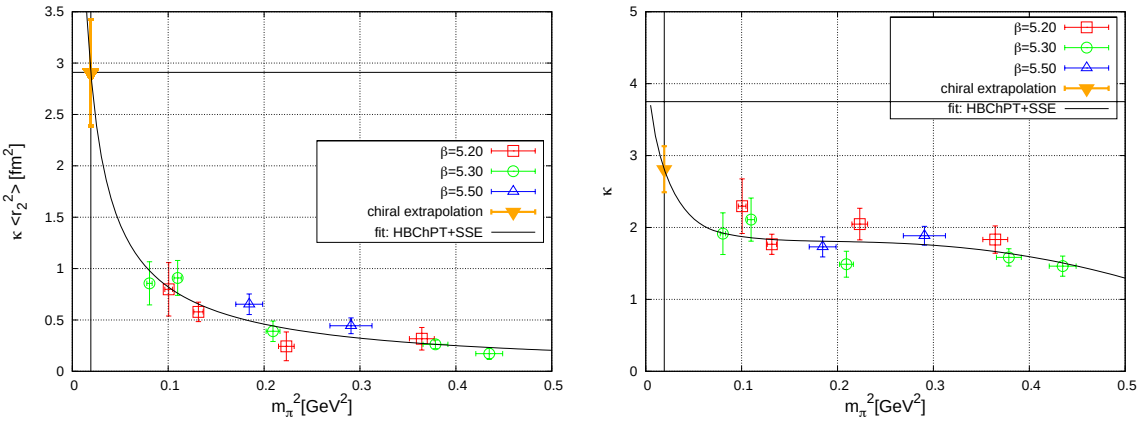

Figure 6.11: Chiral extrapolation of the Pauli radius and the magnetic moment of the nucleon. Shown are data which are extracted from the conserved vector current only.

	conserved	local
$\kappa \cdot \langle r_2^2 \rangle [\text{fm}^2]$	2.91(51)	3.22(66)
κ	2.81(32)	3.41(37)
$\langle r_2^2 \rangle [\text{fm}^2]$	1.04(18)	0.94(19)

Table 6.9: Fit results of $\kappa \cdot \langle r_2^2 \rangle$ and κ. The radius is calculated via $\frac{\kappa \cdot \langle r_2^2 \rangle}{\kappa}$.

Within errors the values for the radius and for $\kappa \cdot \langle r_2^2 \rangle$ extracted from the conserved and local currents agree. The deviation in the magnetic moment computed from the local and the conserved current is not surprising because of the discrepancies in the extrapolation of the ratio $\kappa = 1 - \frac{G_M(q^2)}{G_E(q^2)}$ which was used in the previous chapter. To be able to exclude any further discretization effects the term $(1 + ca)$ was added to the fit functions. The parameter c was statistically compatible with zero and the extrapolated values from both fits agreed within statistical errors.

A simultaneous fit to the radius and the magnetic moment [47] was performed. The fit function is a combination of eq. 6.43 and an adjusted version for the radius:

$$\langle r_2^2 \rangle = \frac{d_1}{m_\pi} + \frac{d_2}{\sqrt{\Delta^2 - m_\pi^2}} \ln\left(\frac{\Delta}{m_\pi} + \sqrt{\frac{\Delta}{m_\pi^2} - 1}\right) \frac{m_N}{\kappa^{\text{SSE}}}. \tag{6.45}$$

The extrapolated values are summarized an table 6.10 and the fits are shown in figure 6.14.

	conserved	local
κ	2.98(29)	3.51(33)
$\langle r_2^2 \rangle [\text{fm}^2]$	0.89(16)	0.90(18)

Table 6.10: Fit results of a conbined fit to $\langle r_2^2 \rangle$ and κ.

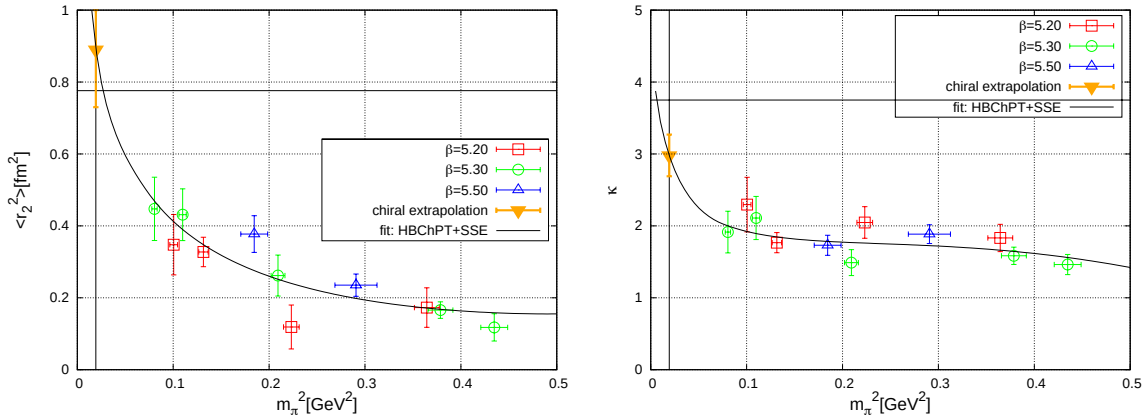

Figure 6.12: Chiral extrapolation of a combined fit to the Pauli radius and the magnetic moment of the nucleon. Shown are only data extracted from the conserved current.

The values extracted from these two different methods are in good agreement to each other. We quote the median of the two fits to the conserved and local data as our best estimate for the radius and the magnetic moment. These are

$$\kappa = 2.98(29)(53) \tag{6.46}$$

$$\langle r_2^2 \rangle = 0.94(19)(10)\ \text{fm}^2 \tag{6.47}$$

The first value in brackets is the statistical error and the second one is the systematic error. The systematic error was estimated from the difference of the median to the farthest point away.

The PDG value for the magnetic moment is $\kappa^{\text{PDG}} \approx 3.701$ and for the Pauli radius $\langle r_2^2 \rangle^{\text{PDG}} = 0.776(11)\ \text{fm}^2$. Our predictions for the radius and the magnetic moment over- and undershoot the experimental values. However, our values agree with the experimental values within errors and with other lattice simulation results [3, 24]. The systematic effect in the magnetic moment is mainly induced by the deviation for the local and con-

served currents. A first look into the $\mathcal{O}(a)$-improvement effects have already been made in chapter 5.4. It turned out that these effects seem to be small and the large deviations cannot be explained. A more precise and complete analysis of the improvement term and maybe a non-perturbative computation of the improvement coefficients for the local and conserved currents is necessary.
A trend to higher values of the magnetic moment for smaller pion masses is hard to see within the range of pion masses shown in figure 6.9. It will be important to perform simulations at smaller pion masses to improve the lattice results for the magnetic moment and the radius.

The fits to the Pauli and Dirac radii and the magnetic moment have been performed with two upper limits of the pion mass. All fits which are shown previously were done with a maximal pion mass of $m_\pi^2 = 0.45\,\text{GeV}^2$, in addition we performed fits with $m_\pi^2 = 0.35\,\text{GeV}^2$. The extrapolated results agree with the presented data within errors but the statistical errors grew dramatically for the smaller pion mass cut-off. For example the value for the Dirac radius is $0.546(122)$ fm^2 instead of $0.585(17)$ fm^2, so the error growth by a factor of seven. This shows again that simulations at smaller pion masses are needed. These simulation would allow shorter extrapolations and will stabilize the fits.

6.3.4 The axial radii $\langle r_A^2 \rangle$ and $\langle r_P^2 \rangle$ and the induced pseudo-scalar coupling constant g_P

The axial radius and the induced pseudo-scalar radius and coupling constant can be derived from the form factor fit in the same way as it was done for the electro-magnetic radii and the magnetic moment. The axial charge will be discussed in the next chapter because it can be computed directly from $G_A(0)$ and hence it is not necessary to derive it from form factor fits. Unfortunately, the statistics for the axial form factors are much worse than for the electro-magnetic ones because of the limitations in the accessible momenta (see chapter 5.3). Therefore, the analysis presented here is only qualitative.
The axial radius is plotted in figure 6.13 as a function of the squared pion mass. The experimental value of $\langle r_A^2 \rangle \approx 0.38$ fm^2 is from [11]. In contrast to other lattice results (see e.g [83]) which stay constant and much below the experimental value or decrease with small pion mass our data show a trend towards the experimental value. This is the result of using the summation method and hence the decreased influence of excited state con-

tributions.
The predicted chiral behavior from HBChPT with SSE of the axial radius is given by [12]

$$\langle r_A^2 \rangle^{\text{SSE}} = \frac{\tilde{B}_3}{g_A} \frac{6}{(4\pi F_\pi)^2} \tag{6.48}$$

where $\tilde{B}_3$ is a low energy constant. As already mentioned our lattice data are much below the experimental value but show a clear trend. However, the chiral formula of eq. 6.48 cannot be used for a serious chiral extrapolation because it is just a constant in the pion mass and thus cannot reproduce the slope of the data.

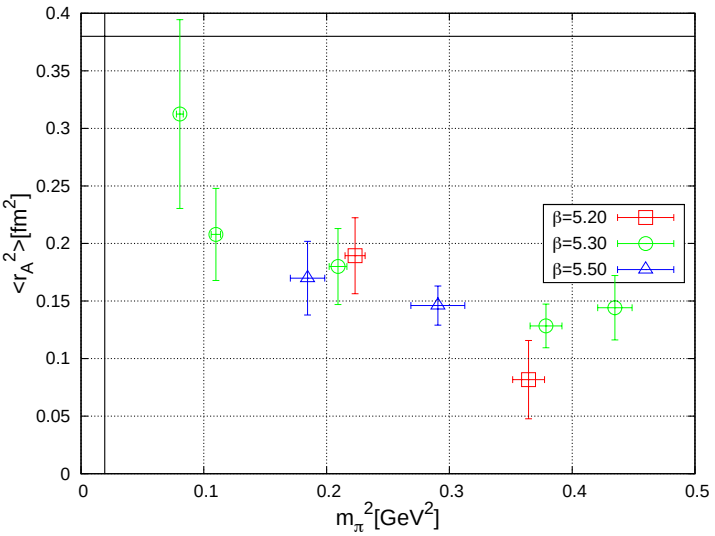

Figure 6.13: The axial radius $\langle r_A^2 \rangle$.

Our data for the induced pseudo-scalar quantities are shown in figure 6.13. The fit functions plotted are motivated by HBChPT with SSE [12]

$$\langle r_P^2 \rangle^{\text{SSE}} = \frac{c_1}{(c_2 - m_\pi^2) m_\pi^2} \tag{6.49}$$

and

$$G_P(0) = c_2 + \frac{c_3}{m_\pi^2}, \tag{6.50}$$

where c_1, c_2 and c_3 are free fit parameters. One can see that these fits reproduce our data points very well and the extrapolated values are $\langle r_P^2 \rangle = 7.9(8)$ and $G_P(0) = 55(12)$. The induced pseudo-scalar coupling constant is not defined at zero momentum transfer but

at 0.88 times the muon mass. The experimental value of g_P is $8.26(16)$ [11].

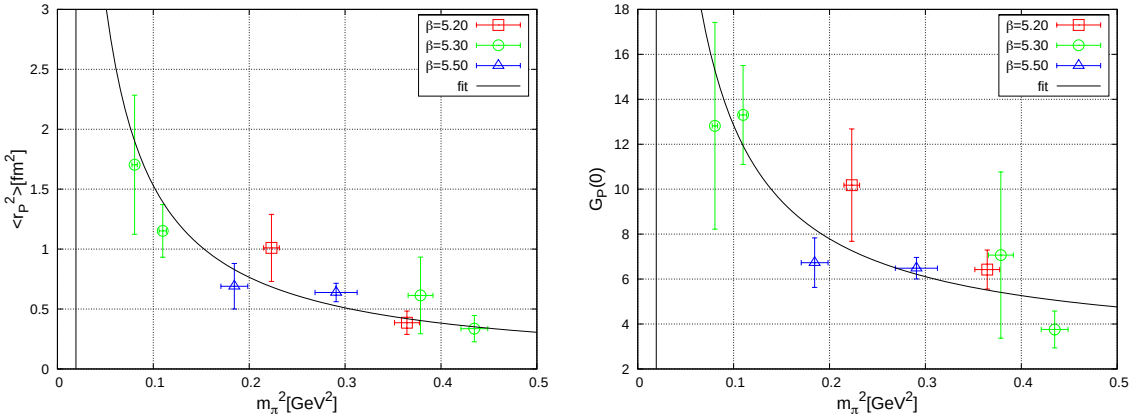

Figure 6.14: The induced pseudo-scalar radius $\langle r_P^2 \rangle$ and form factor at zero momentum transfer $G_P(0)$.

The momentum transfer of $q^2 = 0.88 m_\mu^2 \approx 0.01\text{GeV}^2$ is rather small and our extrapolated value overshoots it by far. It could be that discretization or volume effects are large and that the value would go down in the continuum and infinite volume limit. This can be investigated only if more data points are available. Only four different momentum values have been used to perform the form factor fits and the data are also very noisy. In addition, it was not possible to fit the form factors on some ensembles (E5, A3-5) because the statistical error was larger than 100%. The only way to get reasonable data for the induced pseudo-scalar quantities would be another choice of the polarization matrix where $G_A(q^2)$ and $G_P(q^2)$ are disentangled from the beginning (see e.g. [5]). This would require a new set of simulations on all ensembles.

6.3.5 Axial charge g_A

The data for the axial charge are extracted from the third component of the axial current with the summation method. Of course, the axial charge has to be renormalized. The $\mathcal{O}(a)$-improved renormalization constant Z_A was already used in the quark mass determination. It is defined in eq. 6.2 and was determined in [33]. The improvement coefficient b_A is defined in eq. 6.4. An $\mathcal{O}(a)$-improvement of the axial charge itself is not

necessary because it is determined at zero momentum transfer where the improvement term vanish for spatial components (see eq. 6.6).
The SSE expression for the axial charge in the continuum (indicated by ∞) is given by [58]

$$\begin{aligned} g_A^{SSE}(\infty) &= g_A^0 - \frac{(g_A^0)^3 m_\pi^2}{16\pi^2 F_\pi^2} + 4\left\{ C^{SSE}(\lambda) + \frac{c_A^2}{4\pi^2 F_\pi^2}\left[\frac{155}{972}\, g_1 - \frac{17}{36}\, g_A^0\right] + \gamma^{SSE} \ln\frac{m_\pi}{\lambda}\right\} m_\pi^2 \\ &\quad + \frac{4c_A^2 g_A^0}{27\pi F_\pi^2 \Delta} m_\pi^3 + \frac{8}{27\pi^2 F_\pi^2}\, c_A^2 g_A^0 m_\pi^2 \sqrt{1-\frac{m_\pi^2}{\Delta^2}}\, \ln R \\ &\quad + \frac{c_A^2 \Delta^2}{81\pi^2 F_\pi^2}\left(25 g_1 - 57 g_A^0\right)\left\{ \ln\left[\frac{2\Delta}{m_\pi}\right] - \sqrt{1-\frac{m_\pi^2}{\Delta^2}}\, \ln R\right\} + \mathcal{O}(\epsilon^4) \end{aligned} \tag{6.51}$$

where g_1 is the $\Delta\Delta$-baryon coupling constant. The scale-dependent low-energy constant $C^{SSE}(\lambda)$ is a linear combination of the low energy constants $B_9(\lambda)$ and $B_{20}(\lambda)$, and g_A^0 is the axial charge in the chiral limit. The factors γ^{SSE} and R are defined as

$$\begin{aligned} \gamma^{SSE} &= \frac{1}{16\pi^2 F_\pi^2}\left[\frac{50}{81}\, c_A^2 g_1 - \frac{1}{2}\, g_A^0 - \frac{2}{9}\, c_A^2 g_A^0 - (g_A^0)^3\right] \\ R &= \frac{\Delta_0}{m_\pi} + \sqrt{\frac{\Delta_0^2}{m_\pi^2} - 1}. \end{aligned} \tag{6.52}$$

The HBChPT results without the Δ-baryon degrees of freedom can be obtained by setting $c_A = 0$. For eq. 6.51 a volume correction exists. The SSE expression of the axial charge defined in a box of length L is given by

$$g_A(L) = g_A(\infty) + \Delta g_A(L). \tag{6.53}$$

where the infinite volume part $g_A(\infty)$ is eq. 6.51. The volume corrections $\Delta g_A(L)$ can be computed via [8]

$$
\begin{aligned}
\Delta g_A(L) \;=\; & -\frac{g_A^0 m_\pi^2}{4\pi^2 F_\pi^2}\sum_{\vec{n}}\frac{K_1(L|\vec{n}|m_\pi)}{L|\vec{n}|m_\pi} \\
& +\frac{(g_A^0)^2 m_\pi^2}{6\pi^2 F_\pi^2}\sum_{\vec{n}}\left[K_0(L|\vec{n}|m_\pi)-\frac{K_1(L|\vec{n}|m_\pi)}{L|\vec{n}|m_\pi}\right] \\
& +\frac{25c_A^2 g_1}{81\pi^2 F_\pi^2}\int_0^\infty \mathrm{d}y\, y\sum_{\vec{n}}\left[K_0(L|\vec{n}|f(m_\pi,y))-\frac{L|\vec{n}|f(m_\pi,y)}{3}K_1(L|\vec{n}|f(m_\pi,y))\right] \\
& -\frac{c_A^2 g_A^0}{\pi^2 F_\pi^2}\int_0^\infty \mathrm{d}y\, y\sum_{\vec{n}}\left[K_0(L|\vec{n}|f(m_\pi,y))-\frac{L|\vec{n}|f(m_\pi,y)}{3}K_1(L|\vec{n}|f(m_\pi,y))\right] \\
& +\frac{8c_A^2 g_A^0}{27\pi^2 F_\pi^2}\int_0^\infty \mathrm{d}y\sum_{\vec{n}}\left[K_0(L|\vec{n}|f(m_\pi,y))-\frac{K_1(L|\vec{n}|f(m_\pi,y))}{L|\vec{n}|f(m_\pi,y)}\right] \\
& -\frac{4c_A^2 g_A^0}{27\pi F_\pi^2}\frac{m_\pi^3}{\Delta_0}\sum_{\vec{n}}\frac{1}{L|\vec{n}|m_\pi}e^{-L|\vec{n}|m_\pi}+\mathcal{O}(\epsilon^4)
\end{aligned}
\tag{6.54}
$$

where the contribution of $|\vec{n}| = 0$ are omitted in the sums. The functions K_0 and K_1 are modified Bessel functions and the function $f(m_\pi, y)$ is defined as

$$f(m_\pi, y) = \sqrt{m_\pi^2 + y^2 + 2y\Delta}. \tag{6.55}$$

Five different types of fits in m_π^2 have been performed. The simplest ones were a constant and a linear fit in m_π^2. We used as well the HBChPT form of eq. 6.51 with $\lambda = 1.0\,\mathrm{GeV}$ and where f_π was fixed at its experimental value. The free parameters in the SSE fit without the volume correction were g_A^0, $C^{SSE}(\lambda)$ and g_1. All other parameters have been fixed to their physical values. Other combinations of free parameters have been tried as well but only the afore-mentioned fit was stable and gave a reasonable χ^2.

The volume correction was used in earlier analysis as well but in a slightly different manner [5]. In this publication the experimental values of all parameters have been used to correct the finite volume effects for each value of $m_\pi L$ with eq. 6.54. We used a different approach. Instead of correcting each point separately we used eq. 6.53 as our fit function where the same fit parameters as without the finite volume correction have been used. This has the advantage that we are independent of the experimental values of the three fit parameters, especially of the axial charge in the chiral limit.

All five fit functions have been used for a chiral extrapolation. The axial charge and the different fit results are plotted in figure 6.15. The black lines indicate the experimental

values. One can see that a lot of our lattice data points touch the experimental value for g_A especially at small pion masses. This is a vast improvement compared to previous lattice determinations (see e.g. fig 1.2) where the lattice data are much below the experimental value or even decrease at small pion masses.
The fit results for fits to all accessible pion masses and for pion masses smaller than $m_\pi^2 < 0.35\ \text{GeV}^2$ only are shown in figure 6.16. One can see that the HBChPT fit without the Δ-baryon degrees of freedom cannot reproduce the experimental value and the fit does not agree with the data points at small pion masses. It is somewhat surprising that all other extrapolated values agree so well especially when the points of all pion masses were included. That the errors of the constant fit and the linear fit are smaller than for the SSE fit is clear because the number of degrees of freedom is smaller. Nevertheless, the χ^2-values are around 0.5 for the uncorrelated and correlated fits (except for the HBChPT fit) which is acceptable. The volume correction of the SSE fit drives the extrapolated value slightly upwards but the deviation is very small and hence, volume effects should be small.

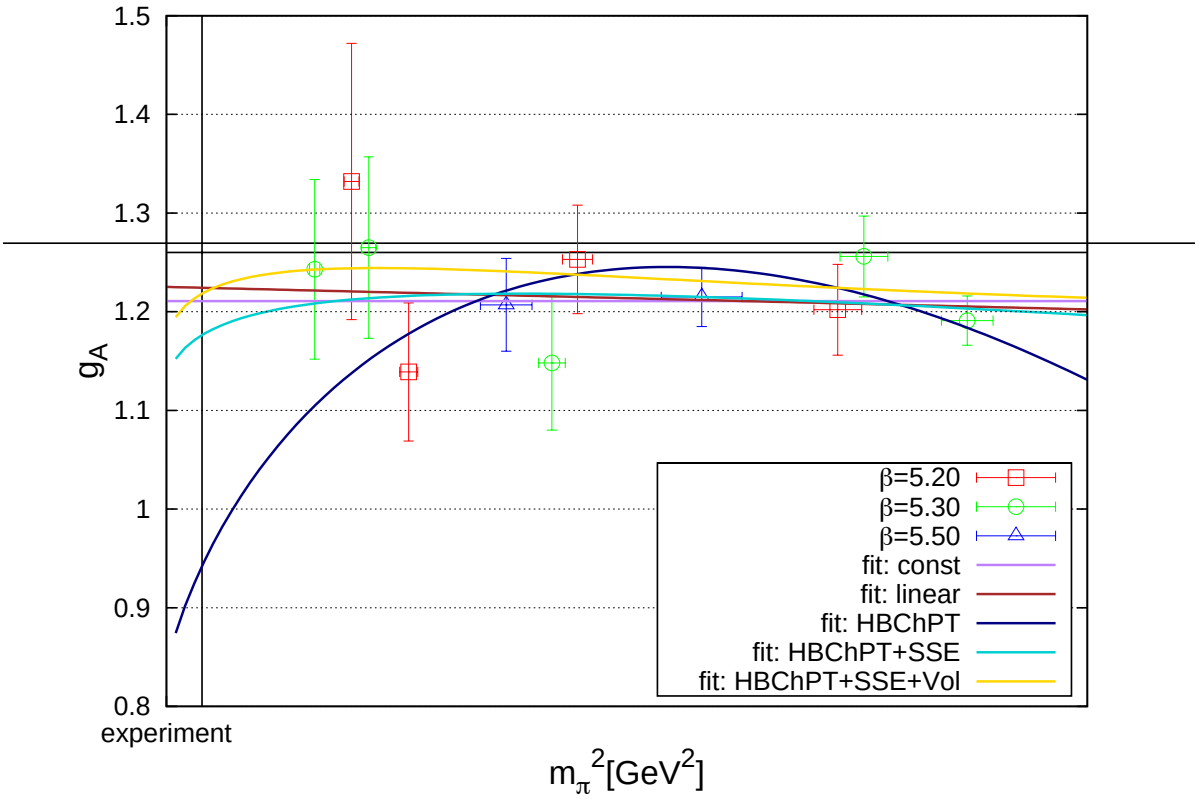

Figure 6.15: Fits to the axial charge for all accessible pion masses.

The cut-off in the pion masses has no effect on the constant and linear fit except that the statistical error grows. In the case of the SSE fits the extrapolated values increase but they are still compatible with the experimental value and the other fit results. This may come from the two relatively low points at pion masses of $m_\pi^2 \approx 0.21\,\text{GeV}^2$ and $m_\pi^2 \approx 0.12\,\text{GeV}^2$ which lead to a much steeper curve and thus to higher values for g_A.
Discretization effects have been investigated for all fits. As in the case of the electromagnetic quantities the term $1 + ca$ was multiplied to the fit function. The value for the new fit parameter c was in all cases compatible with zero and the continuum extrapolated and chirally extrapolated value agreed perfectly with the fits without the discretization term. The only effect was a growth of the statistical error by a factor of two roughly. It follows that discretization effects are small for the data presented here.

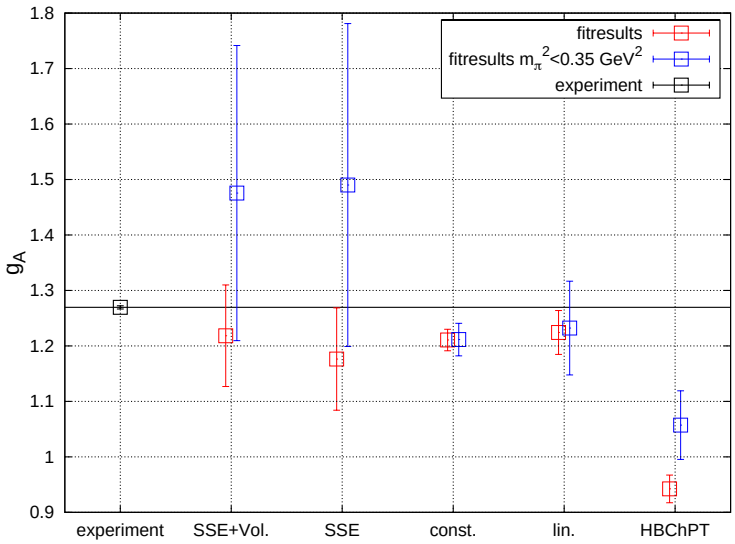

Figure 6.16: Results of the fits to the axial charge. Shown are the results to fits to all data and for data with $m_\pi < 0.35\,\text{GeV}^2$.

All in all it is difficult to present a systematic error on the axial charge. The only deviations in all different kinds of fitting procedures are from the HBChPT fits (which does not work obviously) and the SSE fits which are computed at pion masses of $m_\pi^2 < 0.35\,\text{GeV}^2$. However, the errors of these SSE fits are roughly a factor of three larger than the errors of the fits including the point at heavier pion masses and hence they are not used for an estimate of the systematic error.
We quote $g_A = 1.218(92)$ as our best estimate for the axial charge which is extracted from the SSE fit with the volume corrections without the cut in the maximal pion mass. The ex-

tracted value is in a very good agreement with the experimental value of $g_A = 1.2695(29)$ (PDG). This was achieved by using the summation method to reduce excited state contributions. All other systematic effects seem to be very small, which is in agreement with the observations of other lattice calculations. However, all other lattice calculations have failed so far to reproduce the experimental value. Their results deviate two standard deviations [5, 21, 83, 107] from the experimental value at least or the quoted errors are much larger as ours. Unfortunately, our quoted error is roughly a factor 30 larger than the experimental error. This will be improved in further simulations at smaller pion masses. In addition it is still possible to expand the current simulation with more statistics. For some ensembles not all configurations have been used and the usage of more source positions with other polarization matrices is always possible.

Chapter 7

Summary and future work

In this work, the lattice spacing was computed which was used to compare dimensionful lattice results with their experimental counterparts. This has been done by using the Ω-baryon mass and the results have been compared to complementary calculations on the same ensembles. These data are in very good agreement to each other.
Hadron masses have been computed as well and were chirally extrapolated to the physical point. Discretization effects have been investigated and they cannot be neglected in the case of the Kaon. The vector mesons ρ and K^* have been computed but the effects of the width have been ignored. Large deviation from their experimental values appeared. The nucleon and Δ-baryon masses are in agreement with experimental values within their errors.
The light and the strange quark masses have been calculated. They were found to be in agreement with experiments and determinations from other lattice groups.
The iso-vector electro-magnetic and axial form factors of the nucleon have been calculated on a set of gauge ensembles with different pion masses, volumes and lattice spacings with the result that discretization effects and volume effects seem to be small. The chiral extrapolation is crucial because the fit ansatz predicted by HBChPT (with or without SSE) have to treated with caution. These functions are derived for small pion masses and it is not a priori clear what the maximal pion mass of their applicability is.
Excited state contributions to the nucleon matrix elements have been investigated carefully. It turned out that they cannot be neglected for baryonic matrix elements. It was possible to achieve results from the lattice which agree with the experimental data within

their errors. This is a huge improvement compared to all other previous lattice simulations of these quantities.

Four new lattices are in the production pipeline, B6, G8, N6 and O7 which have pion masses between 200 and 300 MeV. These four lattices will improve the calculation of the lattice spacing. This will be very helpful because the error of a is relatively large with $1-3\%$ currently. A smaller error on the lattice spacing would lead to smaller errors on all dimensionful quantities. The quark and hadron mass determination will also be improved by these lattices because of the much shorter chiral extrapolation.
The computation of form factors will benefit from these four new lattices as well. Especially the magnetic moment of the nucleon shows no trend in the pion mass down to values of around 300 MeV and is much smaller than the experimental value. Due to computation on the new ensembles an upwards trend to the physical value will hopefully be seen. The chiral extrapolation will become shorter and values computed at higher quark masses can be sorted out. This was not possible at the moment because the error of the extrapolated quantities increase extremely when values from the largest quark masses were left out.
It is difficult to investigate volume effects systematically at the given sets of ensembles and in fact it was done for the axial charge only with the help of chiral perturbation theory. Although a large set of ensembles exist with different volumes, none of them have the same pion mass and lattice spacing. It will be important to create an ensemble in the future, preferably at a pion mass below 300 MeV. This will allow a systematic investigation of the volume dependence of each quantity separately without the help of ChPT.

The $\mathcal{O}(a)$-improvement of baryonic matrix elements was only touched. It will be necessary to include the spatial derivative of the tensor current to get the full improvement term. In addition a non-perturbative computation of the improvement coefficient c_V for the local and the conserved current would be helpful. It was shown for the improvement coefficient b_V that the deviation between the non-perturbative and perturbative calculation can be large. The computations of c_V and the full improvement term could help to understand the difference in the magnetic moment of the nucleon computed form the ratio $G_M(q^2)/G_E(q^2)$.
The current version of the code provides a good starting point for further investigations of baryons. One could think about the computation of nucleon to Δ transitions which gives informations about the shape of the Δ. The Δ form factors are of interest as well.

The Generalized Parton Distributions (GPDs) of the nucleon have not been mentioned yet. It will be the next important task to implement them in the current program and to compute them. This is important because GPDs provide informations about the quarks in the nucleon in terms of their longitudinal momentum fraction and their transverse spatial distribution, and give access to the angular momentum decomposition of the nucleon. As for the axial form factor and the Dirac radius, some of the experimental values cannot be reproduced by current lattice computations. Hence, careful investigations of the systematic effects especially of the excited state contributions will be mandatory and may lead to better agreement of lattice results and experimental values.

Appendix A

Lattice set-up

ID	β/a/c_{SW}	κ_c /κ_s	$T \cdot L^3$	κ_{sea}	m_π [GeV]	$m_\pi L$
A2	5.2/ 0.079(1)fm/ 2.01715	0.136051(2)/ 0.135041(32)	$64x32^3$	0.13565	0.604(11)	7.7
A3				0.13580	0.472(9)	6.0
A4				0.13590	0.363(7)	4.7
A5				0.13594	0.317(6)	4.0
B6			$96x48^3$	0.13597	≈0.270	≈ 5.2
E3	5.3/ 0.062(1)fm/ 1.90952	0.136456(1)/ 0.135730(20)	$64x32^3$	0.13605	0.659(11)	6.6
E4				0.13610	0.615(10)	6.2
E5				0.13625	0.458(8)	4.7
F6			$96x48^3$	0.13635	0.331(6)	5.0
F7				0.13637	0.284(5)	4.2
G8			$128x64^3$	0.136417	≈0.200	≈4.0
N3	5.5/ 0.050(2)fm/ 1.7515	0.136779(1)/ 0.136179(34)	$96x48^3$	0.13640	0.629(23)	7.7
N4				0.13650	0.539(20)	6.5
N5				0.13660	0.430(16)	5.2
N6				0.13667	≈0.330	≈4.0
O7			$128x64^3$	0.13671	≈0.260	≈4.2

Table A.1: Overview of the lattice ensembles. The lattices B6, G8, N6 and O7 are still under construction and will be used in later analysis. The estimates for the pion mass and $m_\pi L$ on these lattices are computed by chiral extrapolations of the pion mass in $1/\kappa_{\mathrm{sed}}$ (see chapter 6.1) and with the determined scale (see chapter 4). Values with errors have been computed in this thesis.

ID	# configs.	# src. Pos.	# polarizations	smearing	smearing parms
A3	265	4	1	J+HYP	N=300, α=0.2
A4	371				
A5	201				
E3	155	4	1	J+HYP	N=300, α=0.2
E4	162				
E5	168				
F6	192				
F7	250				
N3	148	4	2	G+HYP	N=175, α=2.9
N4	141				
N5	239				

Table A.2: Overview of the lattice ensembles used in the scale determination and the hadron mass computation. The second column shows the number of configurations used. The third one shows the number of source positions where the sources are maximally separated. More than one polarization matrix for baryons was used on the N-lattice only because these are computations with the latest version of the code where this feature was accessible. This is the reason why the smearing is different for the N lattice as well. Jacobi source [54] smearing was used in the old simulations, Gaussian smearing [27] was used in the latest ones. In all cases HYP smeared links [57] with the parameters $\alpha_1 = 0.75$, $\alpha_2 = 0.6$ and $\alpha_3 = 0.3$ were used. The smearing is tuned in a way that the radius of the source is $r \approx 0.4$ fm which gives the best results.

ID	# configs.	# src. Pos.	# polarizations	smearing	smearing parms
A2	144	4	1	G+HYP	N=110, α=0.2
A3	265				
A4	199	8			
A5	212				
E3	139	4	1	G+HYP	N=140, α=0.2
E4	162	4+4	2		
E5	168				
F6	199	4	1		
F7	250				
N4	150	4	1	G+HYP	N=100,α=2.9
N5	150				

Table A.3: Overview of the lattice ensembles used in the form factor simulations. The columns are the same as in table A.2. In the symmetry column $4 + 4$ means that eight source positions were used but 4 with another polarization matrix as for the other four. The smearing was applied to the source and to the sink.

Appendix B

Chiral representation of Dirac matrices

In our measurement code the chiral representation of the Dirac matrices is used. In Euclidean space time, these matrices are defined as:

$$\gamma_0 = \begin{pmatrix} 0 & 0 & -1 & 0 \\ 0 & 0 & 0 & -1 \\ -1 & 0 & 0 & 0 \\ 0 & -1 & 0 & 0 \end{pmatrix}, \tag{B.1}$$

$$\gamma_1 = \begin{pmatrix} 0 & 0 & 0 & -i \\ 0 & 0 & -i & 0 \\ 0 & i & 0 & 0 \\ i & 0 & 0 & 0 \end{pmatrix}, \tag{B.2}$$

$$\gamma_2 = \begin{pmatrix} 0 & 0 & 0 & -1 \\ 0 & 0 & 1 & 0 \\ 0 & 1 & 0 & 0 \\ -1 & 0 & 0 & 0 \end{pmatrix}, \tag{B.3}$$

$$\gamma_3 = \begin{pmatrix} 0 & 0 & -i & 0 \\ 0 & 0 & 0 & i \\ i & 0 & 0 & 0 \\ 0 & -i & 0 & 0 \end{pmatrix}, \tag{B.4}$$

$$\gamma_5 = \gamma_0\gamma_1\gamma_2\gamma_3 = \begin{pmatrix} 1 & 0 & 0 & 0 \\ 0 & 1 & 0 & 0 \\ 0 & 0 & -1 & 0 \\ 0 & 0 & 0 & -1 \end{pmatrix}. \tag{B.5}$$

With this definition of the Dirac matrices the polarization matrices of eq. 3.49-3.52 can be written as:

$$\Gamma = \tfrac{1}{2}(1+\gamma_0)\tfrac{1}{2}(1-i\gamma_3\gamma 5) = \begin{pmatrix} 0 & 0 & 0 & 0 \\ 0 & \frac{1}{2} & 0 & -\frac{1}{2} \\ 0 & 0 & 0 & 0 \\ 0 & -\frac{1}{2} & 0 & \frac{1}{2} \end{pmatrix}, \tag{B.6}$$

$$\Gamma^{\mathcal{T}} = \gamma_5\gamma_0\Gamma\gamma_0\gamma_5 = \tfrac{1}{2}(1-\gamma_0)\tfrac{1}{2}(1+i\gamma_3\gamma 5) = \begin{pmatrix} 0 & 0 & 0 & 0 \\ 0 & \frac{1}{2} & 0 & \frac{1}{2} \\ 0 & 0 & 0 & 0 \\ 0 & \frac{1}{2} & 0 & \frac{1}{2} \end{pmatrix}, \tag{B.7}$$

$$\Gamma^{\mathcal{C}} = C^{-1}\Gamma C = \tfrac{1}{2}(1-\gamma_0)\tfrac{1}{2}(1-i\gamma_3\gamma 5) = \begin{pmatrix} \frac{1}{2} & 0 & \frac{1}{2} & 0 \\ 0 & 0 & 0 & 0 \\ \frac{1}{2} & 0 & \frac{1}{2} & 0 \\ 0 & 0 & 0 & 0 \end{pmatrix}, \tag{B.8}$$

$$\Gamma^{\mathcal{TC}} = \gamma_5\gamma_0 C^{-1}\Gamma C\gamma_0\gamma_5 = \tfrac{1}{2}(1+\gamma_0)\tfrac{1}{2}(1+i\gamma_3\gamma 5) = \begin{pmatrix} \frac{1}{2} & 0 & -\frac{1}{2} & 0 \\ 0 & 0 & 0 & 0 \\ -\frac{1}{2} & 0 & \frac{1}{2} & 0 \\ 0 & 0 & 0 & 0 \end{pmatrix}. \tag{B.9}$$

Appendix C

Smearing

C.1 Source and sink smearing

The choice of the source for the inversion is crucial and depends on the observables of interest. To invert the Dirac operator $D(x,z)$ one needs to solve the linear equation

$$\sum_{z,b,\beta} D(x,z)^{ab}_{\alpha\beta} S(z,y)^{bc}_{\beta\gamma} = \eta(x,y)^{ac}_{\alpha\gamma} \tag{C.1}$$

where $S(z,y)$ is the quark propagator from point z to all other points y and $\eta(x,y)$ is the source. To get the full quark propagator 12 inversions are needed, four for the Dirac components and three for the color components. The source η can be tuned in a way that it is the optimal choice for the problem of interest.
The naive (point) source is a delta function in spatial, dirac and color components

$$\eta(x,y)^{ac}_{\alpha\gamma} = \delta_{x,y}\delta_{a,c}\delta_{\alpha\gamma}. \tag{C.2}$$

This source can be used in cases where no exponential error growth exists and where the contamination from exciterd states are small, e.g. for the pion. The point source is always a good cross check for other types of sources. The effective mass of a particle computed with any type of source must be equal to the effective mass computed with a point source. Other source types e.g. which are used for mesons or disconnected contributions are

stochastic volume sources which can be beneficial for statistics and computanional costs [18].
For baryons the contaminations from excited states are large and it would be beneficial to construct a source which suppresses them. Several choices are possible. The Wuppertal smearing [54] is an exact solution of the equation

$$(1 - \alpha H)\Phi = \eta \tag{C.3}$$

where H is the spatial part of the hopping term of the Dirac operator and α is a tunable parameter. The source is not smeared in Euclidean time. In eq. C.3 all indices are suppressed. This equation is solved by an inversion which leads to the smeared Wuppertal source Φ but this inversion is expensive. The solution can be approximated with the so called Jacobi smearing

$$\Phi = \sum_{k=0}^{N} (\alpha H)^k \eta, \tag{C.4}$$

which is an iterative procedure to solve eq. C.3 iteratively where the operator H acts on the pointsource η. In addition to the Wuppertal smearing the additional tuning parameter N appears, the number of jacobi iterations.
The Jacobi source can be computed by a for-loop with N iterations. To see how the series can be implemented the first steps can be written down:

N	
0	η
1	$(1 + \alpha H)\eta$
2	$\eta + \alpha H\left[(1 + \alpha H)\eta\right]$

Table C.1: The first steps of the Jacobi series.

This leads directly to the iterative formula for the Jacobi smearing

$$a_n = \alpha H a_{n-1} + a_0, \qquad \text{with} \quad a_0 = \eta. \tag{C.5}$$

Another way of an iterative smearing procedure is the so called Gaussian smearing [27] which is similar to the Jacobi smearing. The Gaussian source is defined as

$$\Phi = (1 + \alpha H)^N \eta. \tag{C.6}$$

The first steps of the series are:

N	
0	η
1	$(1+\alpha H)\eta$
2	$(1+\alpha H)\eta + \alpha H\left[(1+\alpha H)\eta\right]$

Table C.2: The first steps of the Gaussian series.

which leads to the series formula

$$a_n = (1+\alpha H)a_{n-1}, \qquad \text{with} \quad a_0 = \eta. \tag{C.7}$$

We used only the Jacobi and the gaussian sources in our simulations because the construction of the Wuppertal source is to expensive.
The difference between the Jacobi and the Gaussian source is that the Gaussian source is much easier to normalize. It is clear that an iterative procedure increases the norm of the source which should be around one. If the norm of the source becomes to large the inversion may fail because of rounding and precision errors. After a few hundred iterations some entries can be larger than 10^{300}.
To normalize the Jacobi source one would need a norm of the operator H which is expensive to compute. In contrast, the gaussian smeared source can be easily normalized by multiplying it by $(1+6\alpha)^{-1}$ in each iteration. This is important for the computation of three-point functions when the smearing is also applied to the sink.
The sink smearing is applied in the same way as the source smearing. Instead of the point source an already created quark propagator is used. This is more expensive in computer time because the smearing routine must be applied on all time slices. The sink smearing of the three-point functions is more involved [36]. The extended source defined in eq. 3.28 must be constructed of source and sink smeared quark propagators and the extended source must be smeared as well.
The effectiveness of the source smearing can be increased when the links in the operator H are smeared as well. Two different ways of link smearing are implemented, the so called APE [1] and the hypercubic (HYP) [57] smearing.
The basic idea of link smearing is that two lattice points can be connected by staples. An example is shown in figure C.1 where the original link $U_\nu(x)$ is smeared by the three other links.

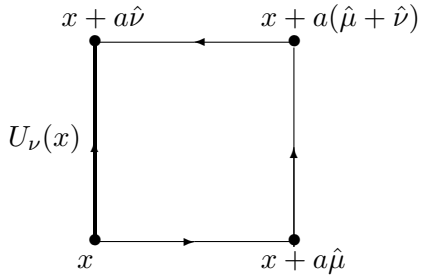

The APE smearing procedure uses only staples to smear the original links. A sum over all staples for one link is build and multiplied by a factor. This staple is added to the original link. After the summations the new fat links must be projected to $SU(3)$. The HYP smearing procedure uses all links in a hyper-cube which are surrounding the original link. This is done in three steps where each step is an application of one APE smearing.

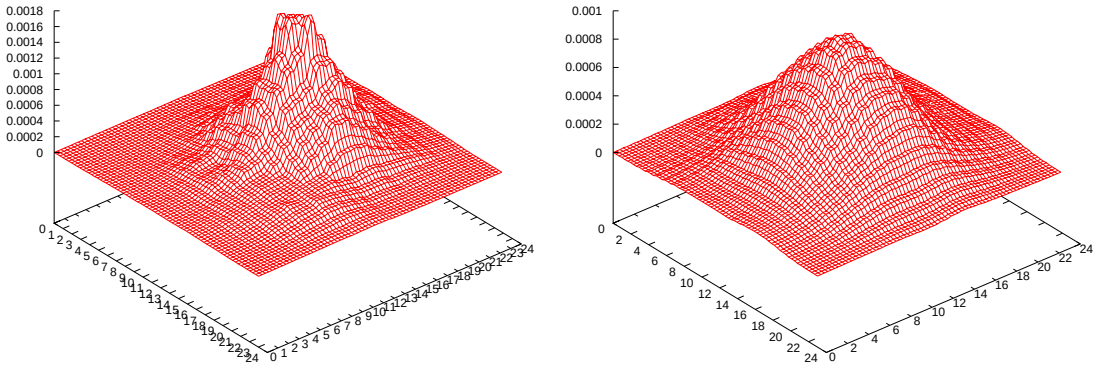

Figure C.1: Jacobi smeared sources. The left picture shows a source with unsmeared links and the right picture one with HYP smeared links. The parameters were $N = 200$ and $\alpha = 0.2$ for both sources.

C.2 Numerical tests

Two examples of a smeared source are shown in figure C.1. These are Jacobi sources created with the parameters $N = 200$ and $\alpha = 0.2$. Plotted is the Frobenius norm of the source on the x-y-plane at $z = 0$. One can see that the additional HYP smearing (shown in the right panel) smoothes the source which gives usually a better signal-to-noise ratio.

The effectiveness of the smearing is shown in figure C.2. Plotted is the effective mass of the nucleon on the N5 ensemble.

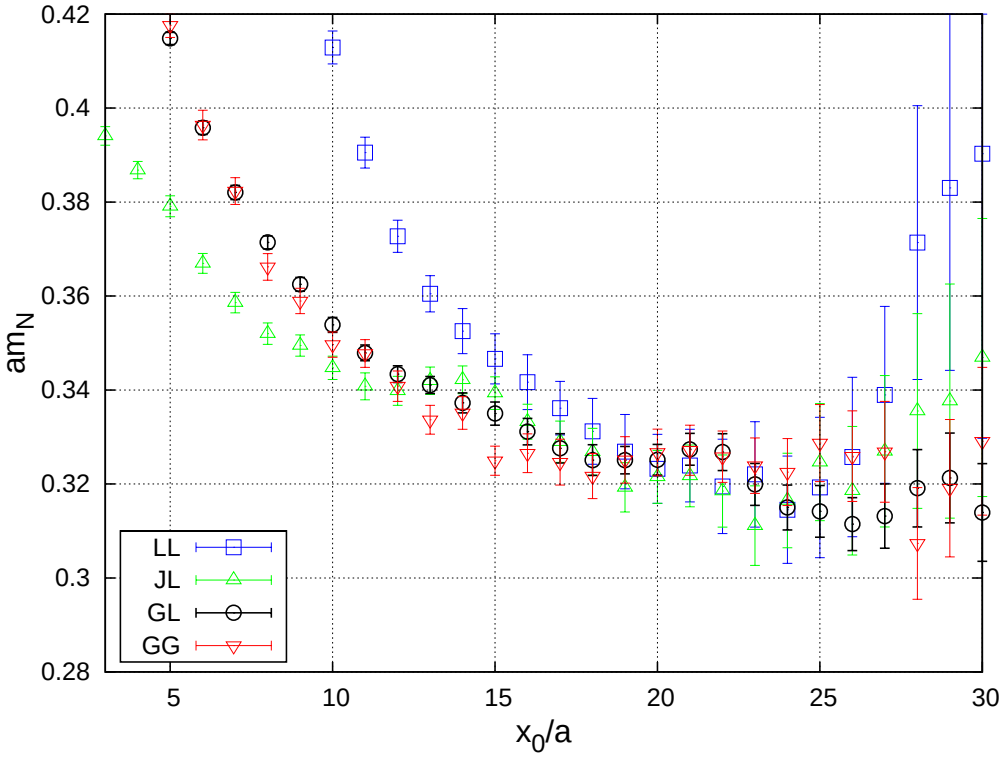

Figure C.2: Effectiveness of different smearing procedures for the nucleon effective mass. The label LL means that the quark propagators are created with a local and unsmeared source and sink, GL and JL with a Gaussian/Jacobi smeared source and a local sink and GG means with a Gaussian smeared source and sink.

The parameter to create these source were $N = 100$ and $\alpha = 2.0$ in the case of the Gaussian smearing and $N = 300$ and $\alpha = 0.2$ in the case of the Jacobi smearing. It can be seen that the excited state contributions are decreased compared to the point source for all smearings. In addition the signal-to-noise ratio is much better for the effective masses which were created with smearing. The effective mass of the unsmeared nucleon starts to increase around $28a$ in Euclidean time while it remains almost constant for the smearing procedures. The signal-to-noise ratio is best for the gaussian source with the local sink hence this is the reason why it was used in the latest computations of the scale. The smeared-smeared correlation functions were used for the form factor calculation because excited states contribute from both sides t and $t_s - t$ (see chapter 3.2.2) of the correlation functions.

Appendix D

Error analysis

The analysis of the statistical errors is one of the last steps of a Monte Carlo simulation. It provides the average value of an observable with its statistical error. This error depends on the number of configurations, the number of source positions and in the case of baryons, on the number of polarization matrices. We use several hundred gauge configurations and usually four source positions on each. The number of configurations is not large enough to investigate autocorrelations. Other techniques have to be used.
The so called pre-binning [73, 45] is used to get an estimate of the autocorrelation time (in Monte Carlo history) and to minimize it. N blocks of size K are build where $N \cdot K$ is the number of configurations times the number of source positions and the number of symmetries. On each block the mean value is build which is used as the new observable. This is done for increasing values of K until the correct statistical behavior $\sigma \sim 1/K$ is observed. In all our simulations it was enough to build the mean value over all source positions and symmetries on each configuration to observe the correct behavior.
The pre-binning procedure minimizes only the autocorrelation of the data but the number of configurations or hence K is maybe too small to achieve a reliable value of the statistical error. We use the so called bootstrap method [39] which has two advantages. The estimate of the statistical error is more reliable and one gets the same number of data points on each ensemble. Assuming a set of K pre-binned data samples have been generated. The bootstrap samples are produced by choosing randomly K times one entry of the pre-binned set. After that the mean value over the K values is computed. This is done for a fixed number C, the number of bootstrap samples which is in our simulations

1000. The mean value and the error can be computed from this set of bootstrap samples via the standard error procedure.
We use the Chi-square fitting procedure [89] to perform our fits. In this procedure the so-called Chi-square

$$\chi^2 = \Delta y^{\mathrm{T}} V^{-1} \Delta y \tag{D.1}$$

is minimized for each bootstrap sample. Assuming $i = 1...N$ data points (x_i, y_i) and a model function $f(x_i; a_1, ..., a_M)$ with M free fit parameters a, the vector Δy is defined as

$$\Delta y_i = y_i - f(x_i; a_1, ..., a_M). \tag{D.2}$$

The covariance matrix V is in uncorrelated fits simply defined as

$$V = \mathrm{diag}\left(\sigma^2\right), \quad \text{with } \sigma^2 = \frac{1}{C}\sum_{k=1}^{C}\left(y_k - \bar{y}\right)^2 \tag{D.3}$$

where $\bar{y}$ is the mean value of the bootstrap bins. In the correlated case all non-diagonal elements become

$$V_{ij} = \frac{1}{C}\sum_{k=1}^{C}\left(y_k^i - \bar{y}^i\right)\left(y_k^j - \bar{y}^j\right) \tag{D.4}$$

in addition. In our fits, the covariance matrix is fixed for all bootstrap samples which is often called 'frozen covariance matrix'. For the minimization of eq. D.1, we use the so-called Levenberg-Marquardt method [89] which is a standard method when the model function is not linear in its parameters a.
The goodness of the fit can be directly read off of the χ^2 value. The χ^2 statistic has a mean $\nu = N - M$ and the standard deviation of $\sqrt{2\nu}$ [89]. In practice, the reduced Chi-squared $\chi^2_{\mathrm{red}} = \chi^2/\nu$ is used. The fits can be treated as "good" as long as the reduced χ^2 is around 1 within one standard deviation of the χ^2 statistics. If the reduced χ^2 is much larger than 1 the fit function samples the data very badly. A very small value indicates that the errors are over-estimated or (in the case of an uncorrelated fit only) that one has to treat correlations explicitly with eq. D.4.
If we do fits or computed second order quantities we do it for each bootstrap sample individually. After that, the statistical error of the derived quantity or the fit parameters can be computed. This has the advantage that we can estimate the statistical error of quantities which are computed on different ensembles with different numbers of configurations because the number of bootstrap samples in each set is equal for all ensembles.

We used renormalization constants and improvement coefficient form other publications which are usually quoted with an error. To be able to include these factors with their errors in our analysis we generate a pseudo bootstrap set of this quantity. According to a Gaussian distribution random numbers are generated with the mean value and the variance of the quantity of interest. This pseudo bootstrap set can be integrated in the analysis bootstrap sample by bootstrap sample.

List of Figures

List of Tables

Bibliography

[1] M. Albanese et al. Glueball Masses and String Tension in Lattice QCD. *Phys.Lett.*, B192:163–169, 1987.

[2] C. Alexandrou. Hadron Structure and Form Factors. *PoS*, LATTICE2010:001, 2010, 1011.3660.

[3] C. Alexandrou, M. Brinet, J. Carbonell, M. Constantinou, P.A. Harraud, et al. Nucleon electromagnetic form factors in twisted mass lattice QCD. *Phys.Rev.*, D83:094502, 2011, 1102.2208.

[4] C. Alexandrou et al. Light baryon masses with dynamical twisted mass fermions. *Phys.Rev.*, D78:014509, 2008, 0803.3190.

[5] C. Alexandrou et al. Axial Nucleon form factors from lattice QCD. *Phys.Rev.*, D83:045010, 2011, 1012.0857.

[6] Constantia Alexandrou et al. Nucleon form factors with dynamical twisted mass fermions. *PoS*, LATTICE2008:139, 2008, 0811.0724.

[7] Claude Amsler et al. Review of Particle Physics. *Phys.Lett.*, B667:1–1340, 2008.

[8] Silas R. Beane und Martin J. Savage. Baryon axial charge in a finite volume. *Phys.Rev.*, D70:074029, 2004, hep-ph/0404131.

[9] Paulo F. Bedaque. Aharonov-Bohm effect and nucleon nucleon phase shifts on the lattice. *Phys.Lett.*, B593:82–88, 2004, nucl-th/0402051.

[10] M.A. Belushkin, H.-W. Hammer, und U.-G. Meissner. Dispersion analysis of the nucleon form-factors including meson continua. *Phys.Rev.*, C75:035202, 2007, hep-ph/0608337.

[11] Veronique Bernard, Latifa Elouadrhiri, und Ulf G. Meissner. Axial structure of the nucleon: Topical Review. *J.Phys.G*, G28:R1–R35, 2002, hep-ph/0107088.

[12] Veronique Bernard, Harold W. Fearing, Thomas R. Hemmert, und Ulf G. Meissner. The form-factors of the nucleon at small momentum transfer. *Nucl.Phys.*, A635:121–145, 1998, hep-ph/9801297.

[13] Veronique Bernard, Thomas R. Hemmert, und Ulf-G. Meissner. Cutoff schemes in chiral perturbation theory and the quark mass expansion of the nucleon mass. *Nucl.Phys.*, A732:149–170, 2004, hep-ph/0307115.

[14] J.C. Bernauer et al. High-precision determination of the electric and magnetic form factors of the proton. *Phys.Rev.Lett.*, 105:242001, 2010, 1007.5076.

[15] Tanmoy Bhattacharya, Rajan Gupta, Weon-Jong Lee, und Stephen R. Sharpe. Order a improved renormalization constants. *Phys.Rev.*, D63:074505, 2001, hep-lat/0009038.

[16] Benoit Blossier, Michele Della Morte, Georg von Hippel, Tereza Mendes, und Rainer Sommer. On the generalized eigenvalue method for energies and matrix elements in lattice field theory. *JHEP*, 0904:094, 2009, 0902.1265.

[17] Achim Bode et al. First results on the running coupling in QCD with two massless flavors. *Phys.Lett.*, B515:49–56, 2001, hep-lat/0105003.

[18] P.A. Boyle, A. Jüttner, C. Kelly, und R.D. Kenway. Use of stochastic sources for the lattice determination of light quark physics. *JHEP*, 0808:086, 2008, 0804.1501.

[19] Bastian B. Brandt, Andreas Jüttner, und Hartmut Wittig. Calculation of the pion electromagnetic form factor from lattice QCD. 2011, 1109.0196.

[20] B.B. Brandt, S. Capitani, M. Della Morte, D. Djukanovic, J. Gegelia, et al. Form factors in lattice QCD. 2011, 1106.1554.

[21] J.D. Bratt et al. Nucleon structure from mixed action calculations using 2+1 flavors of asqtad sea and domain wall valence fermions. *Phys.Rev.*, D82:094502, 2010, 1001.3620.

[22] John Bulava, Michael Donnellan, und Rainer Sommer. On the computation of hadron-to-hadron transition matrix elements in lattice QCD. 2011, 1108.3774.

[23] Gilberto Colangelo, Stephan Dürr, Andreas Jüttner, Laurent Lellouch, Heinrich Leutwyler, et al. Review of lattice results concerning low energy particle physics. *Eur.Phys.J.*, C71:1695, 2011, 1011.4408.

[24] S. Collins, M. Göckeler, Ph. Hägler, R. Horsley, Y. Nakamura, et al. Dirac and Pauli form factors from lattice QCD. 2011, 1106.3580.

[25] M. Creutz. Monte Carlo Study of Quantized SU(2) Gauge Theory. *Phys.Rev.*, D21:2308–2315, 1980.

[26] Michael Creutz. Chiral anomalies and rooted staggered fermions. *Phys.Lett.*, B649:230–234, 2007, hep-lat/0701018.

[27] Asit K. De, A. Harindranath, und Jyotirmoy Maiti. Investigation of Lattice QCD with Wilson fermions with Gaussian Smearing. 2007, 0712.4354.

[28] G.M. de Divitiis, R. Petronzio, und N. Tantalo. On the discretization of physical momenta in lattice QCD. *Phys.Lett.*, B595:408–413, 2004, hep-lat/0405002.

[29] L. Del Debbio, Leonardo Giusti, M. Luscher, R. Petronzio, und N. Tantalo. QCD with light Wilson quarks on fine lattices. II. DD-HMC simulations and data analysis. *JHEP*, 0702:082, 2007, hep-lat/0701009.

[30] Michele Della Morte et al. Non-perturbative quark mass renormalization in two-flavor QCD. *Nucl.Phys.*, B729:117–134, 2005, hep-lat/0507035.

[31] Michele Della Morte und Leonardo Giusti. A novel approach for computing glueball masses and matrix elements in Yang-Mills theories on the lattice. *JHEP*, 1105:056, 2011, 1012.2562.

[32] Michele Della Morte, Roland Hoffmann, Francesco Knechtli, Rainer Sommer, und Ulli Wolff. Non-perturbative renormalization of the axial current with dynamical Wilson fermions. *JHEP*, 0507:007, 2005, hep-lat/0505026.

[33] Michele Della Morte, Rainer Sommer, und Shinji Takeda. On cutoff effects in lattice QCD from short to long distances. *Phys.Lett.*, B672:407–412, 2009, 0807.1120.

[34] Simon Dinter, Constantia Alexandrou, Martha Constantinou, Vincent Drach, Karl Jansen, et al. Precision Study of Excited State Effects in Nucleon Matrix Elements. 2011, 1108.1076.

[35] Takumi Doi, Mridupawan Deka, Shao-Jing Dong, Terrence Draper, Keh-Fei Liu, et al. Nucleon strangeness form factors from N(f) = 2+1 clover fermion lattice QCD. *Phys.Rev.*, D80:094503, 2009, 0903.3232.

[36] D. Dolgov et al. Moments of nucleon light cone quark distributions calculated in full lattice QCD. *Phys.Rev.*, D66:034506, 2002, hep-lat/0201021.

[37] S. Duane, A.D. Kennedy, B.J. Pendleton, und D. Roweth. Hybrid Monte Carlo. *Phys.Lett.*, B195:216–222, 1987.

[38] S. Durr, Z. Fodor, J. Frison, C. Hoelbling, R. Hoffmann, et al. Ab-Initio Determination of Light Hadron Masses. *Science*, 322:1224–1227, 2008, 0906.3599.

[39] Bradley Efron. Bootstrap methods: Another look at the jackknife. *The Annals of Statistics.*, 7(1):1–26, 1979.

[40] Xu Feng, Karl Jansen, und Dru B. Renner. Resonance Parameters of the rho-Meson from Lattice QCD. *Phys.Rev.*, D83:094505, 2011, 1011.5288.

[41] Nadia Fettes, Ulf-G. Meissner, und Sven Steininger. Pion - nucleon scattering in chiral perturbation theory. 1. Isospin symmetric case. *Nucl.Phys.*, A640:199–234, 1998, hep-ph/9803266.

[42] R. Frezzotti und G.C. Rossi. Chirally improving Wilson fermions. 1. O(a) improvement. *JHEP*, 0408:007, 2004, hep-lat/0306014.

[43] J. Frison et al. Rho decay width from the lattice. *PoS*, LATTICE2010:139, 2010, 1011.3413.

[44] Patrick Fritzsch, Jochen Heitger, und Nazario Tantalo. Non-perturbative improvement of quark mass renormalization in two-flavour lattice QCD. *JHEP*, 1008:074, 2010, 1004.3978.

[45] Christof Gattringer und B. Lang. *Quantum Chromodynamics on the the Lattice*. Springer-Verlag Berlin Heidelberg, (2010).

[46] Paul H. Ginsparg und Kenneth G. Wilson. A Remnant of Chiral Symmetry on the Lattice. *Phys.Rev.*, D25:2649, 1982.

[47] M. Göckeler et al. Nucleon electromagnetic form-factors on the lattice and in chiral effective field theory. *Phys.Rev.*, D71:034508, 2005, hep-lat/0303019.

[48] M. Göckeler et al. Nucleon electromagnetic form-factors with Wilson fermions. *PoS*, LAT2007:161, 2007, 0710.2159.

[49] M. Göckeler et al. Nucleon structure with partially twisted boundary conditions. *PoS*, LATTICE2008:138, 2008.

[50] D.J. Gross und Frank Wilczek. Asymptotically Free Gauge Theories. 1. *Phys.Rev.*, D8:3633–3652, 1973.

[51] D.J. Gross und Frank Wilczek. Asymtotically free gauge theories. 2. *Phys.Rev.*, D9:980–993, 1974.

[52] Vera Gülpers. Improved stochastic estimators for disconnected contributions to mesonic form factors in lattice qcd. Diplomarbeit, Mainz, 2011.

[53] Rajan Gupta. Introduction to lattice QCD: Course. pages 83–219, 1997, hep-lat/9807028.

[54] S. Güsken. A Study of smearing techniques for hadron correlation functions. *Nucl.Phys.Proc.Suppl.*, 17:361–364, 1990.

[55] S. Güsken, K.H. Mutter, R. Sommer, A. Patel, und K. Schilling. Current algebra parameters on the lattice with a renormalization group improved Wilson action. *Nucl.Phys.*, B327:763, 1989.

[56] Ph. Hägler. Hadron structure from lattice quantum chromodynamics. *Phys.Rept.*, 490:49–175, 2010, 0912.5483.

[57] Anna Hasenfratz und Francesco Knechtli. Flavor symmetry and the static potential with hypercubic blocking. *Phys.Rev.*, D64:034504, 2001, hep-lat/0103029.

[58] Thomas R. Hemmert, Massimiliano Procura, und Wolfram Weise. Quark mass dependence of the nucleon axial vector coupling constant. *Phys.Rev.*, D68:075009, 2003, hep-lat/0303002.

[59] Claude Itzykson und Jean Bernard Zuber. *Quantum Field Theory*. Dover Pubn Inc, (24. Februar 2006).

[60] F.-J. Jiang und B.C. Tiburzi. Flavor twisted boundary conditions and the nucleon vector current. *Phys.Rev.*, D78:114505, 2008, 0810.1495.

[61] Fu-Jiun Jiang und Brian C. Tiburzi. Flavor twisted boundary conditions in the Breit frame. *Phys.Rev.*, D78:037501, 2008, 0806.4371.

[62] Joachim Kambor. The Delta (1232) as an effective degree of freedom in chiral perturbation theory. 1997, hep-ph/9711484.

[63] David B. Kaplan. A Method for simulating chiral fermions on the lattice. *Phys.Lett.*, B288:342–347, 1992, hep-lat/9206013.

[64] John B. Kogut und Leonard Süsskind. Hamiltonian formulation of Wilson's lattice gauge theories. *Phys.Rev.*, D11:395, 1975.

[65] B. Leder und F. Knechtli. The static force from lattice QCD with two dynamical quarks. *AIP Conf.Proc.*, 1343:242–244, 2011.

[66] Derek B. Leinweber, R.M. Woloshyn, und Terrence Draper. Electromagnetic structure of octet baryons. *Phys.Rev.*, D43:1659–1678, 1991.

[67] G. Peter Lepage. The analysis of algorithms for lattice field theory. Invited lectures given at TASI'89 Summer School, Boulder, CO, Jun 4-30, 1989.

[68] M. Lüscher. Selected topics in lattice field theory. "Lectures given at Summer School 'Fields, Strings and Critical Phenomena', Les Houches, France, Jun 28 - Aug 5, 1988".

[69] Martin Lüscher. Solution of the Dirac equation in lattice QCD using a domain decomposition method. *Comput. Phys. Commun.*, 156:209–220, 2004, hep-lat/0310048.

[70] Martin Lüscher. Schwarz-preconditioned HMC algorithm for two-flavour lattice QCD. *Comput. Phys. Commun.*, 165:199–220, 2005, hep-lat/0409106.

[71] Martin Lüscher. Deflation acceleration of lattice QCD simulations. *JHEP*, 12:011, 2007, 0710.5417.

[72] Martin Lüscher. Local coherence and deflation of the low quark modes in lattice QCD. *JHEP*, 07:081, 2007, 0706.2298.

[73] Martin Lüscher. Computational Strategies in Lattice QCD. 2010, 1002.4232.

[74] Martin Lüscher, Rajamani Narayanan, Peter Weisz, und Ulli Wolff. The Schrodinger functional: A renormalizable probe for non-Abelian gauge theories. *Nucl.Phys.*, B384:168–228, 1992, hep-lat/9207009.

[75] Martin Lüscher, Stefan Sint, Rainer Sommer, und Peter Weisz. Chiral symmetry and O(a) improvement in lattice QCD. *Nucl.Phys.*, B478:365–400, 1996, hep-lat/9605038.

[76] Martin Lüscher, Stefan Sint, Rainer Sommer, Peter Weisz, und Ulli Wolff. Non-perturbative O(a) improvement of lattice QCD. *Nucl.Phys.*, B491:323–343, 1997, hep-lat/9609035.

[77] M. Lüscher. Volume Dependence of the Energy Spectrum in Massive Quantum Field Theories. 2. Scattering States. *Commun.Math.Phys.*, 105:153–188, 1986.

[78] L. Maiani, G. Martinelli, M.L. Paciello, und B. Taglienti. Scalar densities and baryon mass differences in lattice QCD with Wilson fermions. *Nucl.Phys.*, B293:420, 1987.

[79] Marina Marinkovic. Strange quark mass and lambda parameter by the alpha collaboration. Talk at the Lattice conference 2011, International Symposium on Lattice Field Theory: http://tsailab.chem.pacific.edu/lat11/Parallel/Friday/PalB/Marinkovic.pdf, 2011.

[80] G. Martinelli und Christopher T. Sachrajda. A lattice study of nucleon structure. *Nucl.Phys.*, B316:355, 1989.

[81] Herbert Neuberger. Exactly massless quarks on the lattice. *Phys.Lett.*, B417:141–144, 1998, hep-lat/9707022.

[82] Holger Bech Nielsen und M. Ninomiya. No Go Theorem for Regularizing Chiral Fermions. *Phys. Lett.*, B105:219, 1981.

[83] Shigemi Ohta und Takeshi Yamazaki. Nucleon structure with dynamical (2+1)-flavor domain wall fermions lattice QCD. 2008, 0810.0045.

[84] I.P. Omelyan, I.M. Mryglod, und R. Folk. Symplectic analytically integrable decomposition algorithms: classification, derivation, and application to molecular dynamics, quantum and celestial mechanics simulations. *Computer Physics Communications*, 151(3):272 – 314, 2003.

[85] Konrad Osterwalder und Robert Schrader. Axioms for Euclidean Green's functions. *Commun.Math.Phys.*, 31:83–112, 1973.

[86] Michael E. Peskin und Daniel V. Schroeder. *An Introduction to Quantum Field Theory*. Perseus Books, (1995).

[87] Randolf Pohl et al. The size of the proton. *Nature*, 466(7303):213–216, 07 2010.

[88] H.David Politzer. Asymptotic Freedom: An Approach to Strong Interactions. *Phys.Rept.*, 14:129–180, 1974.

[89] William H. Press und other. *Numerical Recipes 3rd Edition: The Art of Scientific Computing*. Cambridge University Press, (2007).

[90] M. Procura, B.U. Musch, T. Wollenweber, T.R. Hemmert, und W. Weise. Nucleon mass: From lattice QCD to the chiral limit. *Phys.Rev.*, D73:114510, 2006, hep-lat/0603001.

[91] M.N. Rosenbluth. High Energy Elastic Scattering of Electrons on Protons. *Phys.Rev.*, 79:615–619, 1950.

[92] Yousef Saad. *Iterative methods for sparse linear systems*. Society for Industrial Mathematics, (2003).

[93] C.T. Sachrajda und G. Villadoro. Twisted boundary conditions in lattice simulations. *Phys.Lett.*, B609:73–85, 2005, hep-lat/0411033.

[94] Stefan Scherer. Introduction to chiral perturbation theory. *Adv.Nucl.Phys.*, 27:277, 2003, hep-ph/0210398. To be edited by J.W. Negele and E. Vogt.

[95] Stefan Scherer. Effektive Feldtheorie I und II. http://www.kph.uni-mainz.de/T/members/scherer/lecture/EFTI&II.pdf, 2006.

[96] B. Sheikholeslami und R. Wohlert. Improved continuum limit lattice action for QCD with Wilson fermions. *Nucl.Phys.*, B259:572, 1985.

[97] Andrea Shindler. Twisted mass lattice QCD. *Phys.Rept.*, 461:37–110, 2008, 0707.4093.

[98] Stefan Sint. On the Schrodinger functional in QCD. *Nucl.Phys.*, B421:135–158, 1994, hep-lat/9312079.

[99] Stefan Sint und Peter Weisz. Further results on O(a) improved lattice QCD to one loop order of perturbation theory. *Nucl.Phys.*, B502:251–268, 1997, hep-lat/9704001.

[100] R. Sommer. A New way to set the energy scale in lattice gauge theories and its applications to the static force and alpha-s in SU(2) Yang-Mills theory. *Nucl.Phys.*, B411:839–854, 1994, hep-lat/9310022.

[101] Georg von Hippel. Scale setting via the omega baryon mass. Talk at the Lattice conference 2011, International Symposium on Lattice Field Theory: http://tsailab.chem.pacific.edu/lat11/Parallel/Friday/MntC/5-von_hippel.pdf, 2011.

[102] Andre Walker-Loud. Topics in effective field theory for lattice QCD. 2006, hep-lat/0608010. Ph.D.Thesis (Advisor: Professor Martin J. Savage).

[103] Kenneth G. Wilson. Confinement of quarks. *Phys.Rev.*, D10:2445–2459, 1974.

[104] K.G. Wilson. Quarks: From paradox to myth. *Subnucl.Ser.*, 13:13–32, 1977.

[105] H. Wittig. *QCD on the lattice, in: Handbook of Particle Physics* (HRSG. H. SCHOPPER). Springer Verlag, im Druck.

[106] Ulli Wolff. Monte Carlo errors with less errors. *Comput.Phys.Commun.*, 156:143–153, 2004, hep-lat/0306017.

[107] Takeshi Yamazaki, Yasumichi Aoki, Tom Blum, Huey-Wen Lin, Shigemi Ohta, et al. Nucleon form factors with 2+1 flavor dynamical domain-wall fermions. *Phys.Rev.*, D79:114505, 2009, 0904.2039.

[108] Takeshi Yamazaki und Shigemi Ohta. Nucleon form-factors and structure functions with N(f) = 2+1 dynamical domain wall fermions. *PoS*, LAT2007:165, 2007, 0710.0422.

[109] Chen-Ning Yang und Robert L. Mills. Conservation of isotopic spin and isotopic gauge invariance. *Phys.Rev.*, 96:191–195, 1954.

List of publications

Published:

- B.B Brandt, S.Capitani, M. Della Morte, D. Djukanovic J. Gegelia and others. Form factors in lattice QCD. *Eur.Phys.J.ST*, 198, 79-94, 2011, arXiv:1106.1554 [hep-lat].

Proceedings:

- S. Capitani, M. Della Morte, E. Endress, A. Jüttner, B. Knippschild, H. Wittig and M. Zambrana, "Mesonic and baryonic correlation functions at fine lattice spacings", *PoS LAT2009*, **095** (2009) arXiv:0910.5578 [hep-lat].
- B.B. Brandt, S. Capitani, D. Djukanovic, G. von Hippel, B. Jäger, A. Jüttner, B. Knippschild, M. Della Morte, and H. Wittig, "Wilson fermions at fine lattice spacings: scale setting, pion form factors and $(g-2)_\mu$", *PoS LAT2010*, **164** (2010), arXiv:1010.2390 [hep-lat].
- S. Capitani, M. Della Morte, B. Knippschild, H. Wittig, "Systematic errors in extracting nucleon properties from lattice QCD", *PoS LAT2009*, **147** (2010), arXiv:1011.1358 [hep-lat].
- S. Capitani, M. Della Morte, G. von Hippel, B. Knippschild, H. Wittig, "Scale setting via the Ω baryon mass", *PoS LAT2011*, arXiv:1110.6365 [hep-lat].
- J. Bulava, P. Gerhold, G. W.-S. Hou, K. Jansen, B. Knippschild and others, "Study of the Higgs-Yukawa theory in the strong-Yukawa coupling regime", *PoS LAT2011*, arXiv:1111.4544 [hep-lat].

In preparation:

- S. Capitani, M. Della Morte, A. Jüttner, B. Knippschild, H.B. Meyer, H. Wittig, Extracting the axial charge from lattice QCD

Mainz, den 05.03.2012